
THE UNIVERSITY *of* EDINBURGH

# Rheology and flow properties of a deformable droplet suspension

Martina Foglino


Doctor of Philosophy
The University of Edinburgh
January 2019

# Lay Summary

Science, and common sense, has taught us that solid and liquid materials display very different characteristics and properties which enable us to easily distinguish and classify them. Solids, for example, are characterised by a crystalline structure where the material molecules are closely packed, therefore causing a structural rigidity and resistance to changes of shape or volume. Unlike liquids, solid objects retain their own shape and they do not flow under shear. Nevertheless, it has been knows for more than a century that some dense materials are neither simple liquids nor simple crystalline solids, and therefore they do not readily fall within the classical scheme of materials classification. These "complex fluids" are characterised by mechanical properties that are intermediate between ordinary liquids and solids. For instance, in many cases those materials maintain their shape for a certain time before starting to flow eventually. In other words, they behave as solids at short times, and liquids at long times, displaying what we call a "viscoelastic" behaviour.

In this thesis we aim to uncover some of the mechanisms which regulate the properties and flow behaviour of complex fluids. To this end, we study a *suspension* made up of soft and deformable droplets and we analysed its flow, induced by applying an external pressure gradient on our fluid. Via computer simulations, we were able to observe how our fluid *viscosity*, i.e. its ability to easily flow, can change as the amount of pressure exerted on the suspension is varied. Our most relevant finding is the observation of a *discontinuous shear thinning* behaviour: the viscosity of our droplets suspension sharply decreases after a certain threshold value of the applied pressure. In other words, there is a certain amount of force we can apply to push our droplets through the channel which will cause them to flow much more readily than they otherwise would. Further analysis enabled us to conclude that such threshold value of the applied pressure is dependent on the droplets *deformability*, i.e. how firmly they resist to

shape deformation, in that softer droplets suspensions will be characterised by a lower value of such threshold pressure gradient than harder ones.

Finally, in our last chapter we study the intriguing properties of *reversibility* of our droplets suspension. To this end, we recreate and observe the behaviour of our suspension when a certain droplet is periodically inflated and deflated, therefore causing all the neighbouring ones to move across the suspension. This enables us to distinguish the *reversible* cases, where all the neighbouring droplets eventually come back to their original positions, from the *irreversible* ones, where the final positions of most of the droplets is different from their original ones. Moreover, we test how the reversible and irreversible behaviours of our suspension interchange as we vary the final size of the growing droplet, concluding that a faster or larger increase of the growing droplet volume leads to an irreversible behaviour of the overall suspension.

# Abstract

Concentrated suspensions of colloidal particles in a liquid solvent are often found in nature and industry. Familiar examples include ice cream, mayonnaise, paints and biological fluids such as blood. It is well known that the flow properties of colloidal suspensions can be distinctly non-trivial, for instance presenting shear thinning or shear thickening behaviour under different circumstances. Often, in such colloidal fluids, the dispersed particles are not hard but soft and deformable. For instance, we can think about fat droplets floating in milk or eukaryotic cells: all these can deform under flow or when subjected to a mechanical stress. While hard-spheres fluids have been extensively studied and provide the basis for our understanding of the glass transition and soft glassy rheology, comparatively less is known about the flow response of a suspension of deformable particles. Nonetheless, there is evidence suggesting that the physics of soft suspensions is both highly interesting and important in applications. Indeed, particle deformability is important to determine the rheology of a material; for example, emulsions and foam do not normally display shear thickening, unlike hard-spheres colloidal fluids.

In this thesis, we use two-dimensional lattice Boltzmann simulations to investigate the dynamics and the rheological properties of a suspension of soft, non-coalescing deformable droplets. In particular, in the first results chapter, we analysed the rheology of a deformable suspension when subjected to a pressure driven flow, regulated by the external application of an homogeneous body-force on the underlying fluid. Here, we provide evidence of a discontinuous shear thinning behaviour, occurring at a concentration dependent value of the forcing. We further show that this response is associated with a non-equilibrium transition between a "hard" (or less deformable) phase, which is nearly jammed and flows very slowly, and a "soft" (or mode deformable) one, which flows much more easily.

The observed hard-soft transition is further analysed in the second results chapter,

where we provide a detailed study of the role of the droplet surface tension in the overall suspension rheology. After confirming the discontinuous shear thinning behaviour for a range of imposed droplet surface tension, we determine and discuss how the property of deformability affects the forcing threshold leading to the discontinuity. Moreover, we find that the effective viscosity of the suspension is mainly determined by its Capillary number.

In the last results chapter we aim to understand the reversibility properties of our deformable droplet suspension, shedding light on the onset of irreversibility and loss of predictability. To this end we use two different sets of simulations which represent two distinct ways of imposing a deformation on our system and therefore testing its reversibility properties. In the first part, a droplet in our suspension is periodically inflated and deflated, therefore causing an overall rearrangement of the neighbouring droplets. On the other hand, in the second part an oscillatory shear is imposed on the walls which constrain our suspension. In both cases, the droplets position is carefully tracked, enabling us to verify if, after each period of the imposed deformation, all the droplets come back to their original positions, and therefore our suspension shows reversible behaviour. As we will see, a transition between a reversible and an irreversible phase is detected and found to depend on the amount of imposed deformation.

# Declaration

I declare that this thesis was composed by myself, that the work contained herein is my own except where explicitly stated otherwise in the text, and that this work has not been submitted for any other degree or professional qualification except as specified.

Parts of this work have been published in [1],[2].

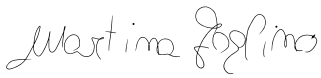

(*Martina Foglino, January 2019*)

# Acknowledgements

First I would like to deeply thank my supervisor Davide Marenduzzo, for his continuous and generous support, caring advices and enviable knowledge (and for the numerous coffees as well). I know I will remember these three years with a touch of nostalgia.

Among the many people that have been part of my life these years, a special mention and thanks go to Ana, precious friend and spectacular flatmate whose mind reading abilities never cease to impress me.

I would especially like to thank Alex, whom I am immensely glad I met at the other end of the corridor, and whose presence was and is all I need.

Another very special thanks goes to my mum, without whom I would not be here (for obvious, and less obvious, reasons), and the rest of my supportive family.

Finally, I would like to thank all members of the COLLDENSE network and all the collaborators in the Soft Matter group in Edinburgh and elsewhere, for all the useful discussions and invaluable inputs. Among those, thanks to Davide Michieletto for never forgetting to check on me.

# Contents

# List of Figures

# List of Tables

# Chapter 1

# The physics of colloids

The ultimate goal of condensed matter physics relies on describing the link connecting the microscopic structural properties of a material to its macroscopic behaviour. In the case of systems in thermal equilibrium, the microscopic and macroscopic variables are related by the free energy and the partition function, which encodes the statistical weight of the possible microstates [7].

On the other hand, in soft matter physics, systems are rarely in thermal equilibrium and there is therefore no generic scheme for predicting macroscopic behaviour from analysing the system microscopic properties. We can distinguish a class of systems which are out of equilibrium in a quiescent state, e.g. polymer and colloidal glasses, which are trapped in a dynamically arrested state and therefore are not allowed to explore all their phase space on an experimental time scale [8, 9]. Instead, other systems are driven out of equilibrium by mechanical deformation where the characteristic stress in soft matter scales around $\sim 1 - 10$ Pa, a range of values easily accessible in every day life (e.g. by stirring a suspension with a spoon). It is therefore important to be able to understand and predict the response of a system to flow and deformation, an area of studies know as *rheology*.

Perhaps the most studied system within soft matter physics is an assembly of hard, spherical particles suspended in a fluid. At rest, the phase behaviour of such system is well understood, as it exhibits a transition from a fluid, to a crystal to a glassy phase as the concentration $\phi$ is increased. In real suspensions of nearly hard spheres, this picture is reasonably insensitive to the details of the particles under examination. On the other hand, under shear such systems display a rich

phenomenology which strongly depends not only on the concentration $\phi$ but also on details such as particle size, interaction potential and surface properties.

This hard sphere suspension model can be used to successfully describe a variety of colloidal suspensions. Nevertheless, many complex fluids are made out of soft and deformable droplets, whose macroscopic flow behaviour displays interesting properties that are different from their hard counterpart. While hard sphere suspensions have been extensively studied, comparatively less is known about soft and deformable ones. The purpose of this thesis is to shed light on the macroscopic flow behaviour of a suspension made out of non coalescing deformable droplets (e.g. droplets stabilised by surfactants or red blood cells), in order to provide an understanding of the physical properties that regulate this kind of systems. In particular, the role of the droplets ability to deform in affecting the flow behaviour is thoroughly investigated.

## 1.1 Complex Fluids

Despite our tendency to classify the world into organized, distinct classes which can give us a sense of the various types of properties and behaviours which can be observed, we are sometimes forced to face the limitations of this methodical approach.

One of the fundamental distinctions we can apply to classical materials is the one between solids and liquids. These are commonly defined as, respectively, different states of matter characterised by regularly ordered particles presenting a repeating pattern, and a nearly incompressible isotropic and homogeneous fluid that retains the shape of its container. However, it has been known for more than a century that some condensed-phase materials are neither simple liquids nor simple crystalline solids, and thus they do not readily fall within the standard materials classification. Instead, these "complex fluids" posses properties which are intermediate between the two classes of materials, therefore presenting a behaviour which can switch from solid-like to liquid-like depending on external conditions. For such materials, the relation between stress and deformation can be non-linear, sometimes unknown or under dispute.

A common feature of complex fluids is their "viscoelastic" behaviour. The latter implies that such materials behave as solids at short times, thus maintaining their

shape, while they act as fluids at long times, thus starting to flow. Depending on the fluid under examination, the characteristic time for observing such change in the material properties varies from seconds to days.

Other than the ability to flow, another typical feature which distinguishes solids from liquids is their microscopic structures. In particular, while crystalline solids are anisotropic, i.e. their properties can depend on the orientation of the deformation with respect to the crystallographic axes, classical liquids are isotropic, i.e. their properties are equal in all directions. Relating to these structural properties, an example of a complex fluid showing a peculiar behaviour is given by liquid crystals, which flow like fluids but show mechanical anisotropic properties like those of crystals.

Complex fluids are extremely common in everyday life. Some examples can be found in simple food products, for instance emulsions like mayonnaise, which is made out of droplets of vegetable oil suspended in vinegar and stabilized by lecithin. As such, mayonnaise, as well as ice cream, is characterised by a low yield stress above which it will start flowing. Other common examples of complex "foods" can be found in ice cream, milk, cream, cheese and chocolate.

Complex fluids can also be found in living organisms. For instance, blood is a suspension composed by blood cells, flexible and deformable disks suspended in clear plasma, which itself is a viscoelastic fluid containing interacting protein macromolecules. It has been observed that at modest shear rates, the flow and orientation properties of red blood cells are similar to those of rigid disks, while at higher shear rates their flow resembles that of a fluid droplet. The viscoelastic properties of blood therefore determine the pumping load on the heart, and as a consequence affect the performances of artificial heart valves.

Personal care products like shampoo, nail polish, lipstick and toothpaste, also possess very peculiar rheological properties which are carefully tuned for customer satisfaction. Indeed, they are specifically designed to flow readily from their container into one's hand and then to be viscous enough to not immediately drip.

Just considering the range of examples cited above, it is clear that complex fluids are ubiquitous in nature as well as industry. As such, they have been, and still are, an interesting and lively topic of research pursuing the multiple task of understanding their fundamental physical properties as well as finding ways to exploit those properties in order to design smart soft materials.

In what follows, we will focus on the properties of a generic colloidal suspension, one of the simplest kind of complex fluid, which we will use as a general framework for our analysis of deformable droplets suspension discussed in this thesis.

## 1.2 Colloidal Suspensions

The term "colloidal suspension", deriving from the Greek $\kappa o\lambda\lambda\alpha$ ("glue"), is used to indicate an heterogeneous system where small particles of solid or liquid with dimension of order $\sim 100nm - 10\mu m$ or less are dispersed in a liquid medium. The stability of this kind of system is heavily affected by the interactions between the colloidal particles, which can cause different degrees of aggregation disrupting the suspension homogeneity. The colloidal particles are much larger in size with respect to the molecules of the suspending fluid, and can therefore be thought of as being immersed in a continuum. The molecular properties of the fluid in which particles are embedded is determined by variables like the temperature $T$, density $\rho$ and viscosity $\eta$.

### 1.2.1 Colloidal interactions: van der Waals, electrostatic and steric stabilisation

By definition, a colloidal suspension is characterised by a large amount of interfacial area between the particles and fluid, which causes a high value of the interfacial energy. Intuitively, in order to prevent the colloid from quickly aggregating to form a single colloidal mass, there must be other forces between the particles that prevent them from coalescing.

Colloidal aggregation typically results form van der Waals attraction, which is a quantum-mechanical force arising from the interaction between fluctuating dipoles proportional to $\sim -C/r^6$ [10],[11]. A sketch of the van der Waals potential is shown in Fig. 1.1.

As previously anticipated, colloids must also present some repulsive force in order to avoid flocculation and obtain a stable colloidal suspension. To this end, there are two possible approaches: introducing an electric charge repulsion between colloids, or a steric stabilization obtained through a polymer layer bound to the particle surface.

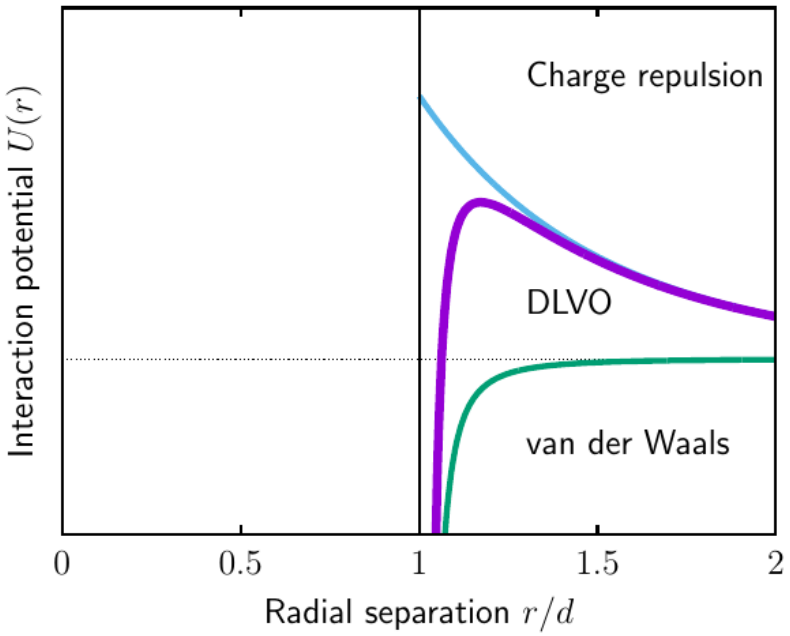


**Figure 1.1** *Sketch of the total pair interaction $U(r)$ for a charge-stabilised colloid. We can see that the purple curve is decomposed into contributions from van der Waals attractions (green curve) and electric repulsion (blue curve). This figure is taken from [1].*

As we know, when immersed in water many colloidal particles acquire an electric charge. The mechanism of such charging depends on the specific chemistry of the particle surface, but it commonly occurs via dissociation of surface groups or the absorption of ions in the fluid to a previously uncharged surface. Furthermore, the presence of dissolved ions in water profoundly affects the nature of electrostatic interaction. In particular, the normal Coulomb electrostatic interactions are replaced by a screened Coulomb one which exponentially decays in strength with increasing distance.

Considering an ionised surface, we can imagine that the overall charge neutrality will be maintained by a layer of counterions attracted to the surface by the electrostatic field. While some of those counterions will be tightly bound to the surface, forming the so-called "Stern layer", others will form a diffuse concentration profile. The latter, together with the density of ions, determines the form of the interaction potential between two charged objects that are brought together. Such interaction is firstly characterised by a repulsive force, originating from the osmotic pressure exerted by the ions in the gap, and is proportional to $\sim e^{-Krm}/r$ where $m$ is the mass of the particle, $K$ is a scaling constant and $r$ is the radial distance to the particle.

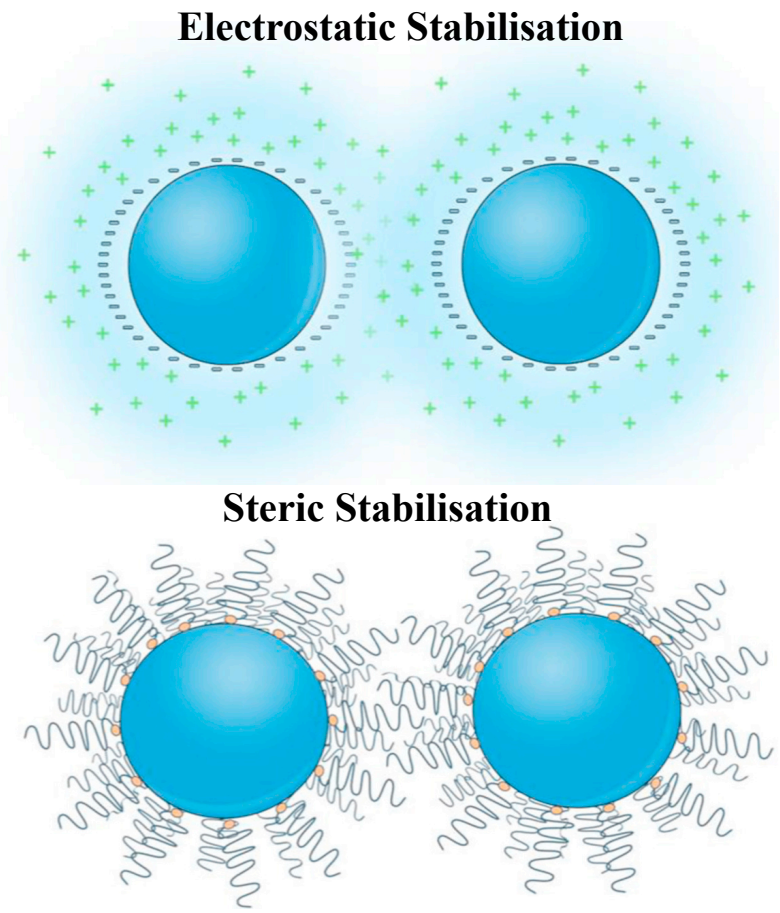


**Figure 1.2** *Schematic representation of a colloidal sphere characterised by a charge stabilisation (a), and a steric stabilisation (b), respectively. The figure is taken from [2].*

The length scale over which the electrostatic interactions are screened in the fluid is given by the so called Debye length which corresponds to the quantity $k^{-1}$ where $k$ is given by

$$k = \left(\frac{2n_0e^2}{\epsilon_0\epsilon k_B T}\right)^{\frac{1}{2}} \tag{1.1}$$

where $n_0$ is the concentration of ions in the fluid far away from the surface and $\epsilon_0$ is the permittivity of free space. A sketch of the potential energy due to charge stabilisation is given in Fig. 1.1 (blue curve). As we can notice, such potential displays a finite value at $U_r(2R) = ZR$ which depends on the surface potential and decays with $r$. In the same figure we can also observe a sketch of the total potential energy due to the sum of the electric charge and van der Waals interactions, $U = U_{vdW} + U_r$ (purple curve) [12]. As we can notice, for this

particular choice of the constants $A$, $Z$ and $k$, the total potential $U(r)$ is strongly attractive for small values of $r$, exhibits a maximum at $r_{max}$ and becomes repulsive for $r > r_{max}$. Different combinations of the above mentioned parameters can lead to pure attraction or the formation of a secondary minimum.

As previously mentioned, another way of stabilising a colloid is via steric stabilization. The latter is due to a polymer brush which is either physically bound or absorbed to the surface of the particles [13]. A schematic representation of the difference between a charge or steric stabilised particle is given in Figure 1.2.

As shown in this figure, in a "good solvent" the grafted polymer molecules extend out into the solution. If two particles approach one another, their respective brushes are compressed, leading to a higher concentration of the polymer solution inside the gap. The resulting reduction of the configurational degrees of freedom of the polymers leads to an entropic penalty and a consequent repulsive force $F_{poly}(r)$. The specific form of $F_{poly}(r)$ can be predicted with various models based on the radial density profile of the brush and the grafting density on the surface [11][14]. On the other hand, if the suspending fluid is not a good solvent for the brush, the energetic interactions between monomers can lead instead to an attractive potential [14].

### 1.2.2 Colloidal suspension under flow

Having introduced the interactions that characterise the physics of colloids, we now discuss the behaviour of such a system when subjected to a constant shear. We consider here the simplest colloidal system, i.e. a suspension of hard spheres interacting with rigid repulsion, where we neglect the effect of finite-range potential interactions such as van der Waals. Indeed, even suspensions as simple as these, can show rather complex rheological phenomena. For a neutrally-buoyant system of $N$ spheres in a domain of volume $V$, the phase behaviour is determined by the volume fraction

$$\Phi = \frac{4}{3}\pi R^3 \frac{N}{V}, \tag{1.2}$$

representing the fraction of volume occupied by the particles. Considering a colloidal suspension at rest, we can distinguish different phases as we change the value of $\Phi$. For instance, for $\Phi < 0.494$, we can observed a fluid phase, for

$0.494 \leq \Phi < 0.545$ there is a coexistence between the fluid and an entropically-stabilised crystal phase, while for $\Phi \geq 0.545$ the equilibrium phase is entirely crystalline. However, it has been found that above the glass transition volume fraction $\phi_g \approx 0.58$, homogeneous crystal nucleation is suppressed and the system dynamically arrests into a disordered phase. In contrast with the fluid phase, in the glassy regime colloids are constrained to move within the cage built by their nearest neighbours and out-of-cage diffusion is arrested on experimental time scales [15].

### Zero-shear Viscosity

An important quantity which characterises the rheological behaviour of a colloidal suspension is the shear viscosity $\eta$. At very low volume fractions ($\Phi < 0.03$), this quantity is predicted by the Einstein's formula [16]

$$\eta = \eta_0(1 + 2.5\Phi). \tag{1.3}$$

This equation, where $\eta_0$ is the viscosity of the underlying solvent, can be derived form the viscous dissipation produced by the flow around a single sphere. It is therefore only valid for the case where the suspension is dilute enough that the flow field around one sphere is not appreciably influenced by the presence of the neighbouring ones. On the other hand, when two sphere are close enough, they experience hydrodynamic interactions which, for this case, leads to contributions to $\eta$ proportional to $\Phi^2$. In a similar way, three body hydrodynamic interactions lead to a term of order $\Phi^3$ and so on. Restricting the calculation to order $\Phi^2$, the effect on the suspension viscosity $\eta$, calculated by Batchelor and combined with (1.3), gives [17]

$$\eta_r = \frac{\eta}{\eta_0} = 1 + 2.5\Phi + 6.2\Phi^2. \tag{1.4}$$

Let's suppose that we increase by $d\Phi$ the particle concentration in a suspension of viscosity $\eta(\Phi)$ by adding a few new particles. If the suspension under study behaves as an homogeneous viscous medium of viscosity $\eta(\Phi)$, the corresponding increment in viscosity $d\eta$ resulting from the addition of the new particles is given

by Einstein's formula (1.3), as

$$d\eta = 2.5\eta(\Phi)d\Phi. \tag{1.5}$$

Integrating this equation gives

$$\eta = \eta_0 e^{\frac{5\Phi}{2}}. \tag{1.6}$$

The latter equation, valid for the case where the particles are hard spheres, can be generalised for an arbitrarily shaped particles, yielding to

$$\eta = \eta_0 e^{[\eta]\Phi} \tag{1.7}$$

where $[\eta]$ is the intrinsic viscosity, a dimensionless quantity representing the dilute limit of the viscosity increment per unit particle volume fraction, divided by the solvent viscosity:

$$[\eta] = \lim_{\Phi \to 0} \frac{\eta - \eta_0}{\Phi \eta_0}. \tag{1.8}$$

Nevertheless, equation (1.7) fails at high $\Phi$, due to the correlation of particles positions as a consequence of crowding. In order to account for this divergence, we can replace equation (1.7) with

$$d\eta = \frac{[\eta]\eta_0 d\Phi}{(1 - \Phi/\Phi_m)} \tag{1.9}$$

so that $d\eta$ diverges as $\Phi$ approaches the maximum packing volume fraction $\Phi_m$ ($\Phi_m \approx 0.63 - 0.64$ for hard spheres). Integrating (1.9) we obtain the Krieger-Dougherty equation [17]

$$\eta = \eta_0 \Big(1 - \frac{\Phi}{\Phi_m}\Big)^{-[\eta]\Phi_m}. \tag{1.10}$$

The latter is an empirical equation valid for suspension of particles of spherical or other shape, where, generally, as the particle aspect ration increases, $[\eta]$ increases and $\Phi_m$ decreases.

To conclude, it is worth mentioning that for high loading of particles, the particle-size distribution has a strong effect on the viscosity of the overall suspension. In particular, when particles of two different sizes are mixed together, the viscosity can be significantly lower than its corresponding value for a suspension containing the same volume fraction of monodisperse particles. Such behaviour is of significant practical importance in the formulation of heavily loaded suspension, such as plastic molding compounds.

### Non-Newtonian effects: shear thinning and shear thickening

Experiments and simulations show that above a certain threshold of volume fraction, the suspension viscosity becomes sensitive to shear rate, or equivalently to shear stress. Indeed, when a colloidal suspension is sheared at rate $\dot{\gamma}$, the particles interactions are dominated by hydrodynamics forces mediated by the fluid, therefore generating a stress proportional to $\eta_0\dot{\gamma}$. Moreover, the shear imposed on the system leads to a distortion of the microscopic structure from its isotropic equilibrium state, which in turn causes a reduction of the available free volume thereby generating an entropic stress proportional to $K_BT/R^3$ (where $R$ is the particle size), which opposes the imposed stress.

The dependence of the viscosity on the imposed shear rate therefore occurs for values of shear that are high enough to disturb the suspension particle distribution from its equilibrium configuration. The particle diffusivity therefore controls the time necessary in order for the suspension to regain its equilibrium state. In a dilute solution, such diffusivity for a particle of radius $R$ is given by Stokes-Einstein law,

$$D_0 = \frac{k_BT}{6\pi\eta_0 R}. \tag{1.11}$$

We can also define the time $\tau_D$, usually referred to as Brownian time, necessary for a particle to diffuse over a distance equal to its radius $R$ as

$$\tau_D = \frac{R^2}{D_0} = \frac{6\pi\eta_0 R^3}{k_BT}. \tag{1.12}$$

Typical value for this quantity is approximately $\sim$ 1s for a particle of diameter $\sim 1\mu m$ in water. The suspension relative viscosity is therefore determined by

the volume fraction $\Phi$ as well as the ratio of the time taken for a free particle to diffuse over a distance equal to its own radius to the time taken to be advected over the same distance by the imposed flow field. This ratio is an adimensional quantity known as Peclet number $Pe$ and is defined as

$$Pe = \frac{\eta_0 \dot{\gamma} R^3}{k_B T} \propto \dot{\gamma} \tau_D. \tag{1.13}$$

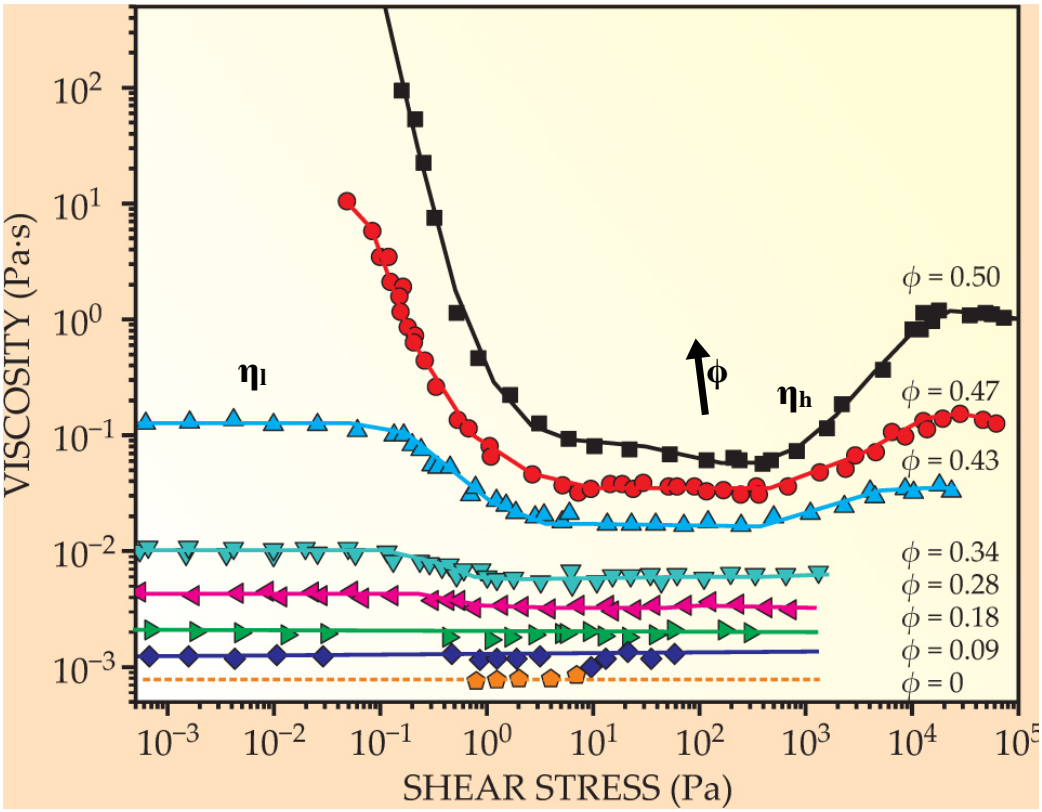


**Figure 1.3** *Viscosity of a colloidal dispersion as a function of the applied shear stress. Each curve refers to a different value of the suspension volume fraction $\Phi$, which increases as indicated by the arrow. As we can notice, beyond the critical stress, the viscosity decreases (shear thinning), while at higher values of shear stress the viscosity curve increases (shear thickening). $\eta_l$ and $\eta_h$ denote the limiting low- and high-shear viscosities, respectively. This image has been adapted from figure 1 in [3].*

As shown in Figure 1.3, the form of $\eta(Pe, \Phi)$ is well known [3]. For low value of $Pe$, $Pe \ll 1$, we observe a standard Newtonian flow, as Brownian motion is able to randomise the suspension microscopic structure on the same timescale of

the imposed shear. In this regime, the viscosity increases with $\Phi$ and diverges at the threshold value of $\Phi_g \approx 0.58$ [4]. Above $\Phi_g$, the system acquires a yield stress $\sigma_Y = \sigma(Pe \longrightarrow 0) \sim k_B T/R^3$, which increases with $\Phi$. On the other hand, below $\Phi_g$ the system exhibits shear thinning for $Pe \sim 1$, and reaches a second Newtonian regime at $Pe \gg 1$ with a viscosity that diverges at the threshold value of $\Phi_{RCP} \approx 0.64$, corresponding to the highest amorphous packing fraction for lubricated hard spheres. In this regime, Brownian motion is no longer able to randomise the microstructure , which therefore becomes highly anisotropic, and the viscosity is now dominated by hydrodynamic interactions between the colloids.

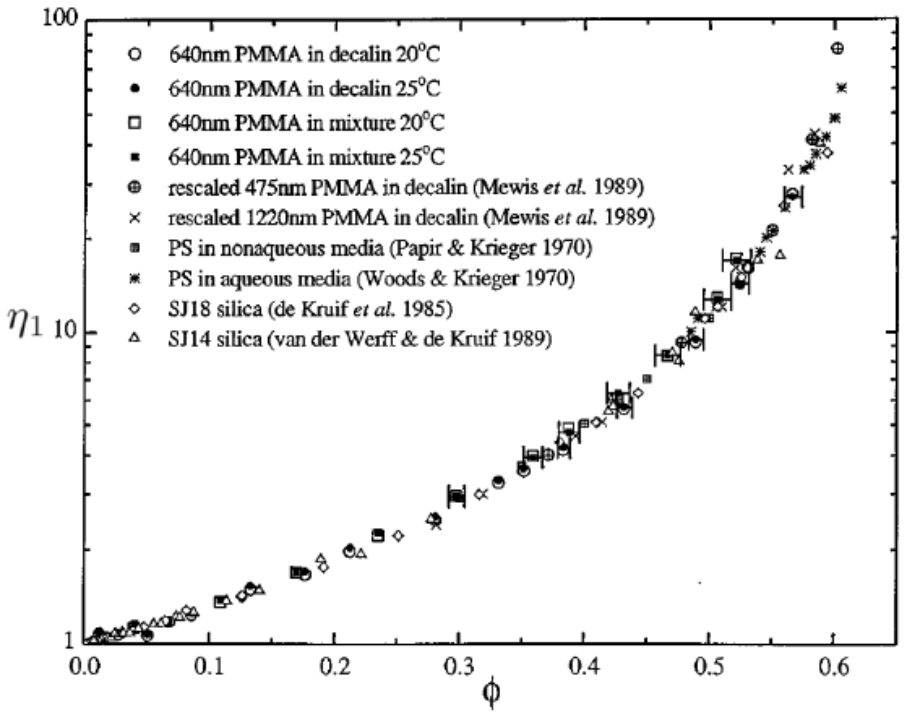


**Figure 1.4** *Limiting high shear viscosity as a function of* $\Phi$ *for diverse model colloidal hard spheres dispersions. This image is taken from [4].*

The scenario described above has been observed in wide range of hard sphere model systems [18], [19] [20]. The dependence of the system high-shear viscosity as a function of the volume fraction $\Phi$ is depicted in Figure 1.4, where we show the trend of $\eta_h(\Phi)$ for a mixture of charge and sterically stabilised colloids [4]. The data can be collapsed onto a single master curve by a $\sim 5\%$ shift in $\Phi$, which accounts for differences in polydispersity and discrepancies in $\Phi$ due to different

preparation method [21].

A simple qualitative interpretation of the viscosity behaviour described above can be obtained on considering the roles played by the different types of interactions among particles (Figure 1.5). In particular, the equilibrium configuration of the particle distribution across the suspension is set by the balance of stochastic and interparticle forces at play, including electrostatic and van der Waal forces, but is not affected by the hydrodynamic interactions. We can therefore imagine the low shear viscosity ($Pe \ll 1$) as composed of two different components referring to the interparticle forces and to hydrodynamic interactions, respectively. In this scenario, the former is predominant over the latter and the fluid exhibits an isotropic structure. Under weak but increasing shear flow ($Pe \sim 1$), as particles rearrange in order to reduce their interactions, the fluid structure becomes anisotropic and flows much more readily.

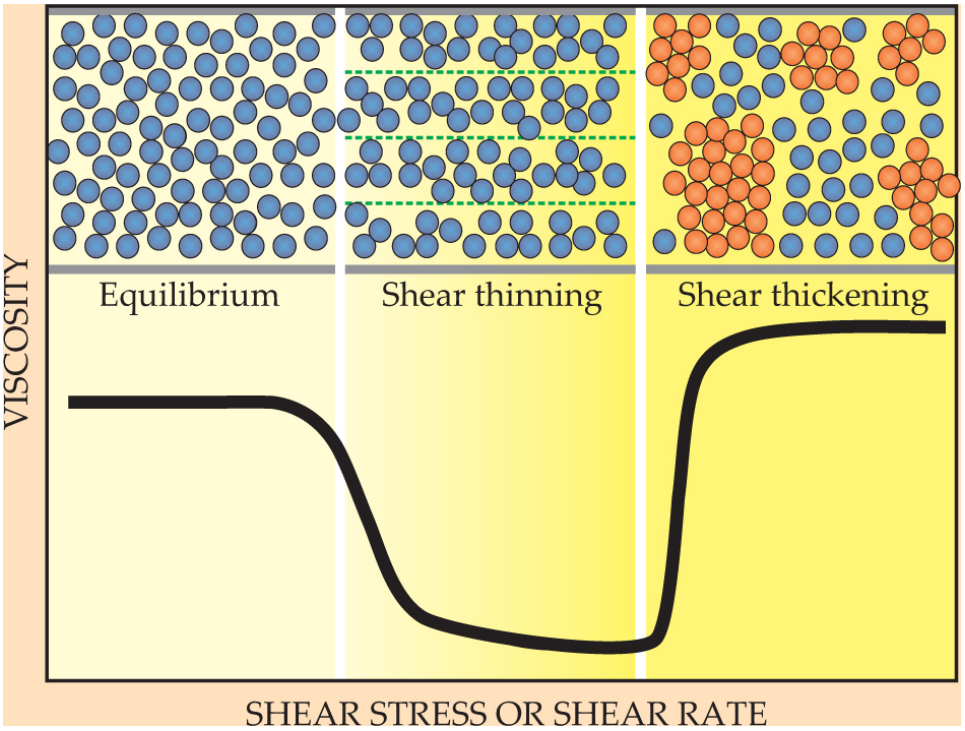


**Figure 1.5** *Schematic representation of the change in microstructure of a colloidal dispersion which explains the transition to shear thinning and shear thickening. This image has been adapted from figure 2 in [3].*

A longstanding view is that thickening, especially if it is continuous with shear

rate, is predominantly driven by hydrodynamic interactions [3, 20, 22]. Figure 1.5 schematically illustrates the evolution in the suspension microstructure according to this interpretation of the shear thickening. Near equilibrium, the resistance to flow is naturally high, as shearing a suspension characterised by random distribution of particles causes them to frequently collide. As the shear rate is increased, the distribution of the particles within the suspension becomes more structured and organised: the flow is streamlined and the increasingly efficient transport of colloidal particles reduces the suspension viscosity (shear thinning). However, Stokesian dynamics simulations demonstrate that hydrodynamics forces become progressively larger for higher shear rates ($Pe \gg 1$), and therefore start to dominate over the interparticle forces that drive Brownian motion. In this scenario, lubrication forces strongly couple the particles' relative motion. As a result, the colloidal dispersion obtains a microstructure significantly different from the near-equilibrium one, and hence, the energy dissipation markedly increases, leading to a shear thickening behaviour.

In both the semidilute and concentrated dispersions, the strong hydrodynamic coupling between particles leads to the formation of hydroclusters, i.e., transient concentration fluctuation driven and sustained by the applied shear field. Such hydroclusters represent the defining feature of the shear-thickening state. Indeed, unlike the seemingly random microstructure observed close to equilibrium, in this scenario the particles distribution is highly organised and anisotropic.

This interpretation of the shear thickening phenomenon has been confuted by recent theoretical [23] numerical [24] [25] and experimental [26] works which describe shear thickening as associated with a transition between the low to the high viscosity in non Brownian suspensions above an onset stress $\sigma^*$. In particular, for values of the stress $\sigma < \sigma^*$, particles do not touch each other, therefore yielding to a lubricated regime, characterised by low values of viscosity. On the other hand, for $\sigma > \sigma^*$, all particles present frictional contact with each other, causing higher values of the suspension viscosity. In this scenario, $\sigma^*$ therefore represents the critical stress value at which shear thickening occurs.

## 1.3 Droplets Suspensions

Within the domain of colloids we can distinguish a class of two-phase systems called *emulsions*, or droplets suspensions. These systems consist of a mixture of two or more liquids that are normally immiscible. Although the terms colloid and emulsion are sometimes used interchangeably, emulsion should refer to the cases where both phases, dispersed and continuous, are liquids. Familiar examples of emulsions include vinaigrettes, homogenized milk and mayonnaise. In this section we give a general overview of the physical properties that describe the behaviour of small droplets, given that they represent the main ingredient forming an emulsion.

### 1.3.1 Surface and Interfacial Tension

Liquid droplets can be generically described as fluid volumes bound by immiscible interfaces characterised by an interfacial tension [27]. To understand the molecular origin of surface or interfacial tension, let us consider the free surface between air and water. While a water molecule in the fluid bulk is surrounded by attractive neighbours, a molecule at the surface is necessarily attracted by a reduced number of neighbours and is therefore in an energetically unfavourable state. Since the creation of a new surface has a high energetic cost, small fluid volumes tend to evolve into spheres. We can define the surface tension of a water molecule as a measure of the energy loss per unit surface area given by the reduced amount of neighbours that a molecule at the surface is interacting with. Indeed, the surface tension can be defined as $\sigma \approx U/2R^2$, where $R$ is the characteristic molecular dimension and $U$ is the total cohesive energy per molecule. This definition shows that the surface tension is inversely proportional to the molecule size, and is described in units of force per unit length or equivalently energy per unit area.

On the other hand, a similar quantity is the interfacial tension, a material property of a fluid-fluid interface whose origins lie in the different attractive intermolecular forces that act in the two neighbouring fluid phases. The result is an interfacial energy per area that acts to resist the creation of new interface. Typical value for interfacial tension is $\sim 1mN/m$, e.g. water/air, water/oil.

### 1.3.2 Droplets shape and dynamics

Fluid droplets may be formed in several ways. For instance, they can form in a gas phase by one of three common routes. First, in response to a vigorous flow, fluid volumes could fragment to filaments and to droplets [28]. Second, droplets may condense from moist air, arising from a temperature drop. Third, vigorous motion within the gaseous phase and associated Bernoulli low pressures can substantially reduce the pressure, thereby facilitating condensation.

An important parameter which characterises droplets shape is the Capillary number $Ca$. The latter represents the relative effect of viscous forces versus surface tension acting across an interface between a liquid and gas, or between two immiscible fluids, and it can be defined as

$$Ca = \frac{\eta V}{\sigma} \tag{1.14}$$

where $\eta$ is the dynamic viscosity of the liquid, $V$ is a characteristic velocity and $\sigma$ is the surface tension or interfacial tension between the two fluid phases. Interfacial and surface tension are very similar properties, and their distinction is only based on where they occur. Indeed, surface tension is defined to a single liquid surface, whereas the interfacial tension is defined to the interface of two immiscible liquids.

If we consider a droplet falling at a characteristic speed $U$ under the influence of gravity $\mathbf{g} = -g\hat{z}$ through a fluid of density $\rho$, we can define a characteristic droplet capillary length as $l_c = (\sigma/(\rho g))^{1/2}$. At length scales corresponding to this capillary length ($lc \sim 2mm$), we observe that the forces induced by gravity and the ones induced by the surface tension are comparable. Provided that the droplets are smaller than the capillary length, they will be dominated by the influence of surface tension: when placed on a surface, their tendency to keep their spherical shape overcomes their tendency to flatten in response to gravity.

Nevertheless, the droplets shape is naturally influenced by the flow of the underlying fluid [29], characterised by the Reynolds number. The latter is defined as $Re = uL/\nu$, where $u$ is the fluid velocity, $L$ is the characteristic linear dimension and $\nu$ is the fluid kinematic viscosity. Given its definition, the Reynolds number prescribes the relative magnitudes of inertial and viscous forces in the system under study. In particular, for low Reynolds number, small droplets retain a

markedly spherical form as the surface tension contribution prevails. As the Reynolds number $Re$ is increased, both the droplet shape and the form of the flow dramatically change. The first effect of dynamic pressure on the shape of the droplet is to distort it into an oblate ellipsoid. As the Reynolds number is further increased, a stable wake adjoins the droplet therefore breaking its for-aft symmetry. Eventually, at high $Re$ the droplet's speed will increase to the point that the associated dynamic pressure will cause droplet cleavage.

### 1.3.3 Wetting properties

Wetting is a physical phenomenon which arises when any liquid-gas interface comes into contact with a solid [27], and it deeply affects the dynamics of the system. The degree of wetting is usually determined by a variety of factors including the topography of the solid interface and the material properties of both the fluid and solid phases. Considering a liquid interface with interfacial tension $\sigma$ in contact with a solid, we can define the two relevant interfacial free energies $\gamma_{SL}$ and $\gamma_{SG}$ referring to the wet and dry surface, respectively.

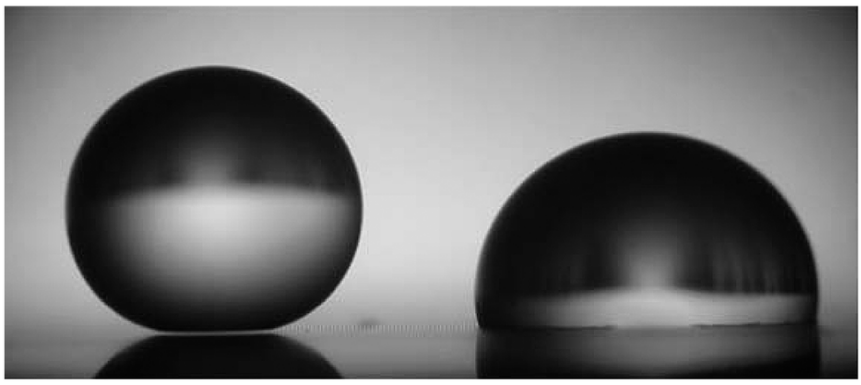

**Figure 1.4** *Millimetric water droplets deposited on a superhydrophobic substrate. The picture has been taken from [5].*

The relative magnitude of the three surface free energies $\sigma$, $\gamma_{SL}$ and $\gamma_{SG}$ defines

the tendency of the liquid to wet the solid through the spreading parameter $S = \gamma_{SG} - (\gamma_{SL} + \sigma)$. A value of $S > 0$ indicates a fluid that will spread completely into a thin film, as the surface tension of the solid material is lower in the wet phase than in the dry one. This is the case for most oils spreading on solid surfaces. Conversely, when $S < 0$ it is energetically favourable for the solid to stay dry, and the fluid will retain its semi-spherical droplet shape with a finite equilibrium contact angle $\theta_e$. The latter can be calculated using the expression $\sigma \cos\theta_e = \gamma_{SG} - \gamma_{SL}$, known as Young's relation. The value of the contact angle $\theta_e$ defines the degree of wetting: $\theta_e = 0$ corresponds to complete wetting, $\theta_e \geq 90$ and $\theta_e \leq 90$ define an hydrophobic or hydrophilic surface, respectively.

### 1.3.4 Droplets Coalescence

In nature, droplets often arise in the form of suspensions. The high density of droplets within a suspension as well as the dependence of their speed and transport properties on their size, enhance the probability of observing coalescence, a common phenomenon that has received extensive study [30, 31].

The easiest way of observing coalescence is considering a water droplet placed on a quiescent water bath. As we expect, the droplet will ultimately merge within the bath, collapsing into it due to the gravitational force. Such coalescence however is delayed by the thin layer of air present between the droplet and the underlying surface. Indeed, in order for the droplet to merge, this layer needs to become thin enough so that the Van der Waals forces between droplet and bath become predominant. The resulting coalescence can be either complete, i.e the entire drop merges within the bath, or partial, i.e. only a fraction of the droplet coalesces, leaving behind a smaller daughter droplet that is ejected from the bath and eventually undergoes partial coalescence as well. This cascade continues until the daughter droplet becomes sufficiently small that viscosity comes into play and complete coalescence occurs.

Droplet-droplet coalescence, occurring for example inside the clouds, presents a similar physical scenario. Indeed, considering two droplets that come into contact, provided that the impact time is greater than the drainage time of the layer of air in between them, the two droplets will merge into a single bigger one.

Nevertheless, an emulsion, or droplet suspension, can be stabilised and coalescence avoided by increasing the repulsion between the dispersed phase, i.e. by

increasing the steric repulsion (short range) or the electrostatic repulsion (long range). Experimentally, a way to avoid droplet coalescence in an emulsion is adding surfactants. Surfactants, or emulsifiers, are compounds that lower the surface tension (or interfacial tension) between two phases and therefore contribute to the stabilisation of the dispersed droplets, via electrostatic or steric effects.

## 1.4 Experimental methods for emulsions

Emulsions are widely used as a means of transport of value-added materials that can be composed of potentially volatile substances that are safely encased within the surrounding fluid. The earliest techniques for forming these kind of materials come from food science. For example, butter has been created through the processing of milk solids into semi-solid phases that are composed of water droplets dispersed in milk fats. Nowadays, emulsions provide versatility in a variety of applications that require deep and fundamental understanding of their creation and properties, making them object of extensive and continuous study [32].

The simplest emulsions are thermodynamically metastable fluid droplets suspended within a second fluid, therefore forming a mixture. In particular, the creation of an emulsion requires a substantial amount of energy, while a deep understanding of the physiochemical properties of the diverse macromolecular components is required for emulsion stability. In order to obtain a stable emulsion and preventing the phase separation of the liquid components, an emulsifier, or surfactant, must be added to the system. In general, surfactants are surface-active compounds which promotes the formation and long-term stability of emulsions. Examples of surfactants can be found in powdered silica, minerals, lattices, proteins and block copolymers. Since emulsion are not in thermodynamic equilibrium, their formation requires the addition of energy, usually through stirring, shaking or vibration. In particular, as the mechanical work generates shear forces on the liquid-liquid interface that exceed the cohesive forces of the dispersing liquid, droplets are formed. The size of the droplets is in general a complicate function of the local shear forces in the system and the surface tension between the two fluids.

In general, in an emulsion the surfactants play two important roles. First, they

lower the surface tension between the two fluids, therefore reducing the work and energy necessary to create the droplets. On the other hand, the second role of the surfactant is to coat the outside of the droplets, acting as a physical barrier between the different phases of the system. As a consequence, the surfactant isolates the individual droplets from the continuous phase as well as from each other, therefore ultimately preventing their coalescence.

*Microfluidics.* An important experimental method for the creation of emulsion is given by microfluidics. Microfluidics devices, produced using soft lithography methods or with pulled microcapillaroties, can be used to create droplet-on-demand emulsions for micro-encapsulation of materials. In this environment, as shown in Fig. 1.4, each drop is largely independent from their surroundings and from other droplets. Moreover, by controlling the relative ratios of dispersed phase constituents, fine control of each droplet's content can be achieved on a pico- to nanoliter volumes. Microfluidic emulsion generators generally rely on hydrodynamic flow as the main physical mechanism for creating droplets, usually within the context of low Reynolds number flow ($Re \sim 10^{-6} - 10^{1}$).

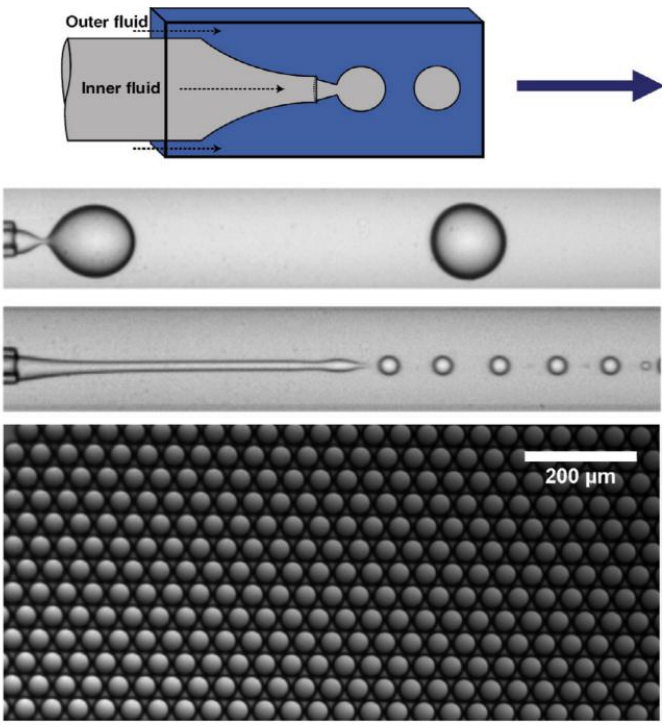


**Figure 1.4** *Single emulsions in a co-flow microfluidic device. The image is adapted from [6].*

## 1.5 Rheology

As we previously mentioned, in order to be able to describe the properties defining the behaviour of a colloidal suspension, we need to understand its response to deformation. This area of study, which aims to characterise the mechanical response of a material to an external deformation is known as *rheology*. We now give a general overview of the field of *rheology* [33] [34].

To understand the premises of rheology, we can imagine squeezing with our hand a small cube (about $1cm$ in size) of a suspension containing around $N \approx 10^{11}$ particles. As physicists, ideally we would like to have access to all particle positions $\{x^\alpha\}$ and velocities $\{v^\alpha\}$ as well as the velocity of the suspending fluid at every point. In this way, knowing the kind of interactions between particles, we would be able to solve all the particles' Newton equations and therefore exactly determine their dynamics. However, in practise, the exact particles' positions and velocities are not accessible, and solving the $3N$ equation of motion would certainly be far too demanding, and arguably not that useful, a task. Nevertheless, we can find some macroscopic observables that we can probe, for instance the force, or stress we exert while squeezing our suspension sample. This stress is related to the particles configuration in the suspension in an analogous way as the temperature and pressure are related to the microstates explored by the system in equilibrium thermodynamics. Given this strong relation between the microscopic and macroscopic properties, the fundamental premise of rheology is to characterise the macroscopic response of the system to deformation without explicitly worrying about all microscopic details.

In rheology, we assume to be able to treat the suspension as a continuous medium composed of *material elements* with volume $V$ each enclosing numerous particles. Moreover, these volume elements are chosen to be small with respect to the volume of the entire suspension. In this way, instead of considering the velocity of each particle, we can define a velocity vector field $\bar{v}(x)$ given by the average velocity of all particles and fluid enclosed in the material element. In an analogous way, we can describe the forces acting on each particles and on the fluid defining a stress tensor $\bar{\sigma}(x)$. We can then relate the particle position to a strain tensor $\bar{\epsilon}(x)$, and the particle number within the material element to a density field $\bar{\rho}(x)$.

### 1.5.1 Rheology of continua: stress and strain tensor

When applying an external force, we are interested in characterising the deformation induced on the overall system. Two important quantities, which give insight on the state of deformation of a material, are given by the stress and strain tensor.

Let's consider a material subjected to an external force, and denote with $x_i$ the components of the position vector $\mathbf{r}$, which describes the position of any point within the body. After the deformation, every point is generally displaced, and the components describing the new positions will be $x_i'$. We can therefore define a displacement vector $u_i$, due to the deformation, as

$$u_i = x_i' - x_i. \tag{1.15}$$

Naturally, the new coordinates $x_i'$ will depend on the old $x_i$ and, as a consequence, the displacement vector $u_i$ will also be dependent on $x_i$. In particular, if we can describe $u_i$ for any given $x_i$, the deformation of the body is entirely determined. Let's consider two points very close to each other, joined together by a vector $dx_i$ before the deformation. The vector joining the same two points this time of the deformed body will be $dx_i' = dx_i + du_i$. Using the Einstein convention (summation is implied over repeated indices), we can write the distance between two points as $dl = \sum_i {dx_i}^2$ before the deformation, and as $dl' = \sum_i {dx_i'}^2 = \sum_i (dx_i + du_i)^2$. Substituting $du_i$ with $du_i = (\partial u_i / \partial x_k) dx_k$,. we obtain [35]

$$dl' = dl^2 + 2\frac{\partial u_i}{\partial x_k} dx_i dx_k + \frac{\partial u_i}{\partial x_k}\frac{\partial u_i}{\partial x_l} dx_k dx_l. \tag{1.16}$$

Since the sum is taken over both indexes $i$ and $k$, the second term on the right hand side of the equation (1.16) can be written in the explicitly symmetrical form

$$\left(\frac{\partial u_i}{\partial x_k} + \frac{\partial u_k}{\partial x_i}\right) dx_i dx_k. \tag{1.17}$$

We can therefore express the vector $dl'$ in the final form

$$dl'^2 = dl^2 + 2u_{ik} dx_i dx_k \tag{1.18}$$

where $u_{ik}$ is the *strain tensor*, and it is defined as

$$u_{ik} = \frac{1}{2}\Big(\frac{\partial u_i}{\partial x_k} + \frac{\partial u_k}{\partial x_i} + \frac{\partial u_l}{\partial x_i}\frac{\partial u_l}{\partial x_k}\Big). \tag{1.19}$$

The strain tensor measures the deformation of the material element and therefore vanishes for translation and rotation. From its definition, we can notice that this tensor is symmetrical i.e., $u_{ik} = u_{ki}$. Moreover, its diagonal elements correspond to the fractional change in length of the material element in the $i^{th}$ direction, while its trace is related to the fractional change in volume.

In most cases, $u_i$ and their derivatives are small for small deformations, and we can therefore neglect the last term in (1.19), obtaining [35] [36]

$$u_{ik} = \frac{1}{2}\Big(\frac{\partial u_i}{\partial x_k} + \frac{\partial u_k}{\partial x_i}\Big). \tag{1.20}$$

In an analogous way, we can define the *strain rate tensor* $\epsilon_{ij}$, as

$$\epsilon_{ij} = \frac{1}{2}\Big(\frac{\partial v_i}{\partial x_j} + \frac{\partial v_j}{\partial x_i}\Big), \tag{1.21}$$

where $\mathbf{v}(x,t)$ is the local velocity field. Like the strain tensor, also the strain rate tensor $\epsilon_{ij}$ is symmetric, i.e. $\epsilon_{ij} = \epsilon_{ji}$.

In this thesis we will only consider *incompressible* fluids, i.e. materials where the volume of each material element and hence the local density $\bar{\rho}(x)$ is unchanged by deformation. Physically, this can be explained by the fact that the bulk moduli of most liquids are of the order of $\approx 10^9 Pa$, orders of magnitudes greater than the shear stresses typically encountered in soft matter ($\sigma \approx 1 - 10^4 Ps$ ). Therefore, in practice, both $u_{ij}$ and $\epsilon_{ij}$ are traceless: for fluids, this corresponds to the condition

$$\bar{\nabla} \cdot \mathbf{v} = \mathbf{0}. \tag{1.22}$$

In a body that is not deformed, the arrangement of all its molecules corresponds to a state of thermal and mechanical equilibrium, where the sum of all forces at each point is zero. On the other hand, when a deformation occurs, the arrangement of the molecules is changed and the system is removed from its original state of equilibrium. In turn, forces arise in order to bring back the

system to its equilibrium phase. Such internal forces, which occur when a body is under deformation and are due to molecular forces, are called *internal stresses*.

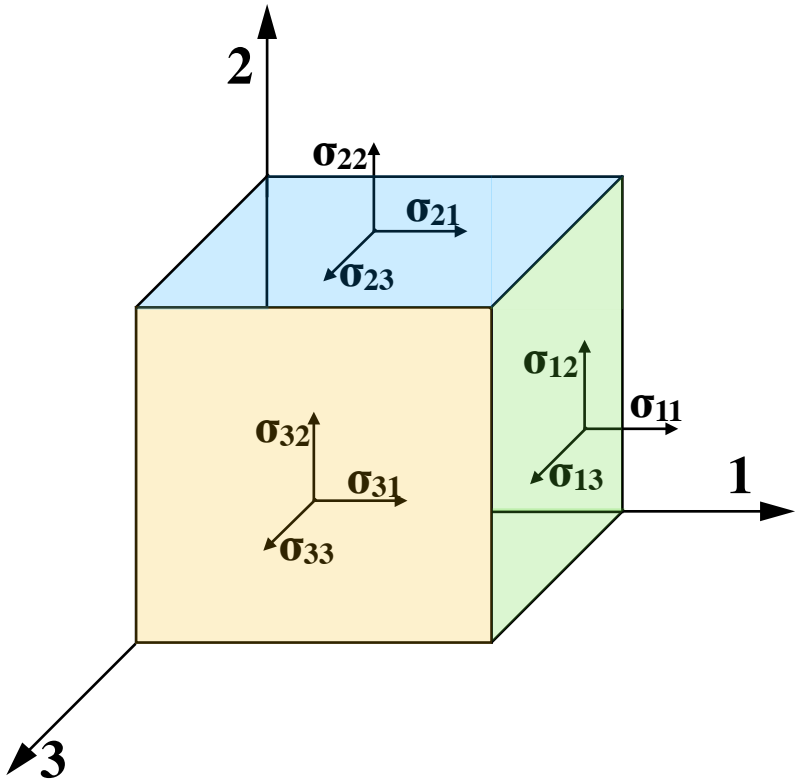


**Figure 1.6** *Schematic representation of the components of the stress tensor $\sigma_{ij}$ for a material element.*

The total force acting on a portion of the body corresponds to the sum of all forces an all the volume elements in that portion of the body and can therefore written as the volume integral $\int \mathbf{F} dV$. Since inside this portion of the body all forces cancel one another due to Newton's Third law, the total force can therefore be regarded as the sum of the forces exerted on the given portion of the body by the portions surrounding it. The resultant force can therefore be represented as the sum of forces acting on all the surface elements, i.e. as an integral over the surface. Thus, for any portion of the body the volume integral of the force can be transformed into an integral over the surface which implies that the vector $\mathbf{F}$ must be the divergence of a tensor of rank two, i.e. in index notation,

$$F_i = \frac{\partial \sigma_{ik}}{\partial x_k} \tag{1.23}$$

and we can write

$$\int F_i dV = \int \frac{\partial \sigma_{ik}}{\partial x_k} dV = \oint \sigma_{ik} df_k. \tag{1.24}$$

The quantity $\sigma_{ik}$ is called *stress tensor* and corresponds to the force per unit area in the k-th direction exerted on the plane with the normal vector k-th direction, while the quantity $\sigma_{ik} df_k$ represents the i-th component of the force on the surface element $df$.

In general, the force per unit volume of a material element can be written as being composed of two contributions

$$F_i = F_i^* + \frac{\partial \sigma_{ij}}{\partial x_j} \tag{1.25}$$

where the repeated indexes implies summation. In equation (1.25) the second term on the right hand side is related to the stress tensor as described in (1.23), while the term $F_i^*$ represents the body forces acting per unit volume on all elements in a continuum [37], e.g. gravity.

The stress tensor, depicted in Figure 1.6, can be expressed in matrix form as follows

$$\sigma_{ij} = \begin{pmatrix} \sigma_{11} & \sigma_{12} & \sigma_{13} \\ \sigma_{21} & \sigma_{22} & \sigma_{23} \\ \sigma_{31} & \sigma_{32} & \sigma_{33} \end{pmatrix}.$$

The diagonal components $\sigma_{11}$, $\sigma_{22}$ and $\sigma_{33}$ represent the normal stresses, while the off-diagonal ones represent the shear stresses. The stress tensor $\sigma_{ij}$ is conventionally decomposed into an isotropic and deviatoric part,

$$\sigma_{ij} = - = p\delta_{ij} + \tau_{ij} \tag{1.26}$$

where $\delta_{ij}$ is the Kronecker delta,

$$p = -\frac{1}{3}\sigma_{ij} = -\frac{1}{3}(\sigma_{11} + \sigma_{22} + \sigma_{33}) \tag{1.27}$$

represents the mechanical pressure, and $\tau_{ij}$ is the traceless deviatoric stress tensor ($\tau_{ii} = 0$).

Requiring that the net torque on each material element is zero at every time, even in absence of mechanical equilibrium, corresponds to requiring that the stress tensor is symmetric, i.e. $\sigma_{ij} = \sigma_{ji}$, so that there are only six independent stress components. Nevertheless, for a particles suspension, $\sigma_{ij}$ is not a priori symmetric: indeed, two particles in contact with static friction will exert a torque on each other. However, as discussed in [36], the stress tensor $\sigma_{ij}$ for a suspension become symmetric if we consider the averaging volume $V$ of the material element to be large enough. It is however important to notice that while in theory it is always possible to reduce the stress tensor to its symmetrical form, there are cases where it is useful to describe the stress tensor as antisymmetric, for example for systems like liquid crystals.

When a body is under mechanical equilibrium, the forces on each material element vanish, $F = 0$, yielding Cauchy's equation

$$F_i^* + \frac{\partial \sigma_{ij}}{\partial x_j} = 0. \tag{1.28}$$

For a Newtonian fluid, such condition implies steady flow, while for an elastic solid it implies a deformation which is constant over time.

The stress and strain rate tensor described above in a fluid flowing at steady state are related by a function known as a *constitutive equation*. The simplest form of such an equation is for a Newtonian fluid, and can be written as

$$\sigma_{ij} = -p\delta_{ij} + 2\eta\epsilon_{ij}, \tag{1.29}$$

where $\sigma_{ij}$ and $\epsilon_{ij}$ are linearly related, and the coefficient $\eta$ is the shear viscosity of the fluid. In the case of a simple shear flow with a velocity gradient within two planes, (1.29) reduces to

$$\sigma_{12} = \eta\dot{\gamma} \tag{1.30}$$

where $\dot{\gamma}$ is the shear rate.

### 1.5.2 Non Newtonian fluids

Newtonian fluids are characterised by a stress tensor with equal normal components, i.e. $\sigma_{11} = \sigma_{22} = \sigma_{33} = -(1/3)p$. However, in most complex fluids this is not true, and the stress tensor can no longer be written in the form of eq.(1.29) [38]. Such kind of fluids are called *non Newtonian*.

For the case of an incompressible material $\sigma_{ij}$ is only defined up to an additive (isotropic) pressure and it therefore follows that there are only three independent stresses of rheological significance: the shear stress $\sigma_{12}$ and the first and second normal stress difference defined as $N_1 = \sigma_{11} - \sigma_{22}$ and $N_2 = \sigma_{22} - \sigma_{33}$. Typically, it is assumed that these stresses depend only on the local value of the shear rate $\dot{\gamma}$, so that $\sigma_{12} = \sigma(\dot{\gamma}), N_1 = N_1(\dot{\gamma})$ and $N_2 = N_2(\dot{\gamma})$ [39].

Although at high concentration the flow of a generic suspension is non-Newtonian, there are some special cases, for instance the case of wet granular flow, where all components of the stress tensor $\sigma_{ij}$ scale linearly with the strain rate $\dot{\gamma}$. In this case, the rheology is called *quasi-Newtonian* and the stress tensor can be written as

$$\sigma_{ij} = H_{ij}\dot{\gamma} \begin{pmatrix} H_{11} & \eta & 0 \\ \eta & H_{22} & 0 \\ 0 & 0 & H_{33} \end{pmatrix} .\dot{\gamma},$$

where $H$ is a constant tensor.

Generally, $N_1(\dot{\gamma})$, $N_2(\dot{\gamma})$ and $\eta(\dot{\gamma})$ present a different dependence on $\dot{\gamma}$. Figure 1.6 shows the different possible dependence of the stress tensor $\sigma_{12}$ on $\dot{\gamma}$, for four types of fluids. For each case, the gradient of the curve corresponds to the shear viscosity $\eta$. If $\eta$ decreases with $\dot{\gamma}$, the fluid is said to be *shear thinning*. On the other hand, if $\eta$ increases with $\dot{\gamma}$, the fluid shows a *shear thickening* behaviour. In *yield stress fluids*, a critical stress $\sigma_Y$, known as yield stress, needs to be exceeded in order for the fluid to flow.

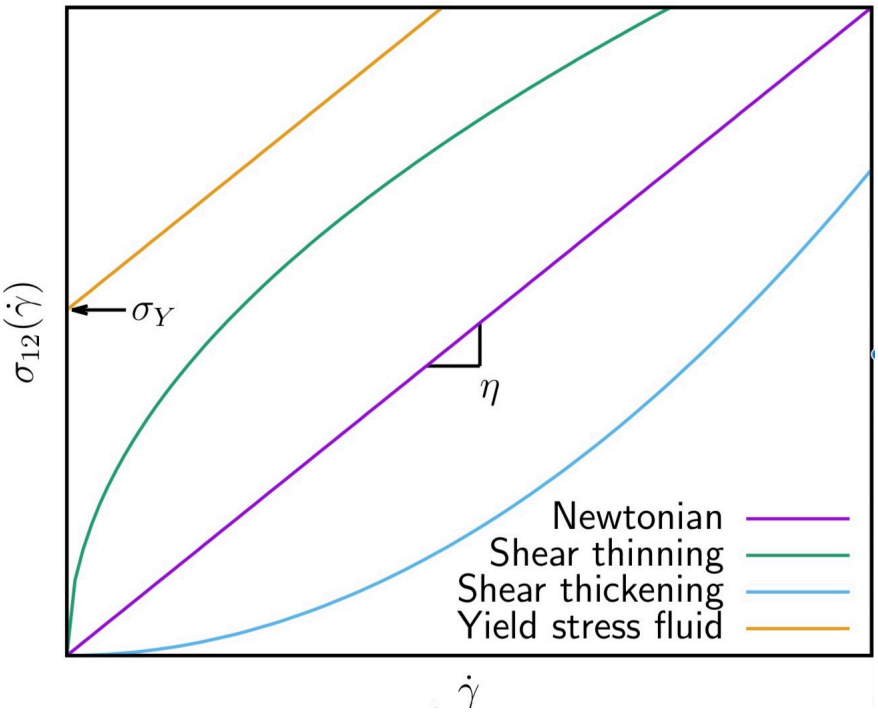


**Figure 1.6** *Schematic representation of the flow curves $\sigma_{12}(\dot{\gamma})$ for different types of fluids (labelled in the Figure). This figure is taken from [1]*

### 1.5.3 Thesis structure

In this thesis we present a computational study aiming to characterise the rheological properties of a deformable droplet suspension.

In Chapter 2 we describe the computational model used to perform our simulations, giving a general overview of the Lattice Boltzmann method and its implementation in our program. The following three Chapters, 3, 4 and 5 present the results obtained with our research.

Chapter 3 is dedicated to the study of the rheology of a suspension of soft deformable droplets subjected to a pressure-driven flow. We measure the apparent viscosity as a function of droplet concentration and pressure gradient, and provide evidence of a discontinuous shear thinning behaviour, which occurs at a concentration-dependent value of the forcing. We further show that this response is associated with a nonequilibrium transition between a hard (or less deformable) phase, which is nearly jammed and flows very slowly, and a soft (or more deformable) phase, which flows much more easily. Close to the transition, we find sustained oscillations in both the droplet and fluid velocities. Polydisperse systems show similar phenomenology but with a smoother transition, and less

regular oscillations.

In Chapter 4 we elucidate the role of deformability on colloidal flow, measuring the apparent viscosity of a system of droplets of variable surface tension subjected to a pressure-driven flow. We confirm that our suspension generically undergoes discontinuous shear thinning, and determine the dependence of the location of the discontinuity on surface tension. We find that the effective viscosity of the suspension is mainly determined by a capillary number. We then present active microrheology simulations, where a single droplet is dragged through the suspension. These also show a dynamical phase transition, analogous to the one associated with discontinuous shear thinning in our interpretation. Such a transition is signalled by a discontinuity in the droplet velocity versus applied force.

Chapter 5 presents a study of the reversibility properties of our deformable droplets suspension. Using a similar computational model as in Chapter 3 and 4, we now use two different methods to test the reversibility properties of our system: an oscillatory shear, and a periodically inflating a deflating droplet within our suspension. The position of all droplets is carefully tracked during the periodic oscillation or inflation/deflation of the central droplet, in order to be able to compare the position of all droplets every period of the imposed deformation. We were therefore able to distinguish a transition between a reversible phase, where each droplet gets back to its original position after each period of deformation, and an irreversible one, where the imposed deformation on the suspension induces a random change in the position of all droplets. Moreover, tracking the droplets position over time, we distinguish a limit cycle behaviour, where some droplets repeatedly follow the same circular path every period of deformation.

We conclude our thesis with a brief chapter (Chapter 6), with our conclusive remarks on the overall research developed in this work.

# Chapter 2

# Hybrid Lattice Boltzmann Method

In order to investigate the properties of complex fluids through numerical simulations, a common approach is to analyse the hydrodynamics of a binary fluid. To this end, we need the equations of motion of a conserved order parameter describing the composition of our binary fluid to be coupled with the Navier-Stokes equation via the fluid velocity $\vec{v}$. In particular, in this thesis we will be solving the dynamics of a conserved order parameter ($\phi$), coupled with the incompressible Navier-Stokes equation:

$$\rho\Big(\frac{\partial}{\partial t} + \mathbf{u}\cdot\nabla\Big)\mathbf{u} = -\nabla P + \eta\nabla^2\mathbf{u} + \mathbf{f} \tag{2.1}$$

$$\nabla\cdot\mathbf{u} = 0. \tag{2.2}$$

Here, $\eta$ represents the fluid viscosity, $P$ the pressure, $\mathbf{u}$ the fluid velocity and $\mathbf{f}$ is the force density acting on the fluid. Considering the case where the force density $\mathbf{f}$ originates from a short-range intermolecular interactions, this quantity can be expressed also as the divergence of the hydrodynamic stress tensor as $\mathbf{f} = \nabla\cdot\sigma(\phi)$, thus providing the coupling with the order parameter $\phi$. In our case we can write this term as $\mathbf{f} = -\phi\nabla\mu$, where $\mu$ denotes the chemical potential.

On the other hand, the dynamics of a conserved order parameter $\phi$ is regulated

by the Cahn-Hilliard equation:

$$\frac{\partial \phi}{\partial t} + \mathbf{u} \cdot \nabla \phi = -\nabla \cdot \mathbf{J} \tag{2.3}$$

where the flux $\mathbf{J}$ is defined as $-\nabla \mathcal{F}$, and $\mathcal{F}$ is the system free energy functional of $\phi$. While a finite difference method is implemented in order to solve the Cahn-Hilliard equation, for the Navier-Stokes we use the Hybrid Lattice Boltzmann method, which is briefly explained in the next section. More details about these techniques can be found in Refs[40–44].

## 2.1 The Lattice Boltzmann Equation

We can think of the Lattice Boltzmann equation (LB) as deriving from the discretization of the general Boltzmann equation:

$$\frac{\partial f}{\partial t} + \mathbf{v} \cdot \nabla_x f + \frac{\mathbf{F}}{m} \cdot \nabla_{\mathbf{v}} f = \left(\frac{\partial f}{\partial t}\right)_{coll} \tag{2.4}$$

where $f(\mathbf{x}, \mathbf{v}, t)$ represents the distribution function, in the phase space, of the system's particles, subjected to the force $\mathbf{F}$ acting on them. The main difficulty in numerically solving the incompressible Navier-Stokes equation lies on the fact that the fluid velocity $\mathbf{v}$ needs to be updated at each timestep while simultaneously satisfying the constraint $\nabla \cdot \mathbf{v} = 0$. The LB scheme helps us avoiding this challenge by introducing a mesoscopic distribution function $f(\mathbf{x}_i, \mathbf{v}_i, t)$, defined as the average number of fluid particles at position $\mathbf{x}_i$ and with velocity $\mathbf{v}_i$ at time $t$. In this way, rather than explicitly solving the equation for the fluid velocity $\mathbf{v}$, we can evaluate the dynamics of the overall distribution function which, in LB, depends on discretised positions and velocities. Indeed, in LB the position vector $\mathbf{x}$ is discretised as a d-dimensional lattice, spaced every $\Delta x = \Delta y = \Delta z$. Simultaneously, the particles' velocities are also discretized such that only a finite set of directions for $\mathbf{v}$, namely $\{\mathbf{e}_0, \ldots, \mathbf{e}_l\}$, is accessible. In $3D$ one could choose

to set $l = 14$ as follows:

$$\begin{cases} \mathbf{e}_0 = (0,0,0) \\ \mathbf{e}_{1-6} = (0,0,\pm c),(0,\pm c,0),(\pm c,0,0) \\ \mathbf{e}_{7-14} = (\pm c,\pm c,\pm c) \end{cases} \tag{2.5}$$

where $c = \frac{\Delta x}{\Delta t}$. It is common practice to set the lattice space, mass and timestep to unity, $\Delta x = m = \Delta t = 1$. For simplicity, we will refer to this distribution function as $f_i(\mathbf{x}, t)$ where the subscript $i$ labels the lattice velocities. The distribution function $f(\mathbf{x}, t)$ can provide us with the physical observables, namely the fluid density $\rho(\mathbf{x}, t)$ and the fluid velocity $\mathbf{u}(\mathbf{x}, t)$, which can be derived as

$$\rho(\mathbf{x}, t) = \sum_i f_i(\mathbf{x}, t) \tag{2.6}$$

$$\mathbf{u}(\mathbf{x}, t) = \frac{1}{\rho(\mathbf{x}, t)} \sum_i f_i(\mathbf{x}, t)\mathbf{e}_i \tag{2.7}$$

The dynamics of the distribution function $f(\mathbf{x}, t)$ is regulated by the local Lattice Boltzmann Equation, which, in the BGK approximation characterised by a single relaxation time $\tau$, is defined as

$$\underbrace{f_i(\mathbf{x} + \mathbf{e}_i\Delta t, t + \Delta t) = f_i(\mathbf{x}, t)}_{\textbf{Streaming}} + \Delta t F_i - \Delta t \underbrace{\frac{f_i(\mathbf{x}, t) - f_i^{eq}(\mathbf{x}, t)}{\tau}}_{\textbf{Collision}}. \tag{2.8}$$

Here $\tau$ is the relaxation timescale for $f_i$ to reach its equilibrium value, and is at the same time related to the macroscopic fluid viscosity $\eta$ as $\eta = \frac{\rho\tau}{3}$ . The collision term in (2.4) is here approximated as the difference between the distribution function $f_i$ and its local equilibrium value $f_i^{eq}$. The latter, in the continuous Boltzmann equation is given by the Maxwell-Boltzmann equation:

$$f^{eq}(\mathbf{v}) = \frac{\rho}{(2\pi T)^{2/3}} e^{-(v-u)^2/2T} \tag{2.9}$$

where here $\mathbf{v}$ is a continuous variable, and $T$ is the system temperature. In the case where the particles' velocities are discretized, as in our Lattice Boltzmann

method, a polynomial expansion in $\mathbf{v}_i$ and $\vec{u}$ has to be introduced to approximate the Maxwell-Boltzmann equilibrium distribution (2.9), thus obtaining

$$f^{eq}(\mathbf{v}_i) = A_i + B_i \mathbf{u} \cdot \mathbf{v}_i + C_i u^2 + D_i \vec{u}\vec{u} : \vec{v}_i\vec{v}_i + \underline{\underline{E_i}} : \vec{v}_i\vec{v}_i \tag{2.10}$$

for $i = 1 \dots l$.

### 2.1.1 Chapman-Enskog expansion

While the form of the Navier-Stokes equation can be obtained by phenomenological reasoning, it is possible to formally derive it from the Boltzmann equation. Indeed, the application of specific models for the microscopic collision process can lead to explicit formulas for the transport coefficients and a formal derivation of the Navier-Stokes equation. This process, developed between 1910 and 1920, goes under the name of the Chapman-Enskog expansion. In order to give an idea of how it is possible to obtain the Navier-Stokes equation from the Lattice Boltzmann one, in this section we provide the first steps of the Chapman-Enskog expansion. In particular, we show how to derive the continuity equation for the density, as iterating the same mechanism for higher orders in the expansion (after some more pages of calculations), the Navier-Stokes equation can be recovered.

In particular, starting from the Lattice Boltzmann equation(2.4), it is possible to obtain the Navier-Stokes equation (2.1) by expanding the distribution function $f$ as follows

$$f = f^{(0)} + \epsilon f^{(1)} + \epsilon^2 f^{(2)} + \dots \tag{2.11}$$

where $\epsilon$ is a small parameter, $f^{(1)} \sim \mathcal{O}(\partial)$, $f^{(2)} \sim \mathcal{O}(\partial^2)$ and we stop at the $2^{nd}$ order. Inserting (2.11) into the Lattice Boltzmann equation (2.4), we obtain an identity for each order that we compare ($o^{th}, 1^{st}$ and $2^{nd}$). We than impose the

following four constraints, which ensure physical meaning:

$$\begin{cases} \sum_i f_i^{eq} = \rho \\ \sum_i f_i^{eq} e_{i\alpha} = \rho v_\alpha \\ \sum_i f_i^{eq} e_{i\alpha} e_{i\beta} = p\delta_{\alpha\beta} + \rho v_\alpha v_\beta \\ \sum_i f_i^{eq} e_{i\alpha} e_{i\beta} e_{i\gamma} = \frac{p}{3}(v_\alpha \delta_{\beta\gamma} + v_\beta \delta_{\alpha\gamma} + v_\gamma \delta_{\alpha\beta}) \end{cases} \tag{2.12}$$

where $v$ is the fluid velocity, $\rho$ represents its density and $p$ is the pressure. Comparing the different differential orders of the LB equation, and taking into account the above constraints we are able to obtain the Navier-Stokes equation (2.1) as well as the continuity equation for the density

$$\frac{\partial \rho}{\partial t} + \nabla(\rho \mathbf{u}) = 0. \tag{2.13}$$

To give an idea about how this can be done, we will show the steps that lead to the density continuity equation (2.13). First, we can rewrite the first term in (2.4) as

$$\begin{aligned} f_i(\mathbf{x} + \mathbf{v}_i \Delta t, t + \Delta t) &\approx_{\Delta t \longrightarrow 0} f_i(\mathbf{x}, \mathbf{v}_i, t) + \Delta t \underbrace{(\partial_t + e_{i\alpha}\partial_\alpha)}_{D} f_i(\mathbf{x}, t) \\ &\approx f_i(\mathbf{x}, t) + \Delta t D f_i(\mathbf{x}, t) + \frac{\Delta t^2}{2} D^2 f_i(\mathbf{x}, t) + \dots \end{aligned} \tag{2.14}$$

Plugging the last equation into (2.4), we obtain:

$$D f_i(\mathbf{x}, t) + \frac{\Delta t}{2} D^2 f_i(\mathbf{x}, t) = \frac{f^{eq} - f_i(\mathbf{x}, t)}{\tau}. \tag{2.15}$$

We can now separately compare the $0^{th}, 1st$ and $2^{nd}$ asymptotic orders, obtaining:

$$\begin{cases} O(\partial^0) : \frac{f_i^{eq} - f_i^{(0)}}{\tau} = 0 \longleftrightarrow f_i^{eq} = f_i^{(0)} \\ O(\partial^1) : D f_i^0 = \frac{f_i^{(1)}}{\tau} \longleftrightarrow f_i^{(1)} = -\tau D f_i^{eq} \\ O(\partial^2) : f_i^{(2)} = \tau\left(\tau - \frac{\Delta t}{2}\right) D^2 f_i^{eq}. \end{cases} \tag{2.16}$$

From the definition of the fluid density $\rho$ (2.6), we therefore obtain

$$\begin{aligned}\rho &= \sum_i (f_i^{(0)} + f_i^{(1)} + f_i^{(2)}) \\ &= \sum_i f_i^{eq} - \tau \sum_i D f_i^{eq} + \tau\Big(\tau - \frac{\Delta t}{2}\Big) \sum_i D^2 f_i^{eq}\end{aligned} \tag{2.17}$$

Considering now the first of the four constraints in (2.12), the above equation becomes

$$\sum_i D f_i^{eq} = \Big(\tau - \frac{\Delta t}{2}\Big) \sum_i D^2 f_i^{eq}. \tag{2.18}$$

Therefore, if we consider only the terms of $o^{th}$ order:

$$\partial_t \underbrace{\sum_i f_i^{eq}}_{\rho} + \underbrace{\partial_\alpha \sum_i f_i^{(0)} e_{i\alpha}}_{\rho v_\alpha} = O^{(2)} \tag{2.19}$$

thus giving the continuity equation for the density (2.13) (up to order $\mathcal{O}(\partial^2)$). In order to obtain the Navier-Stokes equation, as mentioned before, similar steps must be followed, taking into account the constraints (2.12) and considering higher orders of momenta.

## 2.2 Forcing term in the Lattice Boltzmann model

There is a wide range of fluid problems in which the presence of an external force, for example gravity, significantly affects the dynamics of the overall system. For this reason, a number of techniques have been implemented in order to be able to add a forcing term on the Lattice Boltzmann scheme [45]. In what follows we present the most common techniques useful for this purpose.

When a body-force like gravity is included in the Navier-Stokes equation it is common to express the force terms of the gravitational potential: $-\rho\nabla\Psi$. With this approach, assuming that the density variation produced by the body-force is negligible, the Navier-Stokes equation incorporating the body-force can be

expressed in the same form as in the absence of gravity but with an altered pressure: $p \longrightarrow p + \rho\Psi$. A second way of introducing gravity in the Lattice Boltzmann scheme involves considering the momentum change produced by the body-force [46]. In this case, if a body-force $\mathbf{F}$ is acting, then at every timestep there is a change of momentum $\Delta\mathbf{P} = \mathbf{F}$. In order to incorporate this into the model, we can use an equilibrium distribution which now depends on the "equilibrium velocity" $\mathbf{u}^*$ where $\rho\mathbf{u}^* = \rho\mathbf{u} + \tau\mathbf{F}$ and $\tau$ is the relaxation time. To conclude, an external force can also be included into the Lattice Boltzmann scheme in a similar manner to that adopted for the lattice gas model [47]. Here, as we did in our simulations, the force implementation is achieved by adding a term to the collision function that modifies the distribution function. The collision operators are therefore defined as:

$$C_{f_i}(\mathbf{x}, t, f_i) = -\frac{1}{\tau}(f_i(\mathbf{x}, t) - {f_i}^{eq}(\mathbf{x}, t, f_i)) + p_i(\mathbf{x}, t, f_i), \tag{2.20}$$

where $p_i(\mathbf{x}, t, f_i)$ represent the driving terms. While the first method discussed can only be applied in situations where there is no density change across the fluid, the last two methods are less susceptible to density fluctuations. However, we note that the latter produce more accurate results in the cases when analysing steady state solutions.

## 2.3 Order parameter dynamics: Cahn-Hilliard equation

As previously mentioned, the Navier-Stokes equation is coupled to an evolution equation for a set of conserved order parameters $\phi_i$ defining each of the droplets in our suspension. Their dynamics is regulated by the Cahn-Hilliard equation

$$\frac{\partial\phi_i}{\partial t} + \nabla \cdot (\mathbf{u}\phi) = M\nabla^2\mu_i \tag{2.21}$$

where $M$ is the mobility, and $\mu_i = \frac{\delta F}{\delta\phi_i}$ is the chemical potential.

This set of equations for the order parameter can be solved numerically, using

the explicit Euler scheme

$$\phi_i(\mathbf{x}, t + \Delta t) = \phi_i(\mathbf{x}, t) + \Delta t(M\nabla^2\mu_i - \nabla \cdot (\mathbf{u}\phi_i)) \tag{2.22}$$

where we replace the gradient operations with the appropriate lattice equivalent, for instance imposing $\frac{\partial \phi_i}{\partial x} = \frac{\phi_i(x+\Delta x)-\phi_i(x-\Delta x)}{2\Delta x}$. Since there is not another constraint such as the incompressibility condition to satisfy, the order parameter dynamics can be solved without the aid of a second lattice Boltzmann scheme. The latter might alternatively be introduced in the case where we set a different value of viscosity for the two fluids. Indeed, in this scenario we need two different relaxation timescales $\tau_1, \tau_2$ corresponding to the fluid velocity and order parameter respectively [40].

## 2.4 Boundary conditions

In what follows we will define the boundary conditions used for the two fluids (the droplets, and the underlying solvent), which are implemented through the conserved order parameter $\phi_i$ and the lattice Boltzmann scheme. Our simulations are performed in $2D$, where we fix $Lx = 1$ in our box $Lx \times Ly \times Lz$. Along the $\hat{y}$ axis we fix periodic boundary conditions for both fluids, while two walls are defined at $z = 0$ and $z = Lz$.

### 2.4.1 Solvent: non-slip BC

In defining our wall at $z = 0$, we set a full non-slip boundary condition for the solvent fluid in contact with the wall, imposing

$$\mathbf{u}(z = 0) = 0. \tag{2.23}$$

Using the definition of $\mathbf{u}$ described in (2.7) we obtain

$$\sum_i f_i \mathbf{u}_i = 0, \text{ at } z = 0. \tag{2.24}$$

The latter condition can be split in the $\hat{x}$, $\hat{y}$ and $\hat{z}$ component of $f_i$. In particular considering the $\hat{x}$ components we obtain:

$$f_1 + f_7 + f_{10} + f_{11} + f_{14} - f_3 - f_8 - f_9 - f_{12} - f_{13} = 0$$

for the $\hat{y}$ components we have

$$f_2 + f_7 + f_8 + f_{11} + f_{12} - f_4 - f_9 - f_{10} - f_{13} - f_{14} = 0.$$

Finally, considering the $\hat{z}$ components we obtain

$$f_5 + f_7 + f_8 + f_9 + f_{10} - f_6 - f_{11} - f_{12} - f_{13} - f_{14} = 0. \tag{2.25}$$

Since at the boundary $z = 0$ we have five unknown distributions (namely $f_5, f_7, f_8, f_9$ and $f_{10}$), we will need two other equations so that, together with the three conditions above, we will have a set of five equations defining five distributions. These two ulterior conditions can be chosen arbitrarily, for instance based on symmetry arguments like

$$\begin{cases} f_7 - f_8 = f_{10} - f_9 \\ f_5 = f_6. \end{cases} \tag{2.26}$$

We are know able to solve this system obtaining the explicit non-slip boundary conditions for $f_i$s

$$\begin{cases} f_5 = f_6 \\ f_7 = \frac{1}{4}(-f_1 - f_2 + f_3 + f_4 - f_{11} + f_{12} + 3f_{13} + f_{14}) \\ f_8 = \frac{1}{4}(f_1 - f_2 - f_3 + f_4 + f_{11} - f_{12} + f_{13} + 3f_{14}) \\ f_9 = \frac{1}{4}(f_1 + f_2 - f_3 - f_4 + 3f_{11} + f_{12} - f_{13} + f_{14}) \\ f_{10} = \frac{1}{4}(-f_1 + f_2 + f_3 - f_4 + f_{11} + 3f_{12} + f_13 - f_{14}) \end{cases} \tag{2.27}$$

which are implemented after the particles' mesoscopic distribution update at every lattice point.

### 2.4.2 Order parameter: wetting and non-wetting BC

For a scalar order parameter we impose that the concentration flux across the wall is zero (no-flux condition) by imposing

$$\mathbf{J}_{\perp}(z=0) = -M\frac{\partial \mu}{\partial z}\Big|_{z=0} = 0. \tag{2.28}$$

A second condition is necessary if we want to set a wetting angle of our droplets when in contact with the boundary. In particular, this can be done by

$$\frac{\nabla \phi}{|\nabla \phi|} \cdot \hat{z}\Big|_{z=0} = \cos(180^{\circ} - \theta) \tag{2.29}$$

where $\theta$ is the wetting angle [48]. In our case, we use neutral wetting conditions, where $\theta = 90^{\circ}$, therefore we have

$$\frac{\partial \phi}{\partial z}\Big|_{z=0} = \frac{\partial^2 \phi}{\partial z^2}\Big|_{z=0} = 0 \tag{2.30}$$

Non-wetting boundaries, i.e the case where the droplets do not touch the wall, are implemented by substituting equation (2.30) with the condition $\phi_i = 0$. In practice, this is enforced at the mid-point between the first and second lattice node along $z$.

# Chapter 3

# Pressure-driven flow: discontinuous shear thinning and hard-soft transition

In this chapter we investigate the rheological properties of a deformable droplet suspension when subjected to a pressure driven flow. As mentioned in Chapter 1, concentrated suspensions of colloidal particles in a liquid solvent are often found in industry and nature, familiar examples including paint, ink, ice cream or blood.

The flow properties of colloidal suspensions can be distinctively non-trivial: for instance, a suspension of colloidal spheres in water first exhibits shear thinning and then shear thickening, as the external forcing (pressure gradient or shear) is increased [10, 23, 49–51]. In dense suspensions, the fact that shear thickening can be *discontinuous* has recently attracted a lot of attention: this behaviour marks a transition between a lubrication-dominated and a frictional flow regime [23].

However, often in such colloidal fluids, the dispersed particles are not hard, but soft, and deformable [52]. Examples are the fat droplets found in milk, or eukaryotic cells: all these can deform under flow, or when subjected to a mechanical stress. While hard sphere fluids have been studied extensively, and provide the basis for our understanding of the glass transition [53–55] and of soft glassy rheology [56], less is known about the flow response of suspensions of deformable particles [52, 57–61]. Nonetheless, there is a number of examples suggesting that the physics of soft suspensions is both highly interesting and

important in applications. For example, experiments and simulations have recently demonstrated that glass transitions and jamming can be observed in dense monolayers of living cells[62–65]. For instance, a self-propelled Voronoi model for a confluent tissue exhibits a jamming transition from a solid-like state towards a fluid-like one. Moreover, as shown in [64], this transition is controlled by three parameters: the single-cell motile speed, the persistence time of single cell tracks and a target shape index that characterises the competition between cell-cell adhesion and cortical tension.

Emulsions – which are dispersion of liquid droplets in a continuous medium – are also used in medicine and food, and their flow properties play a pivotal role in applications. Particles' ability to deform is important in determining the rheology of a material: for example, emulsions and foams do not normally display shear thickening, unlike hard sphere colloidal fluids.

In the following sections, after introducing the model used to simulate our droplet suspension, we present the dynamics and flow properties of our system, obtained through the analysis of the simulation results.

## 3.1 Model for a deformable droplet suspension

### 3.1.1 Phase field approach

We use 2D lattice Boltzmann simulations to investigate the dynamics of a suspension of soft, and non-coalescing, droplets (Figs. 3.1a,b) under pressure-driven flow within a channel. Two key parameters determine the flow response of our system: (i) the concentration, or area fraction $\Phi$, defined as the ratio between the area of all droplets and the total area of the simulation domain, and (ii) the applied pressure difference $\Delta p$ driving the flow.

To study the hydrodynamics of our soft droplet fluid, we follow the evolution of the phase-field variables describing the density of each of the droplets, $\phi_i$, $i = 1, \ldots, N$, where $N$ is the total number of droplets, as well as the velocity field of the underlying solvent $\mathbf{v}$. The equilibrium behaviour is governed by the

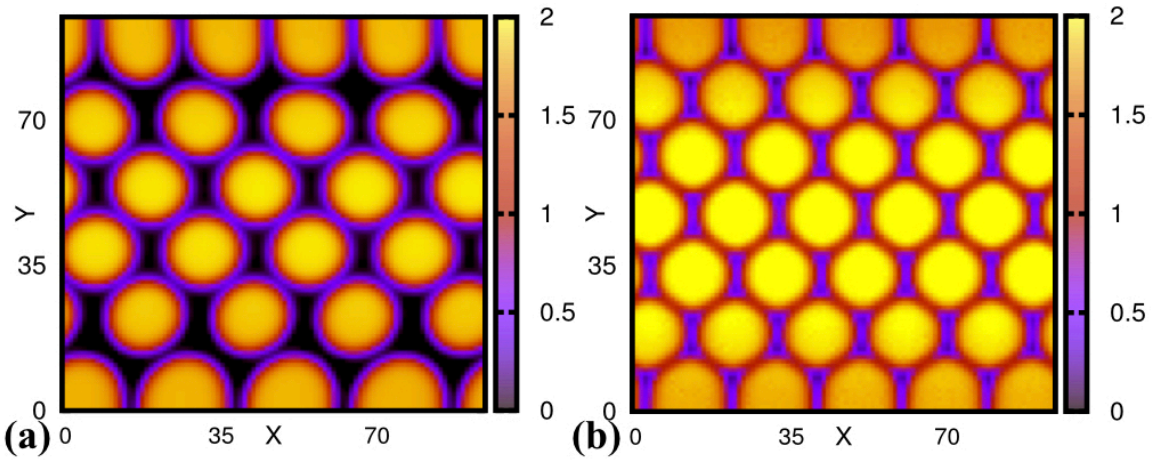


**Figure 3.1** *Geometry and set-up. (a,b) Snapshots of a droplet suspension of area fraction* $\Phi = 54.5\%$ *(a), and* $\Phi = 76.3\%$ *(b). The color code refers to the value of* $\sum_i \phi_i$*: this is* $\sim 2$ *for droplets, and* $\sim 0$ *for the background solvent – values are slightly* $< 2$ *within boundary droplets due to spreading.*

.

following free energy density,

$$f = \frac{\alpha}{4}\sum_{i}^{N}\phi_i^2(\phi_i - \phi_0)^2 + \frac{K}{2}\sum_{i}^{N}(\nabla\phi_i)^2 + \epsilon\sum_{i,j,i<j}\phi_i\phi_j. \tag{3.1}$$

In Eq. 3.1, the first term represents the double well potential which ensure droplets stability. Indeed, it allows the presence of two minima for $f$ for $\phi_i = \phi_0$ and $\phi_i = 0$, which represents the inside and outside area of the i-th droplet, respectively. The droplet deformability properties are determined by their surface tension $\gamma = \sqrt{(8K\alpha)/9}$, and can therefore be tuned by changing the value of $K$ in the second term of eq.(3.1). The parameters $K$ and $\alpha$ also determine the interfacial thickness of the droplets as $\xi = \sqrt{2K/\alpha}$. The third, final term describes a soft repulsion pushing droplets apart when they overlap, therefore preventing coalescence. The strength of this repulsion is regulated by the value of the positive constant $\epsilon$. Such parameter is used to avoid overlaps, and it may be thought of as an analog of the Weeks-Chandler-Anderson (or purely Lennard-Jones) which is used for hard colloidal particles. We note that it is short-ranged and we saw no signal of any ordering caused by this term. We therefore don't expect any quantitative change in the micro or macrorheological response with the $\epsilon$ parameter.

The dynamics of the compositional order parameters $\{\phi_i\}_{i=1,\ldots,N}$ evolves accord-

ing to a set of Cahn-Hilliard-like equations,

$$\frac{\partial \phi_i}{\partial t} + \nabla \cdot (\mathbf{v}\phi_i) = M\nabla^2 \mu_i \tag{3.2}$$

where $M$ is the mobility and $\mu_i = \partial f/\partial \phi_i - \partial_\alpha f/\partial(\partial_\alpha \phi_i)$ is the chemical potential of the $i$-th droplet. Eq. 3.2 conserves the area of each of the droplets (i.e., the integral of each $\phi_i$ over the whole simulation domain).

The droplets dynamics are coupled to that of the underlying solvent which evolves according to the incompressible Navier-Stokes equation:

$$\rho\Big(\frac{\partial}{\partial t} + \mathbf{v}\cdot\nabla\Big)\mathbf{v} = -\nabla p - \sum_i \phi_i \nabla \mu_i + \eta_0 \nabla^2 \mathbf{v}, \tag{3.3}$$

where $\rho$ indicates the fluid density, $p$ denotes its pressure and $\eta_0$ the solvent viscosity. The term $\sum_i \phi_i \nabla \mu_i$ represents the internal forces due to the presence of non-trivial compositional order parameters, and as such it can also be expressed as a divergence of a stress tensor [66].

Figure 3.1 shows two typical snapshots of our system, under weak pressure-driven flow and for two different values of $\Phi$. These snapshots clarify that, when $\Phi$ is low, we obtain a suspension of well-separated droplets: while these droplets interact hydrodynamically and may in principle deform, there is a substantial region between them occupied by the background solvent (Fig. 3.1a). At higher concentrations, droplets touch each other even in the absence of flow, to form a percolating foam (Fig. 3.1b). The snapshots also highlight that the neutral wetting boundary conditions we use lead to spreading on droplets close to the wall, with a contact angle of 90°. We note that droplets need to approach the wall close enough in order to stick: this only happens for $\Phi \simeq 35\%$.

In general, in order to study the dynamics of multiphase flows a different way of implementing Lattice Boltzmann scheme has been proposed [67]. In particular, the inclusion of a mid-range repulsive potential within the Shan-chen formulation [68] of non-ideal lattice fluids provides a very rich physical picture, allowing the possibility of realising multiphase flows with long-lived metastable states characterised by multidroplet configurations. This model allows the independent tuning of droplets' size and of the density ratio between the liquid and gas phases, therefore permitting efficient handling of complex applications such as micro-emulsions, multiphase sprays and globular protein crystallization.

In what follows, we report results from hybrid lattice Boltzmann (LB) simulations [40, 44] where Eq. 3.3 is solved by an LB algorithm, and Eqs. 3.2 are solved via a finite difference. We consider flow in a channel with no-slip boundary conditions at the top and bottom walls. The flow is driven by a fixed, externally imposed pressure difference, which leads to Poiseuille flow in an isotropic fluid, and neutral wetting boundary conditions for each of the droplets [69] (see Chapter 2). The parameters used in our simulations are the following: we fix the droplet radius at $r = 8$ and the mobility to $M = 0.1$, while the free energy parameters are $\alpha = 0.07$, $K = 0.14$ and $\epsilon = 0.05$. The viscosity of the underlying fluid is $\eta_0 = \frac{5}{3}$ (for simplicity this is also the viscosity of the fluid inside the droplets), and the value of the applied pressure difference ranges within $[10^{-6} - 10^{-4}]$. The value of $\eta_0$ derives from our implementation of the Lattice Boltzmann scheme using the predictor corrector method. Whilst using the Euler method it is typical to set values of $\eta_0$ smaller than 1, with the predictor corrector method values larger than 1 do not cause any inconsistencies in the Lattice Boltzmann. While the trends we discuss are generic, the simulations we report can be mapped to a system with $\sim 100\mu$m-size droplets whose surface tension is $\gamma \sim$mN/m, embedded in a background Newtonian fluid with viscosity $\eta_0 = 10^{-2}$ Pa s (similar values of viscosity are measured for apple juice or soybean oil). Our model differs from that used in [67] to study the glassy dynamics of foams and sprays, which in general allows for droplet coalescence.

## 3.2 Hard-soft transition

As anticipated in the previous section, we perform simulations where our droplet suspension is subjected to a pressure driven flow, regulated by the external application of an homogeneous body-force on the underlying solvent.

The flow profile which we observe strongly depends on the suspension area fraction $\Phi$. Indeed, in Fig. 3.2 we plot the $\hat{x}-$component of the average velocity of the fluid as a function of $y$. As we can notice, for low density the profile is approximately parabolic, while the flow becomes plug-like at higher values of the area fraction.

Pressure-driven flow in these suspensions is therefore strongly non-Newtonian, at least for foam-like structures with large $\Phi$. We can nevertheless define, as in experiments, an apparent viscosity, $\eta$, by analysing the throughput flow

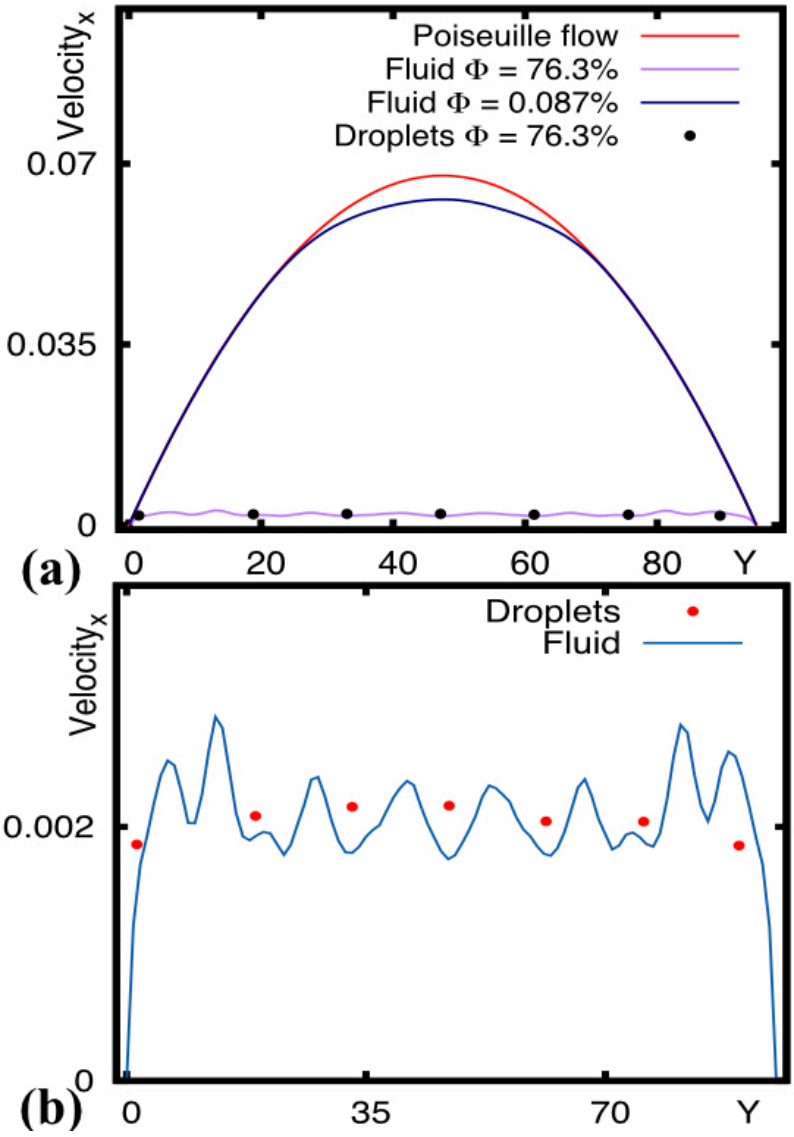


**Figure 3.2** ***(a)*** *Fluid velocity profile (as a function of y) for two different values of area fraction Φ. For lower density (blue line) we observe a parabolic profile, compatible with the behaviour expected of an isotropic fluid with the same viscosity (red line), for higher density (purple line) we observe a plug-like flow. In the latter case the velocity of the droplets (solid circles) is similar to the fluid velocity (purple line).* ***(b)*** *Zoom of plot in* ***(a)*** *to better observe the plug-like shape of the flow in the case of high area fraction Φ.*

$Q = \int dy v_x(y)$. A useful quantity is the ratio between $Q$ and the throughput flow of a Newtonian fluid with viscosity $\eta_0$, that of the underlying solvent (when no droplets are present). The inverse of this ratio gives a measure of the relative, effective viscosity $\eta_{eff} = \frac{\eta}{\eta_0}$. A plot of $\eta/\eta_0$ as a function of $\Phi$ for a given value of $\Delta p$ (Fig.3.3) shows that this viscosity increases sharply and non-linearly with $\Phi$, which is suggestive of jamming, as the droplet concentration increases [70, 71].

The fits are performed using the functional form

$$f(\Phi) = a \exp^{\frac{b}{(c-\Phi)}} . \tag{3.4}$$

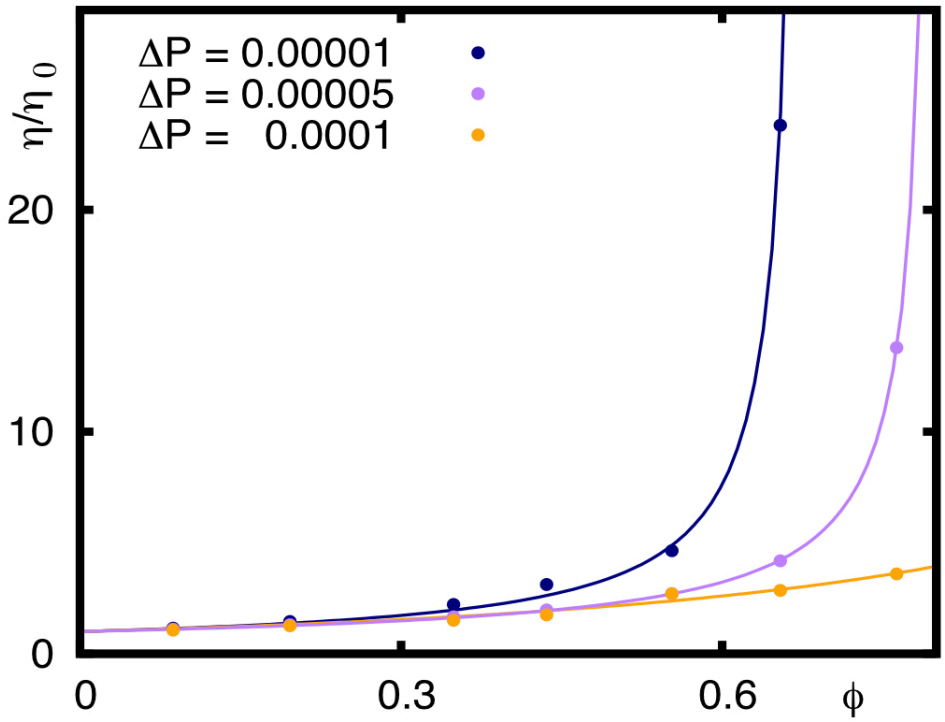


**Figure 3.3** *Plot of the effective viscosity versus* $\Phi$ *for three different fixed values of applied pressure difference* $\Delta p$*; fits are a guide to the eye.*

inspired by previous work on hard colloidal suspensions [72], where a, b, c are fitting constants. These fits are only meant as guide for the eye, as our data do not allow us to discriminate between two scenarios: one in which there is a yield stress as in standard theories of jamming, and another one where there is a very large but finite linear viscosity.

### 3.2.1 Discontinuous shear thinning

As expected, in our previous section we find that, for a fixed $\Delta p$, $\eta_{eff}$ increases sharply with $\Phi$, as droplets approach jamming.

In contrast, the behaviour of our suspension's effective viscosity with the pressure difference $\Delta p$ is more surprising, and constitutes a key result of our simulations: if the concentration is large enough, we find $\eta_{eff}$ shows *discontinuous* shear thinning rheology.

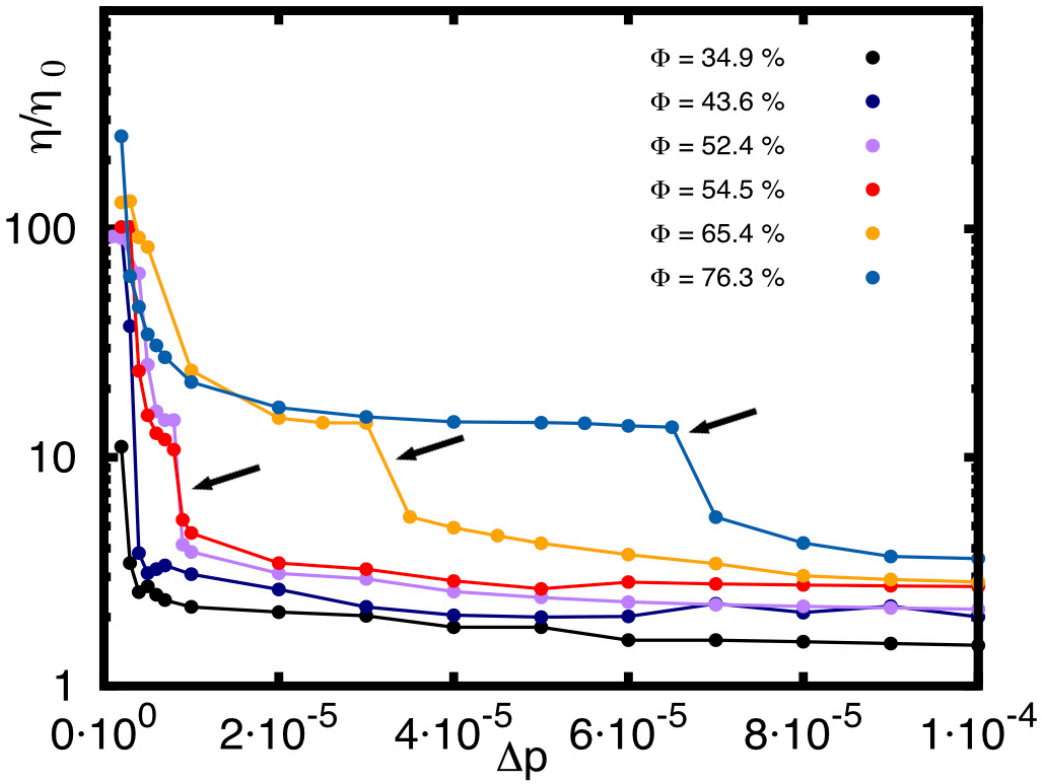


**Figure 3.4** *Plot of the relative viscosity of the droplet suspension as a function of $\Delta p$, for five different values of $\Phi$. As $\Delta p$ increases, there is always shear thinning – i.e. the relative viscosity progressively decreases with forcing. For large enough $\Phi$ this shear thinning is discontinuous, and arrows denote the discontinuities. The small kinks in the bottom two curves at low $\Delta P$ are not significant, and due to inaccuracies in sampling $\eta$ by time averaging which are larger in that regime.*

Indeed, in Figure 3.4 we focus on the variation of $\eta/\eta_0$ with pressure difference $\Delta P$, at fixed $\Phi$. For all concentrations, we find strong shear thinning. This behaviour resembles that seen in experiments probing the rheology of emulsions and foams. Remarkably, though, for area fraction $\Phi \gtrsim 50\%$ we find this shear thinning behaviour to be "discontinuous": in other words, there is a jump in the viscosity for a critical value of the forcing (arrows in Fig. 3.4), signalling a possible flow-induced nonequilibrium transition. This behaviour contrasts with the smooth (or continuous) shear thinning found in hard colloidal dispersions at intermediate shear rates [10], or in previous simulations of droplet emulsions under shear [57, 59, 60].

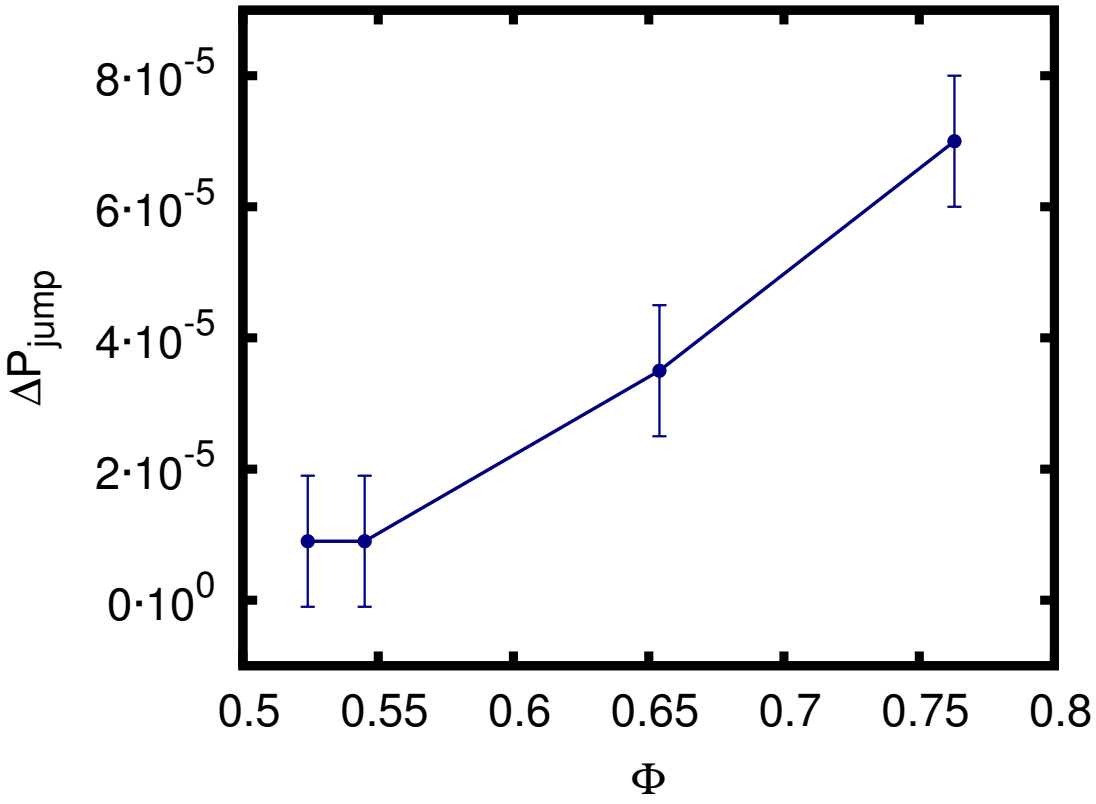


**Figure 3.5** *Plot of the value of the applied pressure difference $\Delta P$ corresponding to the jump in the system viscosity as a function of the suspension area fraction $\Phi$. The error bars refer to the interval between the values of $\Delta P$ used in our simulation. Indeed we only fixed discretised value of $\Delta P$ that are multiple of $10^{-5}$.*

In particular, discontinuous shear thinning is observed for $\Phi = 52.4\%, 54.5\%, 65.4\%$ and $76.3\%$, with the viscosity jump occurring for larger pressure differences as $\Phi$ increases showing an approximately linear trend (see Fig. 3.5).

### 3.2.2 Droplet deformation: hard-soft transition

As shown in Figure 3.4, for sufficiently large values of $\Phi$, we can therefore define two viscosity branches, lying either side of the discontinuity. To identify the difference between the left and right viscosity branches, we first characterise how the flow affects droplet shape (Figs. 3.6a,b).

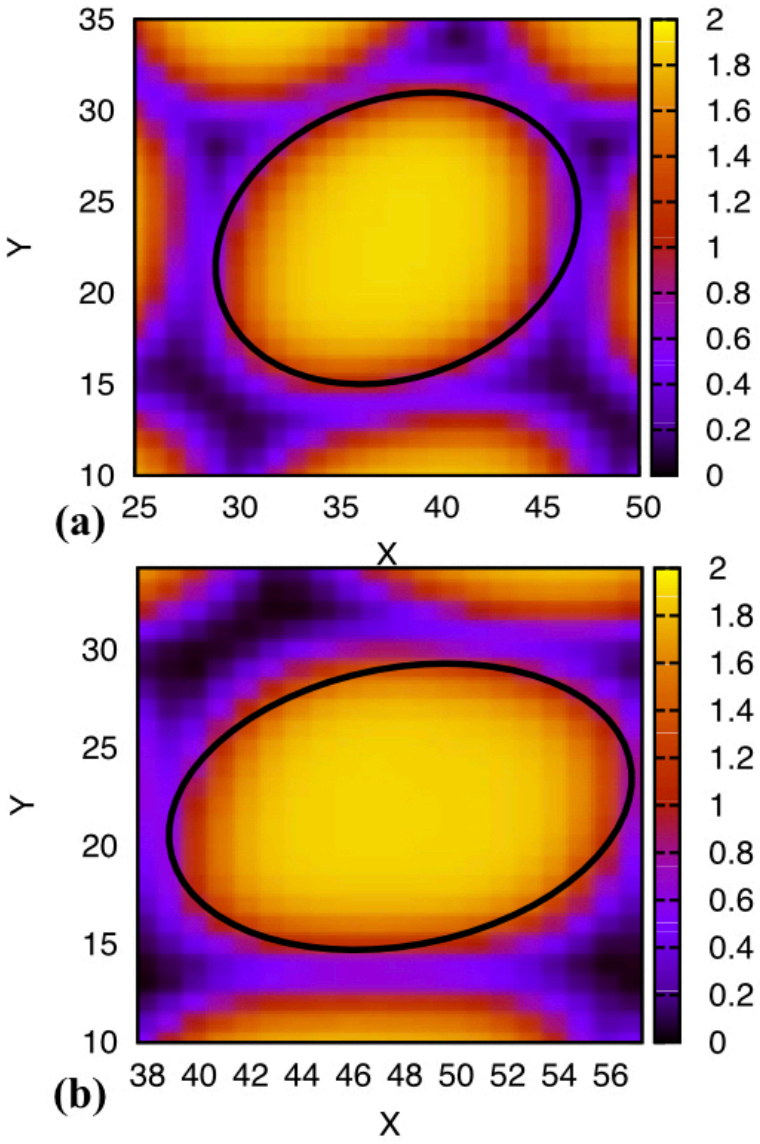


**Figure 3.6** *(a) Zoom of a simulation snapshot showing the shape of a selected droplet under pressure difference $\Delta P = 5 \cdot 10^{-5}$. As we can see, the droplet presents an almost circular shape. (b) Zoom of a simulation snapshot showing the shape of a selected droplet under pressure difference $\Delta P = 9 \cdot 10^{-5}$. As we can see, in this case the droplets presents a more elliptical shape. The black curves are a guide for the eyes.*

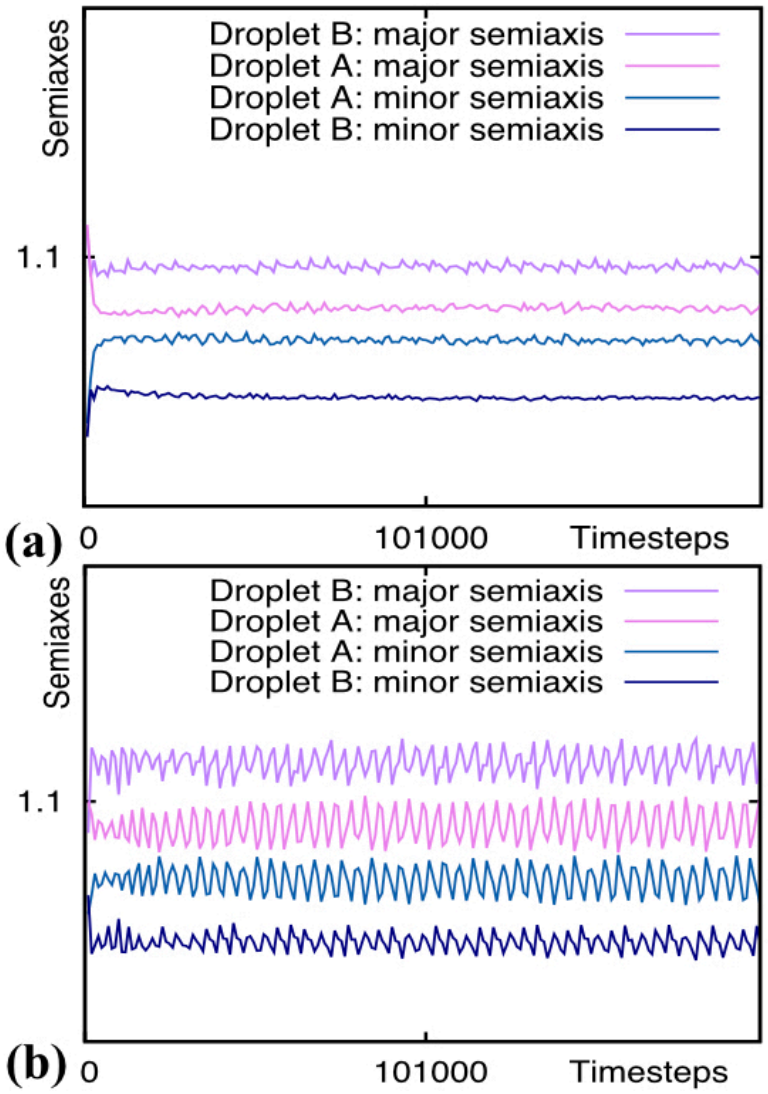


**Figure 3.7** *(a) Plot of the two semi-axis of the ellipse defined by the inertial tensor of two selected droplets taken from a suspension with* $\Phi = 76.3\%$ *and* $\Delta p = 10^{-5}$*. Droplet A belongs to the central array of droplets and is far from the boundary. Droplet B belongs to the array just above the wetting layers of droplets. (b) Same as (a), but for a pressure difference of* $\Delta p = 7 \times 10^{-5}$*, close to the point at which the viscosity drops sharply.*

In order to give a quantitative measure of our droplet ability to deform, we construct the inertia tensor of each of the droplets [73]. The square root of the larger and smaller eigenvalues of this tensor are proportional to the major and minor semi-axes of an ellipse which best approximates the droplet (the proportionality constant is $\frac{2}{M}$, with $M$ the "mass" of the droplet, corresponding to its area in our case). Whilst for large $\Phi$ the droplets may not be well approximated by ellipses, the major and minor semi-axis sizes $\lambda_1$ and $\lambda_2$ still give a measurement of droplet anisotropy, and allow us to estimate variation in droplet shape over

time. An example of this geometrical approximation is shown in Figure 3.6, where we compare the shape of a single droplet when subjected to two different values of the pressure difference. In particular, in Fig. 3.6**(a)**, corresponding to a low value of $\Delta P$, the droplet shows an almost circular shape, while a clearly elliptical one can be seen in Fig. 3.6**(b)**, where the higher value of $\Delta P$ induces a larger deformation. More sophisticated measures would involve higher-rank deformation tensors as in [74], but they are not necessary for our purposes here.

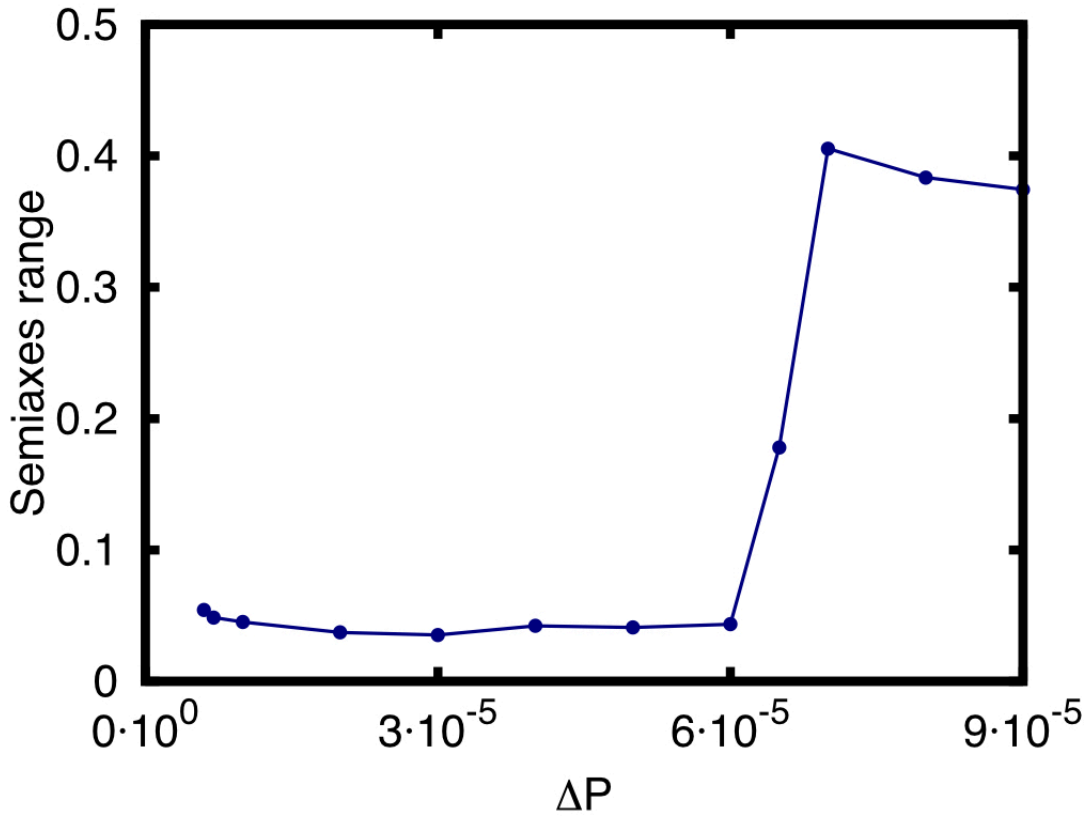


**Figure 3.8** *Plot of the maximal temporal spread of the ratio $\frac{\lambda_1}{\lambda_2}$, as a function of $\Delta P$. Here, $\lambda_1$ and $\lambda_2$ are the larger and smaller eigenvalue of the inertial tensor, respectively (this ratio may also be thought of the ratio between the major and minor semi-axis of an ellipse which fits the droplet shape). This plot is an average over droplets in the array next to the wetting layer, and it gives a measure of the variation of droplet shape over time it can be seen that such variation increases sharply where we observe discontinuous shear thinning.*

Comparing the time evolution of the droplet major and minor semi-axis for the two viscosity branches, the results point to a clear difference: on the left

(high viscosity) branch, the droplet shape is constant over time (Fig. 3.7**(a)**); on the right (low viscosity) branch, there are more significant deformations, and, importantly, these display marked variations over time (Fig. 3.7**(b)**). We therefore name the left branch 'hard', and the right branch 'soft'.

More systematically, we have computed how the spread in the variation of $\frac{\lambda_1}{\lambda_2}$ over time depends on $\Delta P$. Data (averaged over the array of droplets immediately above the wetting layer) are shown in Figure 5.8: they show a clear jump in the spread at the value of $\Delta P$ for which we observe the viscosity jump in Figure 3.4.

We conclude that the discontinuity in the apparent viscosity shown in Fig.3.4 can be interpreted as a transition (or sharp crossover) between a hard phase, where the droplets are effectively rigid, and a soft one, where they are highly deformable, even though the droplet surface tension $K$ set by our model is equal in both cases. Evidence of this transition can be found in the suspension's different behaviour shown in Suppl. Movie 1 and 2 [1], where the applied pressure difference belongs to the hard and soft branch, respectively. Indeed, in Movie 1 the suspension struggles to flow, and the droplets shape barely changes in time. On the other hand, in Movie 2 the same suspension, this time subjected to a higher pressure difference, flows much more easily and each droplets presents a fast periodic shape deformation.

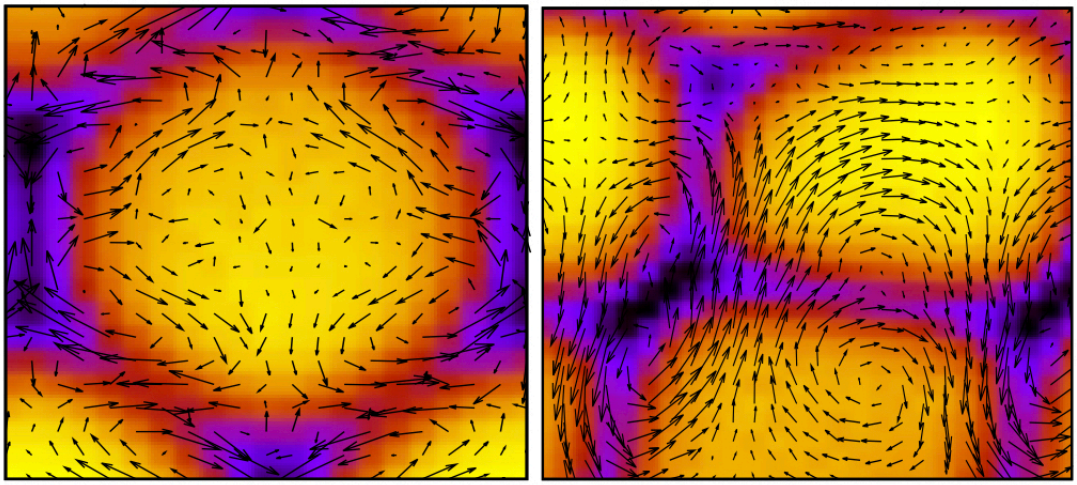


**Figure 3.9** *(a) Fluid velocity field and droplet pattern for a suspension with area fraction* $\Phi = 76.3\%$ *and pressure difference* $\Delta p = 3 \times 10^{-6}$. ***(b)*** *Fluid velocity field and droplet pattern for a suspension with area fraction* $\Phi = 76.3\%$ *and pressure difference* $\Delta p = 9 \times 10^{-5}$.

[1] The supplementary movies can be found on https://datasync.ed.ac.uk/index.php/s/FUhZkTvl4Nqs3yI accessible using password: foglino

The hard and soft branches also differ in the flow patterns observed in the steady state. When the average flow along $x$ is subtracted out, the residual flow is mainly limited to gaps between droplets in the hard branch (Fig. 3.9**(a)**), whereas it penetrates more deeply within the droplet interior in the soft branch (Fig. 3.9**(b)**). The larger internal flow in the soft phase arises mainly due to interaction between neighbouring lanes of droplets, and is therefore maximal close to the boundary, where the wetting layer of droplets leads to the largest effective friction with the rest of the suspension.

### 3.2.3 Droplet velocity oscillations

Closer inspection of the simulation results reveal a further intriguing phenomenon.

Consider for example a suspension with $\Phi = 54.5\%$, for $\Delta p = 10^{-5}$ – i.e., just after the drop in viscosity in Fig. 3.4 (the corresponding dynamics is shown in Suppl. Movie 3).

As the flow sets in, the droplets that are initially close to the boundary (droplets a and e in Fig. 3.10**(a)**) stick to the wall and slow down dramatically, while those close to the centre (droplets b, c, and d) undergo a 'stick-slip' motion whereby they periodically accelerate and decelerate. The oscillations are visually clear when tracking droplet velocity over time (Fig. 3.10**(a)**); Fourier transforming these data shows they are also very regular (Fig. 3.10**(b)**).

Oscillations also occur for other values of $\Phi$ and $\Delta p$, and for larger system size: notably, the region in phase space where they happen is, in all cases, close to the discontinuity in the viscosity curve (see the table below 3.1). This is reasonable, as we expect that near the discontinuous shear thinning transition there should be hysteresis, similarly to what happens next to a thermodynamic first-order transition. Consequently the suspension can hop between the hard and soft viscosity branches, giving rise to oscillations. An analysis of Suppl. Movie 3 additionally suggests that oscillations correlate well with deformations arising from contact interactions between the wetting layer and the nearest lane of droplets. Thus, each droplet in the latter array slows down when it first touches one of the droplets in the wetting layer, while it squeezes faster through the gap once it is deformed. This latter microscopic mechanism is consistent with the former explanation that oscillations require proximity to the hard-to-soft transition, because shape deformations – which play a key role in the microscopic

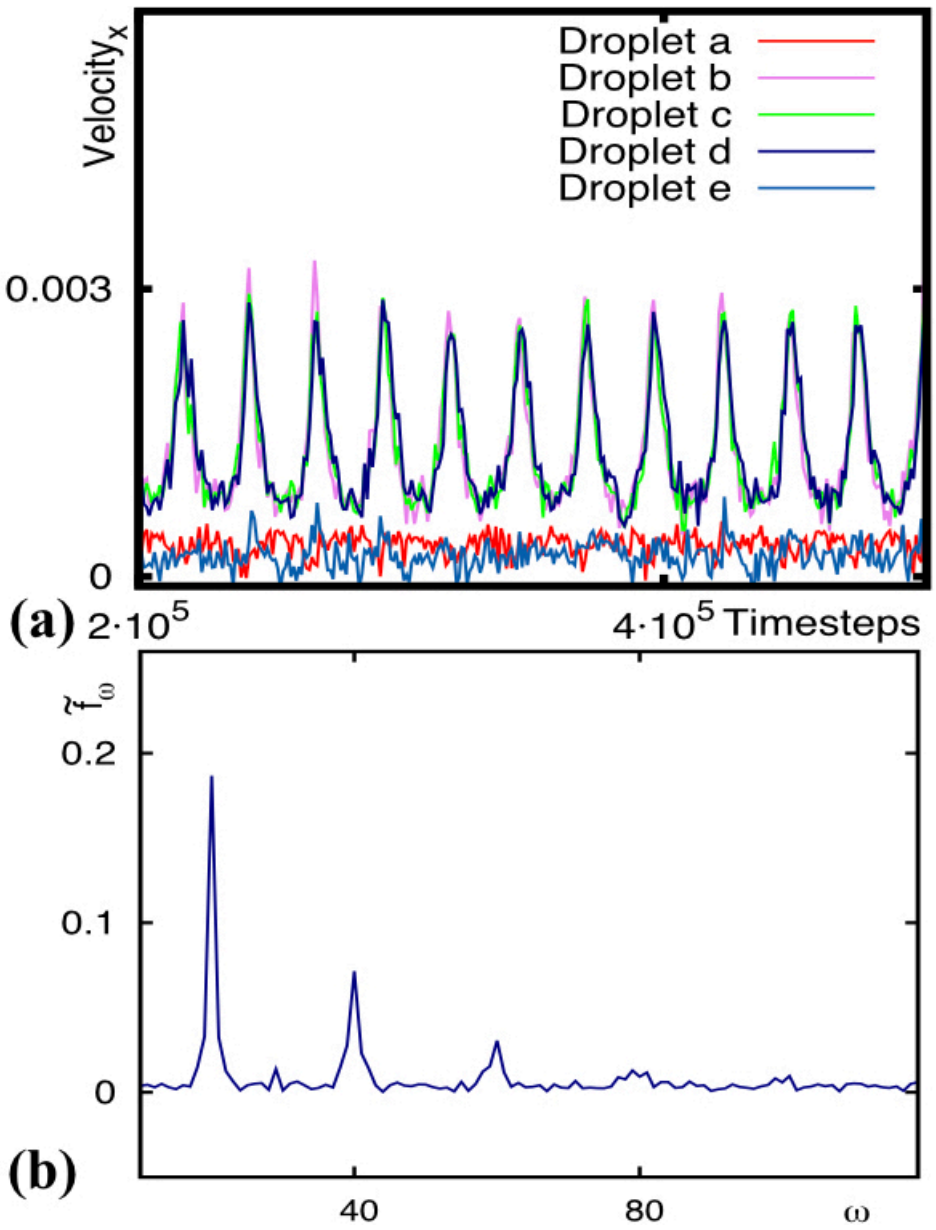


**Figure 3.10** *(a) Plots of the droplet velocities as a function of time. Droplets b, c and d belong to the array at the centre of the channel, while droplets a and e belong to the wetting layer. Oscillations in the x-component of the droplet velocities are apparent for all droplets except those in the wetting layer, where motion is slow. (b) Fourier transform of the droplet velocities time series: clear peaks are visible, corresponding to the oscillation frequency and its multiples.*

argument – define the soft phase.

The droplet velocity oscillations we observe are qualitatively similar to those found in driven colloidal suspensions close to the glass transition [75], as those,

| Area fraction $\Phi$ | Bodyforce $F(\times 10^{-5})$ |
|---|---|
| 54.5% | $1, 2, 3, 4, 5, 6, 7, 8, 9, 10$ |
| 65.4% | $3, 4, 5, 6, 7, 8, 9, 10$ |
| 76.3% | $7, 8, 9, 10$ |

**Table 3.1** *Parameter values (simulation units) at which oscillations in the droplet velocities are found.*

too, correlate well with the gap between flowing and boundary colloids. It would be of interest to ask whether even for the colloidal case oscillations arise close to the discontinuous (shear thickening) transition.

### 3.2.4 System size dependence

The results reported in the previous sections pertain to a system size of $L_y = 96$ in the velocity gradient ($y$) direction.

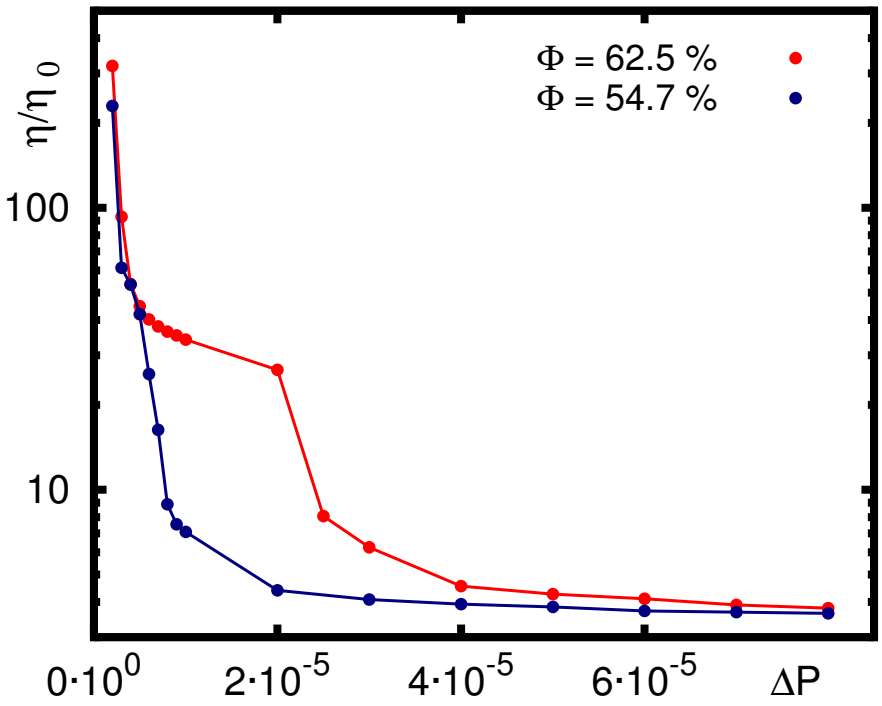


**Figure 3.11** *Plot of the apparent viscosity as a function of $\Delta P$ for two fixed values of area fraction $\Phi = 62.5\%$ and $\Phi = 54.7\%$ for channel of width $L_y = 134$. As in the previous case of a thinner channel ($L_y = 96$, see main text), we observe discontinuous shear thinning in the viscosity curves.*

To address the dependence of discontinuous shear thinning on system size, we ran additional simulations of our droplet suspension confined in a channel of larger width. In particular we simulated a channel with $L_y = 134$ and analysed the flow properties of our suspension for two fixed values of the area fraction, $\Phi = 54.7\%$ and $\Phi = 62.5\%$ (these cases result in two more droplet arrays than considered in the previous case). As we can see in Figure 3.11, also in this case we can detect the discontinuous jump in the suspension relative viscosity as a function of the applied pressure difference.

Additionally, if we focus on the values of applied pressure difference $\Delta P$ close to the viscosity jump, we observe oscillations in the droplets velocities over time as in the previous case of a thinner channel (see Fig. 3.12). The trends we report are therefore robust with changes in the system size, at least within the range we have analysed.

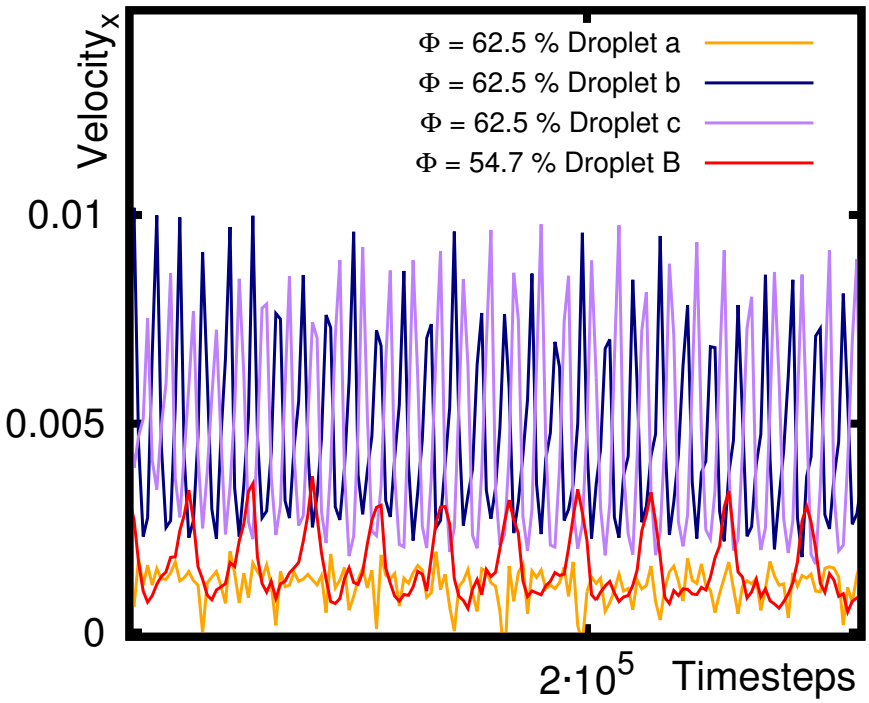


**Figure 3.12** *Plot of the droplets velocities oscillations over time evolution for a fixed value of applied pressure difference $\Delta P$ close to the discontinuity in the system viscosity. Droplets $b, c$ (for the case of $\Phi = 62.5\%$) and $B$ (for the case of $\Phi = 54.7\%$) belong to the lines in the centre of the suspension, while droplet $a$ is in contact with the wetting layer of droplets, which considerably reduce its velocity.*

### 3.2.5 Non-wetting Boundary Conditions

All the results presented so far refer to a neutral wetting boundary condition for the compositional order parameters, $\phi_i$, at the wall, implemented as explained in Chapter 2. If, instead, non-wetting boundary conditions are used, we observe a much lower apparent viscosity with respect to the case of neutral wetting, and we find essentially no discontinuous shear thinning (Fig. 3.13).

Additionally, there are no velocity oscillations in the parameter range we considered. Suppl. Movie 4 shows an example of the dynamics for a suspension with non-wetting boundary conditions. In line with the results in Figure 3.13, it can also be seen that the droplets flow without appreciable deformation. This confirms that friction with the wetting layers of droplets is needed both for the discontinuous shear thinning behaviour, and the presence of velocity oscillations.

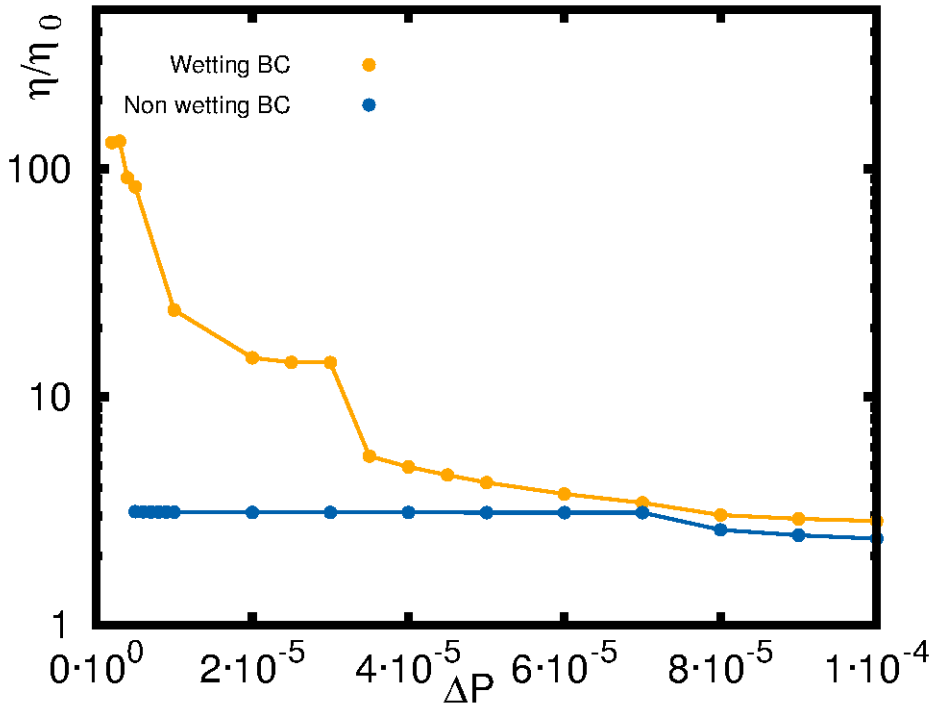


**Figure 3.13** *Plot of the apparent viscosity as a function of the pressure difference $\Delta P$ for neutral wetting (top curve) and non-wetting (bottom curve) boundary conditions, for a suspension with $\Phi = 65.4\%$.*

## 3.3 Polydispersity

All the results discussed in the previous section have been obtained considering a monodisperse suspension, i.e. all the droplets had the same size. However, polydispersity is known to strongly affect the behaviour of colloidal systems, for instance in so far as the glass transition is concerned [55].

To explore the effect of polydispersity on discontinuous shear thinning in a selected case, we performed similar simulations and analysis on a bidisperse suspension. In particular, we considered the case where the droplet radius of one component is twice as large as that of the other one, as shown in the simulation snapshot in Fig. 3.14.

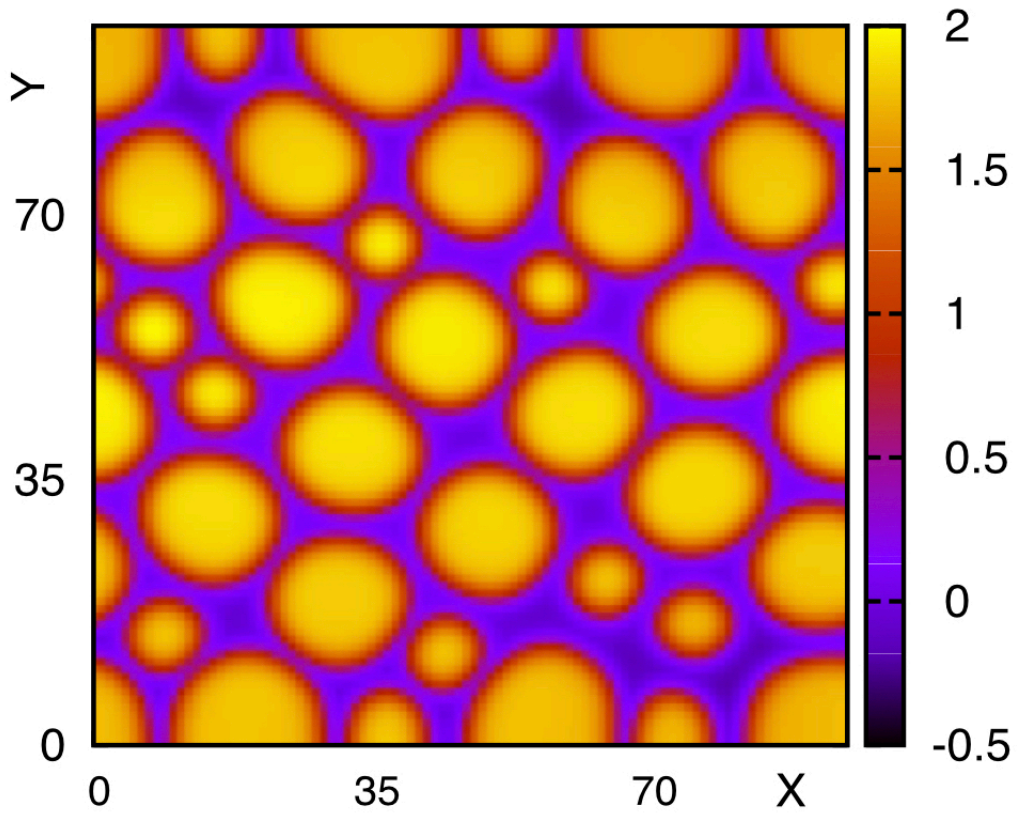


**Figure 3.14** *Simulation snapshot of a polydisperse suspension of area fraction* $\Phi = 54.5\%$*. The small droplets are characterised by a radius which is half the size of that of the large droplets.*

Following the same pattern as for the monodisperse case, we analyse the suspension effective viscosity as a function of the applied pressure difference $\Delta P$ for different value of fixed area fraction (Figure 3.15).

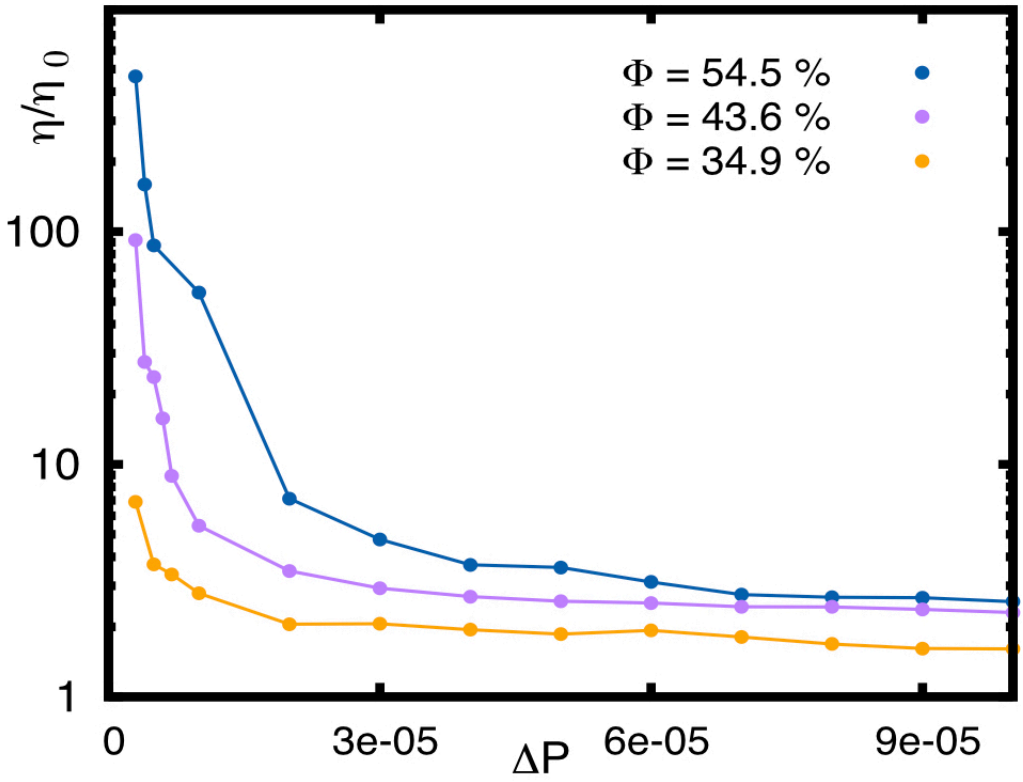


**Figure 3.15** *Plot of the suspension effective viscosity as a function of $\Delta p$ for three different fixed values of area fraction $\Phi$, showing clear shear thinning behaviour. The curve referring to $\Phi = 54.5\%$ shows a discontinuous behaviour analogous to what we found in the monodisperse case. The other two curves present instead only normal shear thinning.*

While the suspension still clearly shear thins, with a comparable overall drop in viscosity with respect to the monodisperse case, here no discontinuity can be found, apart from the case of $\Phi = 54.5\%$ (blue curve in Fig. 3.15). Our simulation videos show less clear droplet deformation; indeed, being spatially distributed in a less regular way with respect to the monodisperse case, the droplets are on average less in contact with each other, therefore less susceptible to deformations.

Considering the case of a suspension of area fraction $\Phi = 54.5\%$, where we observe a discontinuous transition in the viscosity, we find again oscillations in the droplet velocity, analogously to our previous results. However, these oscillations are much more irregular with respect to the monodisperse case. Figure 3.16 shows the $x-$component of five droplets velocity over time evolutions, presenting a much less defined oscillatory pattern in time.

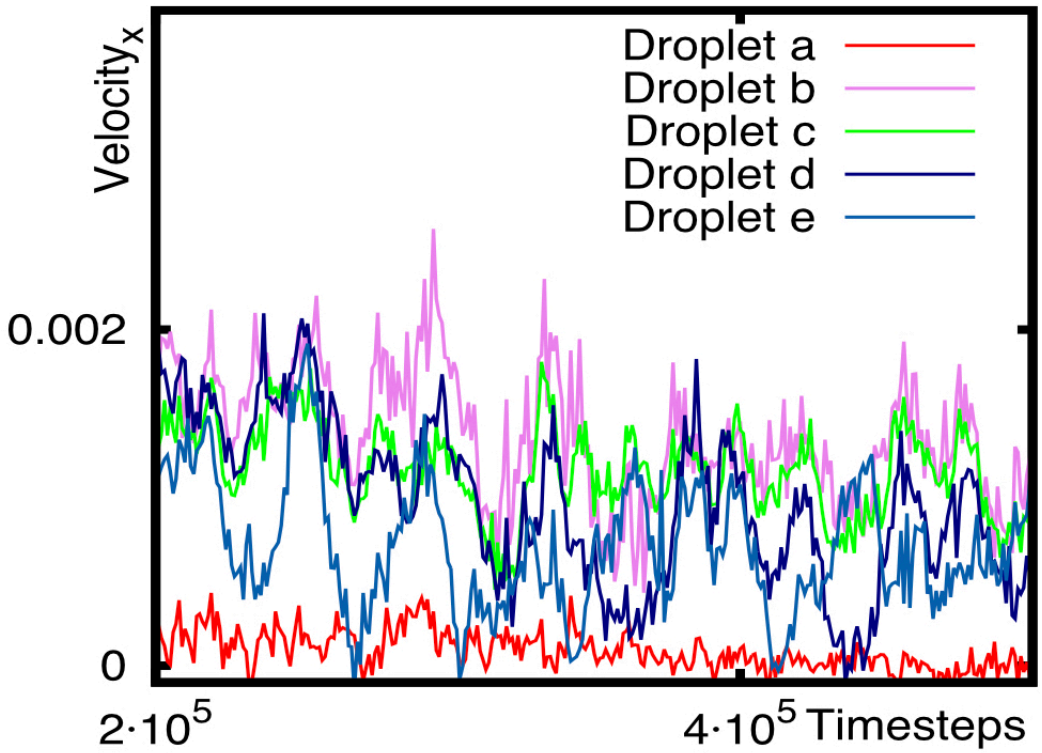


**Figure 3.16** *$x-$component of the velocity of five different droplets within a polydisperse suspension of area fraction $\Phi = 54.5\%$. Droplets b,c,d and e belong to the droplet array in the centre of the channel, while droplet a belongs to the bottom wetting layer. Similarly to Fig. 3.10 there are oscillations in the velocities of the droplets far from the boundary, however these are less regular and clear than in the monodisperse case.*

These findings suggest that a sufficiently strong polydispersity smooths out the nonequilibrium transition between the hard and soft phases, turning it into a crossover. The reason is that larger droplets start to deform at a weaker forcing than smaller ones, hence the overall hard-to-soft transition occurs more gradually with respect to the monodisperse case.

Experimentally, the polydispersity $\sigma$ is usually defined to be the standard deviation of this distribution divided by the mean value. The typical values if polydispersity experimentally achievable range within $[0.02 : 0.5]$ [55]. It has been shown how the degree of polydispersity affect crystallisation and glass formation in hard sphere colloids, as well as the suspension packing volume fraction [76]. In our simulations, given that the radius of the small droplets is half of the bigger droplets' one, the level of polydispersity is quite high (around $\sigma \sim 0.4$). We note that, as discussed above, with this level of polydispersity our results suggest that the transition from the hard to the soft phase becomes smooth, and no

discontinuity in the viscosity can be detected. Although, we would imagine that for lower values of polyduspersity (say $\sigma \lesssim 0.2$), the distribution of droplets' sizes could be less spread, therefore allowing the presence of the discontinuous transition.

## 3.4 Concluding remarks

In summary, we have shown that the rheology of a suspension of deformable non-coalescing droplets, under a pressure-driven flow, entails discontinuous shear thinning behaviour. This discontinuity may be viewed as a nonequilibrium transition between a hard droplet regime, which flows slowly, and a soft droplet phase, which flows much more readily. In the former phase, droplet shape is constant over time; in the latter, it varies significantly as they flow. To observe discontinuous shear thinning, we need large enough concentration, $\Phi$. At a given value of $\Phi$, our physical interpretation of the hard-to-soft transition suggests that a key dimensionless parameter is the capillary number [57–60] denoting the ratio between external forcing and interfacial tension.

Close to the transition, we find sustained oscillations in both the fluid and the droplets velocities, which are reminiscent of those reported previously for hard colloidal systems close to the glass transition [75]. It is tempting to speculate that in both cases oscillations arise due to proximity to a discontinuous transition.

In the future, it would be interesting to experimentally recreate discontinuous shear thinning in the laboratory, by studying the rheology of suspensions of non-coalescing droplets [77]. Theoretically, our findings prompt new questions, which we address in the following Chapter. Indeed, it is interesting to characterise the dependence of the hard-to-soft transition on surface tension. It would also be informative to study the microrheology [78] of our droplet suspensions and see what signatures discontinuous shear thinning leaves there.

# Chapter 4

# The role of droplet surface tension

## 4.1 Deformable suspensions

In this Chapter we investigate the role of droplet deformability in the overall rheological and flow properties of a suspension. In particular, we try to understand and describe the behaviour of emulsions, or suspension of deformable and non coalescing droplets which see broad applications to industry and medicine including waste treatment, food processing and pharmaceutical manufacturing [10, 17].

At a microscopic scale, emulsions are concentrated colloidal suspensions made of soft and deformable particles. A common example is that of blood, made of discrete and highly deformable red blood cells (RBCs) whose microscopic properties can affect the macroscopic rheological behaviour of the fluid [52, 79–81]. For instance, cells affected by malaria are commonly found to be more rigid than their unaffected counterparts. In turn, this induces a distinctive rheological behaviour of the blood [82]. Thus, a better understanding of RBC flow under different conditions such as channel geometry, cell rigidity and shape is essential to develop and optimize new microfluidic devices, drug delivery techniques and even diagnosis protocol.

In Chapter 3 of this thesis, we investigated the dynamics of non-coalescing deformable droplets under pressure-driven flow by means of 2D hybrid lattice Boltzmann simulations. We showed that the emulsion rheology displays a discontinuous shear thinning behaviour, viewed as a non-equilibrium transition

between “hard” and “soft” droplet regimes. The former displays slow flow and caged droplet dynamics whereas the latter is characterised by a fast flow and pronounced droplet deformation.

Having pinpointed the origin of this rich behaviour in the droplet's deformability, we are now interested in characterising the rheological properties as a function of the droplets' surface tension. To this end, we perform hybrid lattice Boltzmann simulations of a 2D emulsion in which we vary the external pressure gradient and the softness of the particles. We show that the non-equilibrium hard-soft transition is progressively shifted towards higher values of the applied pressure-difference as we increase the droplet surface tension and we find that this observation is well captured by a dimensionless capillary number.

To further characterise this discontinuous transition, we perform simulations inspired by typical active microrheology measurements [78, 83–85], where a pre-determined droplet is explicitly pulled through the static suspension. This strategy enables us to study the local rheology of the system and we identify a discontinuous behaviour in the probe velocity with intriguing analogies to the sudden decay in viscosity displayed in the bulk.

## 4.2 Pressure driven flow: hard-soft transition

The simulations discussed in this chapter are performed using the same phase field model described in Section 3.1.1, which uses a system of Cahn-Hilliard equations for the dynamical evolution of the $N$ droplets, coupled to the Navier-Stokes equation which regulates the dynamics of the underlying solvent. The same non-slip boundary condition for the fluid, and normal wetting boundary conditions at the walls for the droplets are implemented in the simulations described in this Chapter. Moreover, all the simulations parameters listed in Section 3.1.1 have been kept constant, with the exception of the value of the surface tension $K$ which now ranges within $[0.02 - 0.25]$.

In this Chapter we aim to understand and characterise the role played by droplet deformability in the flow properties of the overall suspension. To this end, we performed two-dimensional simulations of a suspension of deformable droplets in a liquid medium, subjected to a pressure-driven flow, where we systematically vary the values of droplet surface tension $K$ and applied pressure difference $\Delta P$.

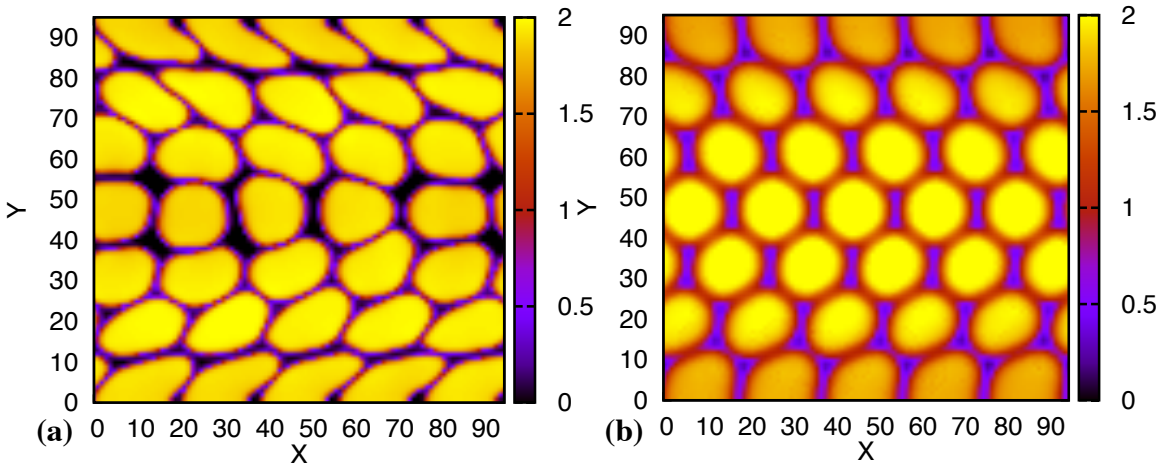


**Figure 4.1** *(a) Snapshot of the simulation of a suspension of* $\Phi = 76.3\%$*,* $K = 0.02$ *subjected to a pressure difference* $\Delta P = 7 \times 10^{-5}$*.(b) Snapshot of the simulation of a suspension of* $\Phi = 76.3\%$*,* $K = 0.18$ *subjected to a pressure difference* $\Delta P = 7 \times 10^{-5}$*. As we can see, lower values of* $K$ *lead to a softer foam, with droplets capable of a string deformation.*

A suggestive image of the extent to which the value of $K$ affects the rheological behaviour of the entire suspension is presented in Fig. 4.1, where the simulation snapshots for two different values of $K$ display a remarkable qualitative difference.

Indeed Fig.4.1**(a)**, which refers to the low surface tension case, shows a suspension made out of droplets which undergo a high degree of deformation and are therefore able to "squeeze" in between their neighbours, consequently allowing the overall suspension to flow easily under the imposed pressure difference. On the other hand, Fig.4.1**(b)** presents a suspension composed of rigid droplets which, being less susceptible to deformation, cause the overall suspension to flow much more slowly.

### 4.2.1 Suspension viscosity and surface tension

To quantitatively characterise the system's rheological behaviour, we measure its effective viscosity $\eta_{eff} = \frac{\eta}{\eta_0}$, where $\eta_0$ is the viscosity of the underlying fluid, as inversely proportional to the suspension throughput flow $Q = \int dy v_x(y)$.

We investigate the correlation between the suspension effective viscosity and the droplets ability to deform, regulated by the value of the surface-tension-like parameter $K$. For simplicity in the rest of the text, we will refer to $K$ as droplet

surface tension. To this end, in Figure 4.2, we plot the effective viscosity $\eta_{eff}$ as a function of the droplet surface tension $K$. Each curve refers to a fixed value of the applied pressure difference which causes the suspension to flow. In line with the results presented in Chapter 3, the suspension effective viscosity undergoes a discontinuous behaviour, now presenting a clear jump towards higher values as we increase the droplets surface tension $K$.

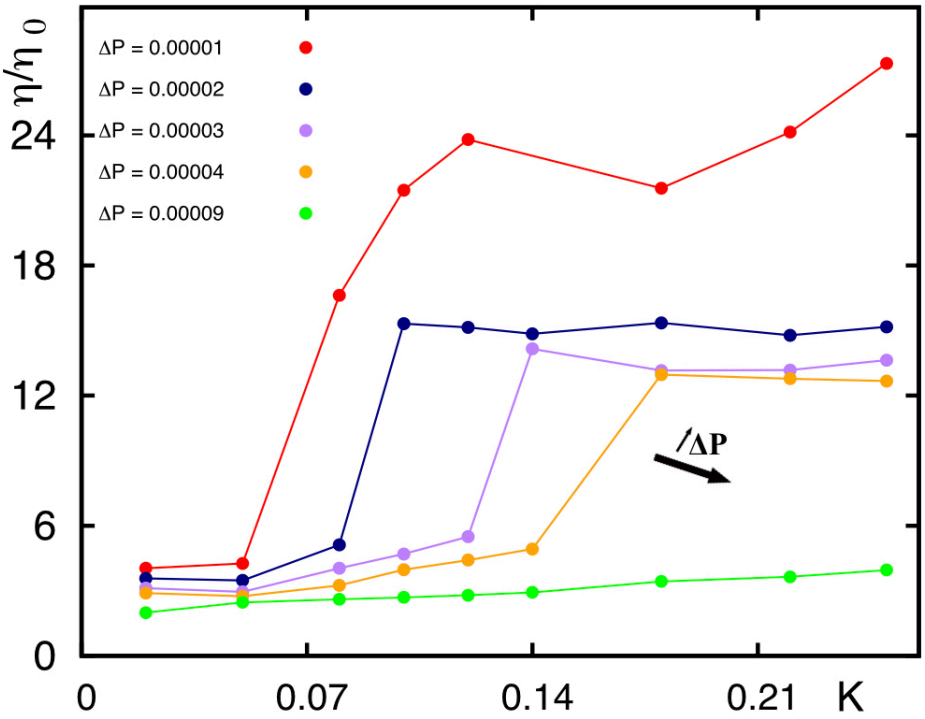


**Figure 4.2** *Plot of the suspension effective viscosity $\eta_{eff}$ as a function of the droplets surface tension $K$ for a system of area fraction $\Phi = 65.4\%$ and different fixed values of the applied pressure difference $\Delta P$. As we can notice, the jump in the viscosity curve is shifted towards higher value of surface tension $K$ as we increase the value of applied pressure difference $\Delta P$.*

The discontinuity shown in Fig. 4.2 can be linked to the discontinuity in the viscosity curve discussed in Chapter 3. The connection between them can be observed by comparing Fig. 4.2 and Fig. 4.4. Indeed, a single line in Fig. 4.2 is given by plotting the vertical points of Fig. 4.4, taken at a fixed value of $\Delta P$. As we can notice, the discontinuity in the viscosity curves in Fig. 4.2 is progressively shifted towards higher threshold values of the surface tension $K$ as we increase the value of the applied pressure-difference. We interpret this

discontinuous behaviour as another mark of the "hard-to-soft" non-equilibrium transition discussed in Section 3.2 in Chapter 3. This interpretation is in agreement with the observed shift of the viscosity jump $\Delta P_{jump}$ as a function of $\sqrt{(}K)$ (proportional tu the real surface tension $\gamma$) shown in Fig. 4.3. Indeed, since higher values of $K$ cause the suspension to be overall less deformable, we expect the transition towards the soft phase to happen for progressively larger values of the applied pressure difference.

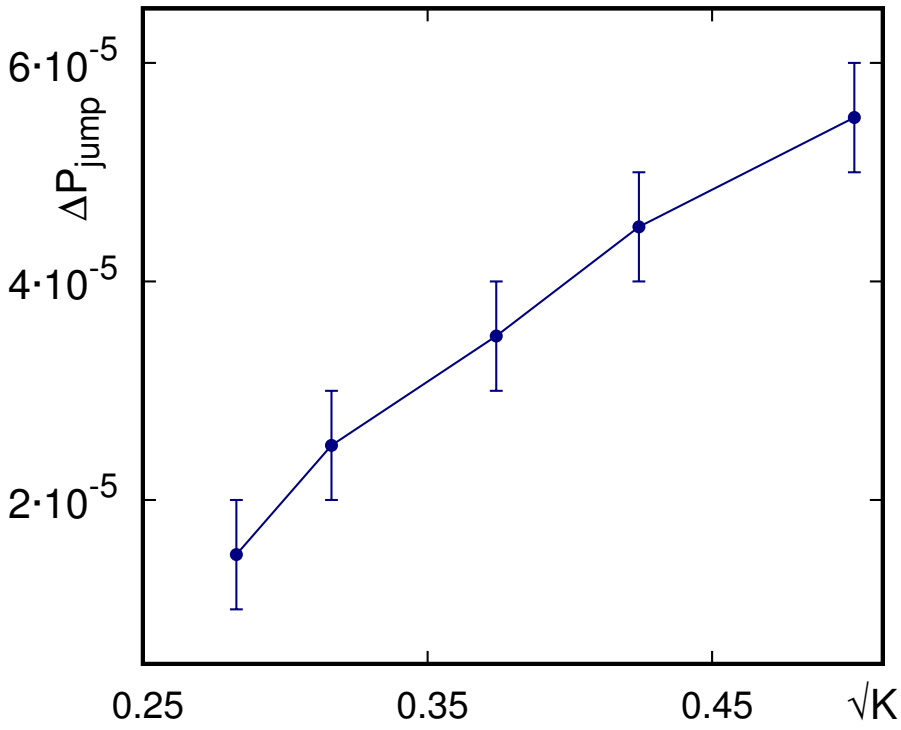


**Figure 4.3** *Plot of the values of the applied pressure difference $\Delta P$ corresponding to the viscosity drop as a function of $\sqrt{K}$, which is proportional to the droplets surface tension $\gamma$ (as explained in Chapter 3 when discussing the free energy functional describing our suspension). As we can notice, the threshold values of $\Delta P$ corresponding to the viscosity jump scales approximately linearly with $\sqrt{K}$. The error bars refer to the interval between the values of $\Delta P$ used in our simulation. Indeed we only fixed discretised value of $\Delta P$ that are multiple of $10^{-5}$.*

### 4.2.2 Discontinuous shear thinning: the role of droplet surface tension

In agreement with the results discussed in Chapter 3, for all the values of droplet surface tension we tested, our suspension undergoes discontinuous shear thinning. The latter behaviour can be observed in Fig. 4.4, where we plot five effective viscosity curves as a function of the applied pressure difference $\Delta P$. The curves refer to different sets of simulations, where we set different values of the droplet surface tension, ranging within $K = [0.02 - 0.25]$ (see for instance the snapshots in Fig. 4.1).

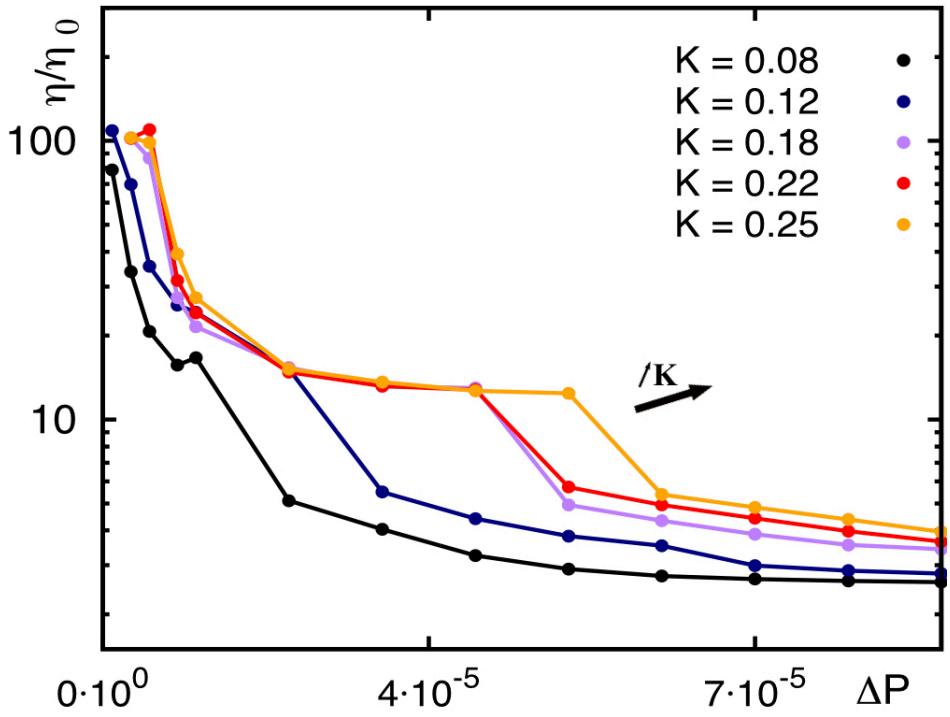


**Figure 4.4** *Plot of the values of the applied pressure difference $\Delta P$ corresponding the the viscosity drop as a function of the droplet surface tension $K$.*

The discontinuous shear thinning behaviour, as discussed in Chapter 3, is a result of the system "hard-to-soft" phase transition. While the former is characterised by almost spherical droplets which tend to resist deformation and flow very slowly, the latter presents droplets that are more susceptible to deformation and therefore flow more easily.

As we can notice from Fig. 4.4, the discontinuity of the viscosity curves is progressively shifted towards higher value of applied pressure difference $\Delta P$ as we increase the imposed droplet surface tension $K$. This result is consistent with our interpretation of an underlying transition from a hard towards a soft phase: for a suspension made out of hard and rigid droplets, we will need a much higher applied pressure difference in order to observe the suspension transition to its soft phase. We note that in the limit for $K \longrightarrow \infty$ we would expect the droplets to behave as a hard-sphere suspension, therefore presenting a shear thickening behaviour for higher values of $\Delta P$.

### 4.2.3 Capillary number

We found empirically that within the parameter range the shape of the viscosity curve is predominantly determined by the following Capillary number

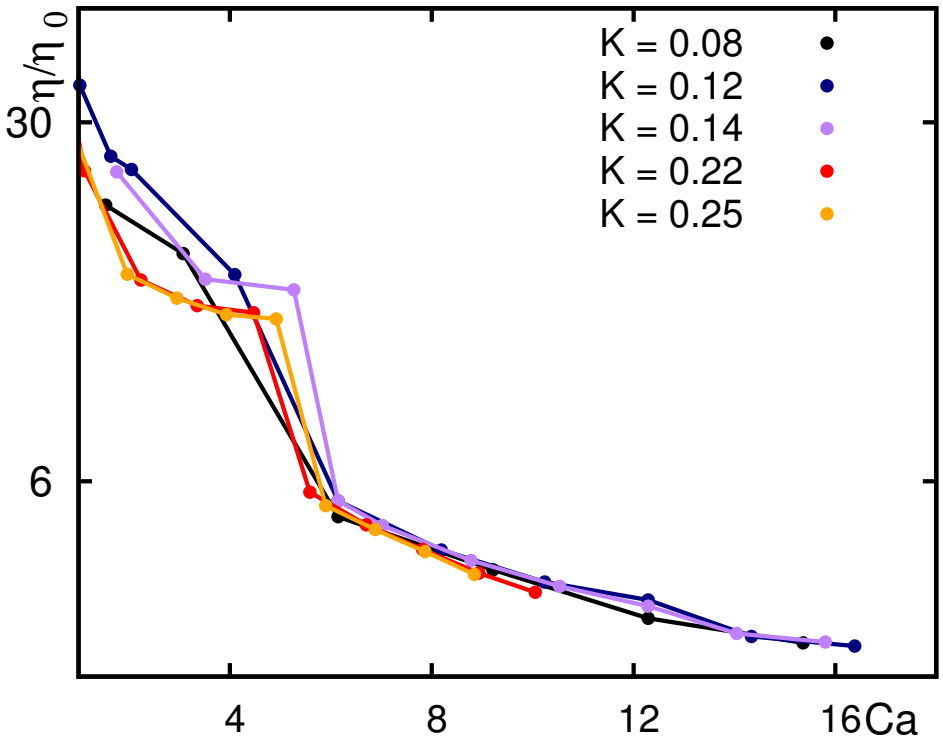


**Figure 4.5** *Plot of the suspension effective viscosity $\eta_{eff}$ as a function of the Capillary number $Ca$ for a system of area fraction $\Phi = 54.5\%$ and different fixed values of the droplet surface tension $K$.*

$$Ca = \frac{\Delta P}{K} L R^2, \tag{4.1}$$

where $L$ and $R$ denote the system size and the droplets' radius, respectively. Of all functional forms of the type $\frac{\Delta P}{K} L^n R^{(3-n)}$ with $n$ integer, this is the combination which leads to the best collapse. Note that while this ratio still measures the relative contribution of viscous and interfacial forces, the latter are now proportional to $K$, the term which enters the free energy density, rather than $\sqrt{K}$ as in the conventional definition of the capillary number.

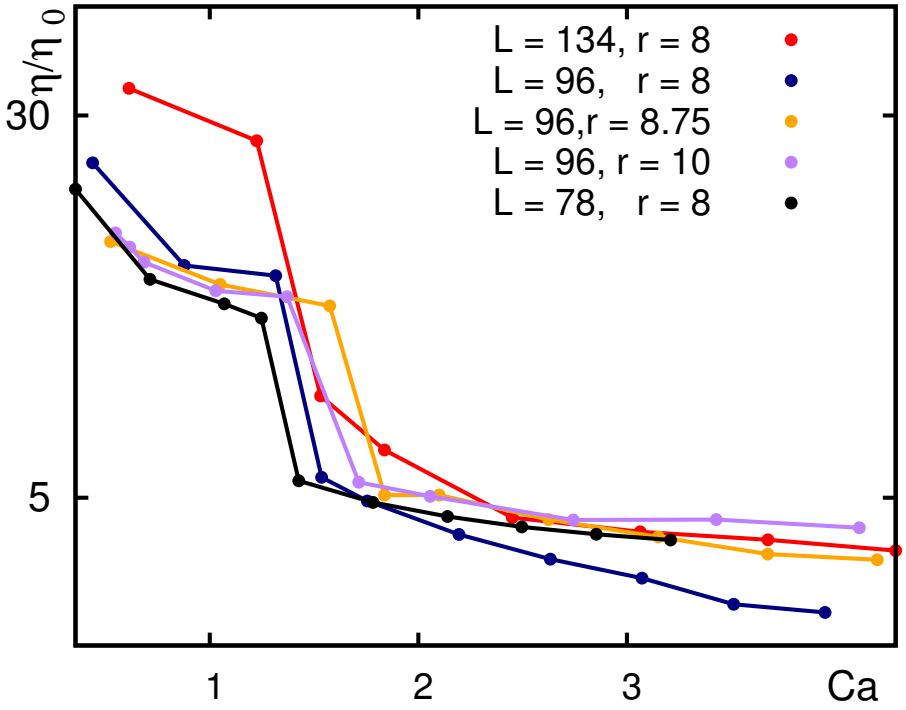


**Figure 4.6** *Plot of the suspension effective viscosity $\eta_{eff}$ as a function of the Capillary number $Ca$ for a system of area fraction $\Phi = 54.5\%$ and different fixed values of the droplet surface tension $K$.*

The usefulness of the Capillary number as a parameter describing the rheological properties of our suspension is demonstrated in Fig. 4.5 and 4.6, where the effective viscosity curves referring to different values of fixed droplet surface tension are plotted as a function of $Ca$. As apparent by comparing Fig. 4.4 and 4.5, the viscosity curves for different values of $K$ all collapse approximately onto the same one when we plot them against the Capillary number (instead of the simple applied pressure difference $\Delta P$). This is in line with the results obtained in [52] a for red blood cell model. Moreover, Fig 4.6 shows that the suspension viscosity curves display a scaling with $Ca$ proportional to $R^2 L$. We can therefore conclude that the Capillary number is the appropriate rescaling

parameter for describing the elastic and flow properties of our suspension.

### 4.2.4 Phase diagrams

Having performed simulations for a variety of different parameters, we are now able to draw a phase diagram describing the transition between the soft and hard phase of our system. As previously explained, the transition between these two phases is marked by a sudden drop in the suspension effective viscosity for a certain threshold of applied pressure difference. We therefore label as "soft" all the cases where the value of viscosity is low, i.e. these are points after the jump in Fig. 4.5. On the other hand, all the cases belonging to the left branch of the viscosity curve, i.e. higher values of $\eta_{eff}$, are labelled as "hard".

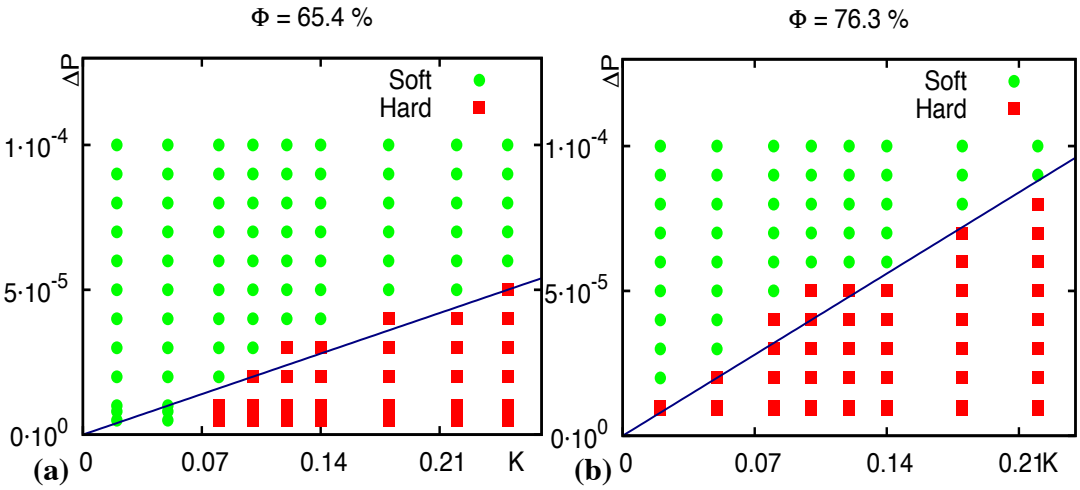


**Figure 4.7** *(a)Phase diagram for a suspension of area fraction* $\Phi = 65.4\%$ *obtained through simulations performed over different values of droplets surface tension* $K$ *and applied pressure difference* $\Delta P$*. The green area represents the soft phase of our suspension, while the red one corresponds to the hard regime.* ***(b)****Phase diagram as in* ***(a)*** *for a system of area fraction* $\Phi = 76.3\%$*. In both plots, the blue line is given by* $\frac{\Delta P}{K} \sim const$*, showing that the transition from the hard to the soft regime happens for a fixed value of Capillary number (*0.0002 *and* 0.0004 *for (a) and (b) respectively).*

In Fig. 4.7 we can observe two phase diagrams corresponding to different values of the suspension area fraction $\Phi$, with increasing values of the droplet surface tension on the x axis, and applied pressure difference on the y axis. The green and

red area corresponds to the soft and hard regime, respectively. Quite intuitively, as we move along the $x-$axis, i.e. increasing $K$ keeping fixed $\Delta P$, our system switches from the soft towards the hard phase. On the other hand, moving along the y axis, i.e. increasing $\Delta P$ keeping fixed the value of $K$, our suspension is undergoing the opposite transition, adjusting from a hard phase to a soft one.

Moreover, the comparison between Fig. 4.7**(a)** and **(b)** suggests that the suspension area fraction $\Phi$ affects the overall system degree of "softness". Indeed, the case where fewer droplets were considered presents a phase diagram where the soft phase, i.e. the green area, is predominant (Fig. 4.7**(a)**). On the other hand, considering higher area fraction (4.7**(b)**), we observe that the red area defining the hard states in the phase diagram increases in size, suggesting that a higher concentration of droplets favours the hard phase.

## 4.3 Micro-rheology

Many experimental data that characterize the rheological properties of a suspension are collected nowadays within the context of microrheology [78, 83–85]. This set of techniques attempts to overcome some of the limitations of bulk rheology such as the sample size and heterogeneity.

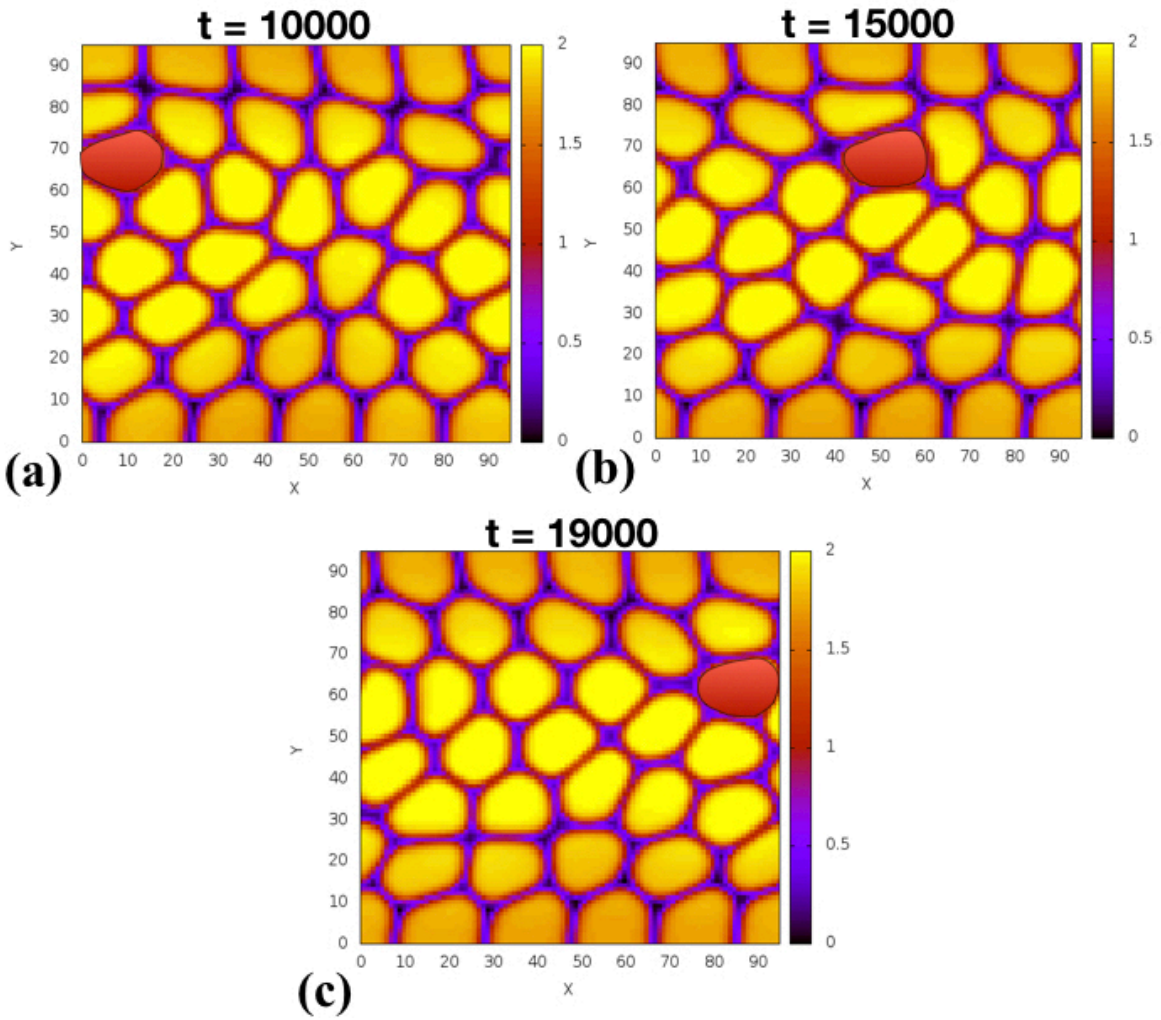


**Figure 4.8** *Snapshot of a simulation of active micro-rheology. The red droplet is the probe which moves due to the applied body-force* $f = 6 \cdot 10^{-5}$*. Plot* ***(a)****,* ***(b)*** *and* ***(c)*** *are taken from the same simulation and refer to different timestep (namely* $t = 10000, 15000$ *and* $t = 19000$*). As we can notice, the probe droplet travels across the entire simulation box within* 9000 *timesteps.*

Indeed, microrheological measurements can be carried out on very small sample volumes, generally tracking the motion of a micron-sized probe particle and using the Stokes-Einstein law or its generalisation to link e.g. diffusion coefficient of the probe to viscosities.

Taking inspiration from this common experimental technique, we performed a set of simulations where the system's rheological properties are probed via micro-rheology. In experiments, this technique is performed by analysing the dynamics of a single probe particle, or droplet, immersed in a suspension. In this way, we are able to extract the rheological properties of the overall suspension avoiding the limitation of a bulk rheology measurement such as the required big sample size. We therefore performed simulations that mimic a typical experiment in active micro-rheology. In order to do so, we simulated our previous two dimensional droplet suspension and directly applied a body-force only on a single droplet chosen as a probe (see Fig. 4.8). This body force is modulated by the phase field of the probe droplet via the term $\sum_i \phi_i \nabla \mu_i$ of Eq. (3.3). Selecting only the phase field $\phi_i$ of the i-th droplet, we apply the forcing only on the probe droplet, forcing its motion through the suspension. We note that we will refer to this body-force as $\Delta P$, in order to draw a comparison with our previous results on the discontinuous shear thinning, although there is no physical connection between the forcing applied on the probe droplet and the pressure difference discussed in the previous chapter. Through this forcing, the probe droplet is able to move across the suspension, while its dynamics over time evolution is carefully tracked and can give useful insights about the overall suspension properties. In analogy with our previous analysis, we performed simulations where we systematically vary the system area fraction $\Phi$ and the values of the body-force applied to the probe droplet. While in our previous analysis, the pivotal quantity used to characterise the suspension rheological properties was its effective viscosity, we now study the trend of the probe velocity over time.

### 4.3.1 Probe velocity and surface tension

In agreement with our previous results, as shown in Fig. 4.9, 4.11 and 4.13 we observe a discontinuous behaviour in the probe velocity curve as a function of the applied body-force. In analogy with the discontinuity in the effective viscosity, this change in behaviour in the probe velocity signals a transition from a hard towards a soft phase. Indeed, for low values of the applied body-force, which we will refer to as $\Delta P$ as in our previous sections, the probe struggle to flow, and is effectively trapped by its neighbouring droplets. On the other hand, we can observe a threshold of $\Delta P$ after which the probe droplet is able to move much more easily across the suspension, which is now composed of droplets that are more susceptible to deformation.

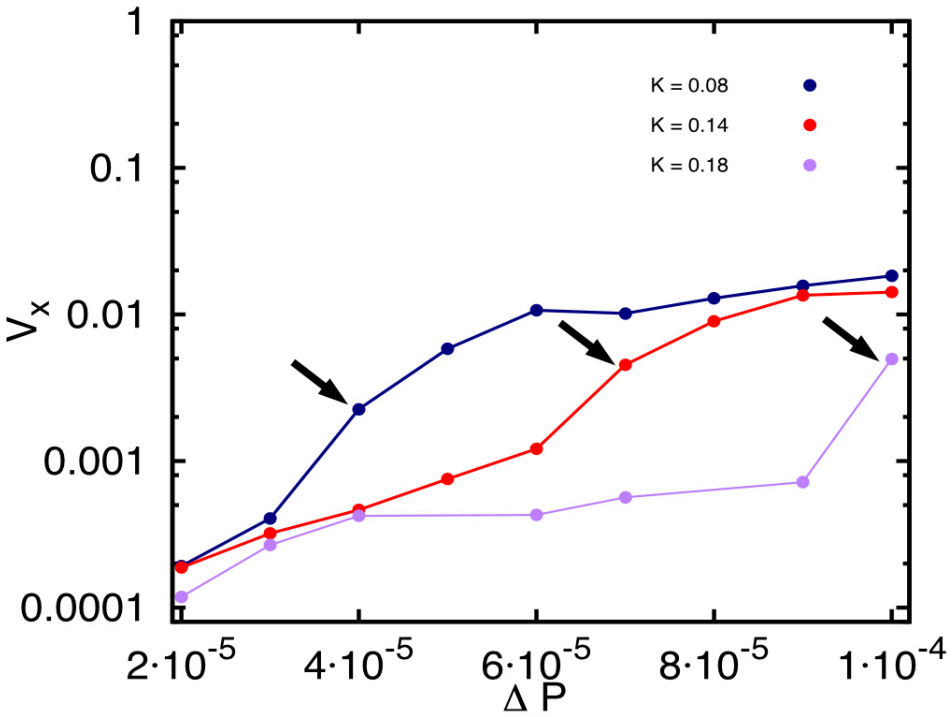


**Figure 4.9** *Probe droplet velocity curves as a function of the applied forcing for a suspension area fraction of $\Phi = 76.3\%$. The three curves refer to different values of the droplet surface tension, namely $K = 0.08$, $K = 0.14$ and $K = 0.18$. As we can notice, the jump in the probe droplet velocity is progressively shifted towards higher values of the forcing as $K$ is increased.*

We are therefore interested in understanding what properties of our system are able to tune the discontinuity which we observe in the probe velocity. To this end, we perform 2D simulations of a suspension of area fraction $\Phi = 76.3\%$, where a range of values for the forcing is applied on the probe droplet. Each set of simulations is then repeated for three different values of the droplet surface tension $K$.

In this way, we first analyse the dependence of this threshold value of the forcing $\Delta P$ which triggers the discontinuity in the probe velocity, as a function of the droplet surface tension $K$.

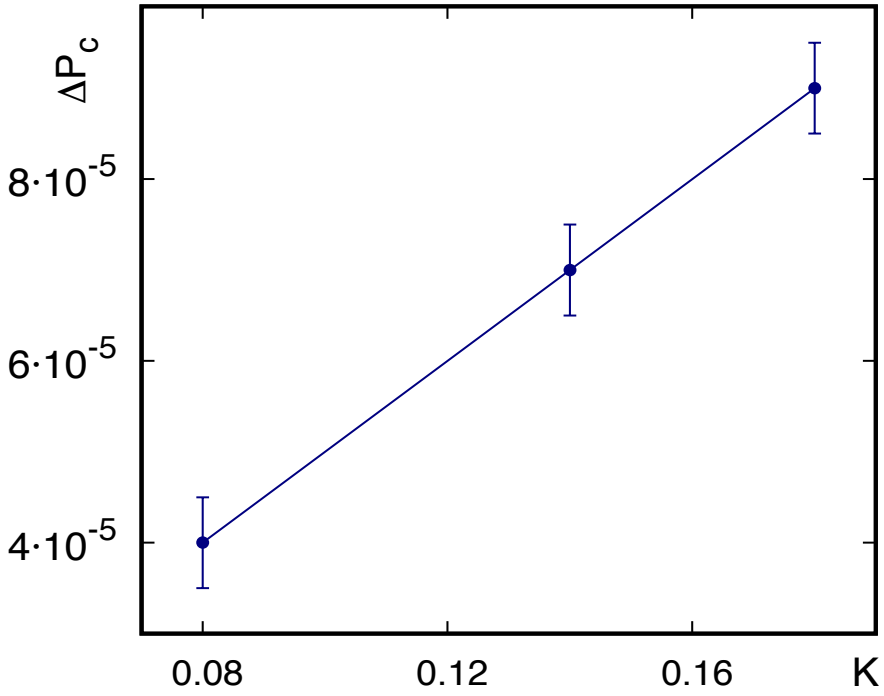


**Figure 4.10** *Plot of the threshold value of the forcing $\Delta P_c$ which triggers the velocity discontinuity as a function of the droplet surface tension. As we can notice, such threshold forcing increases linearly with the droplet surface tension of the overall suspension.*

Similarly to the case of pressure-driven macroscopic flow, in Figure 4.9 we can notice that the discontinuity in the probe velocity occurs for progressively larger

values of the applied forcing as we increase the value of the droplet surface tension. In other words, as our suspension becomes progressively more rigid and overall less deformable, we will need an increasingly higher forcing in order to observe the probe droplet easily flowing across the suspension. Moreover, as shown in Figure 4.10, the threshold value of the forcing needed to observe the discontinuity in the probe velocity increases linearly with the value of the droplet surface tension of the overall suspension, providing us a more quantitative understanding of the role of the droplet surface tension.

### 4.3.2 Probe velocity and area fraction

In this section we study the role played by the suspension area fraction in triggering or tuning the discontinuous behaviour we observe in the probe velocity.

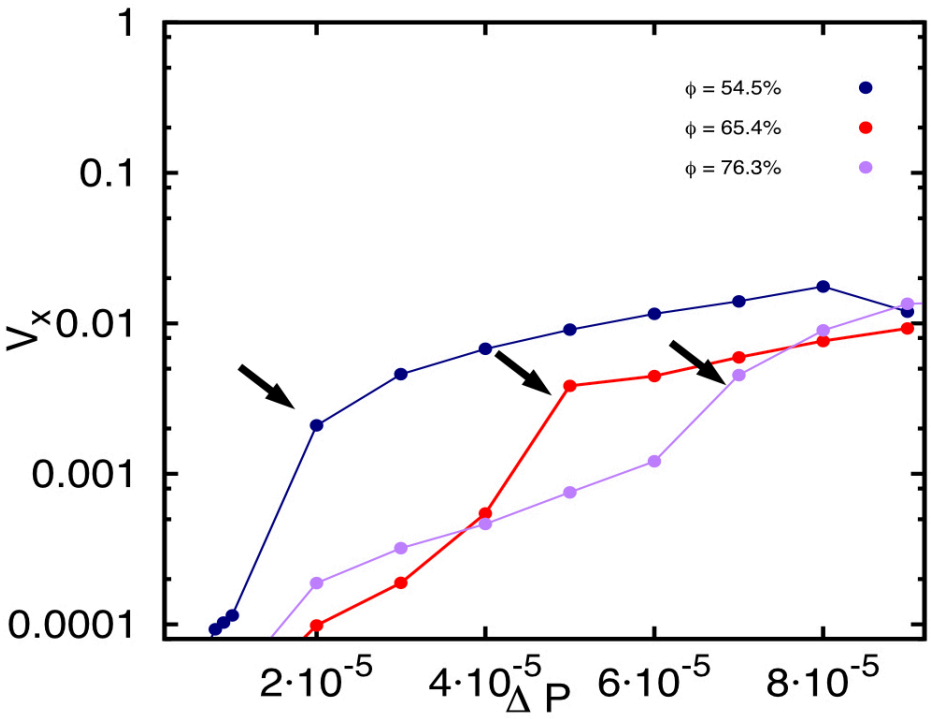


**Figure 4.11** *Probe droplet velocity curves as a function of the applied forcing for a suspension of surface tension $K = 0.14$. The three curves refer to different values of the suspension area fraction, namely $\Phi = 54.5\%$, $\Phi = 65.4\%$ and $\Phi = 76.3\%$. As we can notice, the discontinuity in the probe velocity occurs for progressively higher values of the forcing as we increase the suspension area fraction.*

To this end, we perform simulations of a suspension of droplet surface tension $K = 0.14$ for three different value of area fraction, proportional to the number of droplet of our system, namely $\Phi = 54.5\%$, $\Phi = 65.4\%$ and $\Phi = 76.3\%$.

Analogously to the analysis discussed in the previous section, our results are shown in Figure 4.11 where we plot three curves of the probe velocity as a function of the applied forcing $\Delta P$. The velocity curves refer to the three previously mentioned different value of the suspension area fraction $\Phi$. As we can notice, while the discontinuous trend is always present, in agreement with our previous results, the "singularity" in the velocity of the probe droplet occurs for progressively higher values of the forcing as we increase the suspension area fraction $\Phi$.

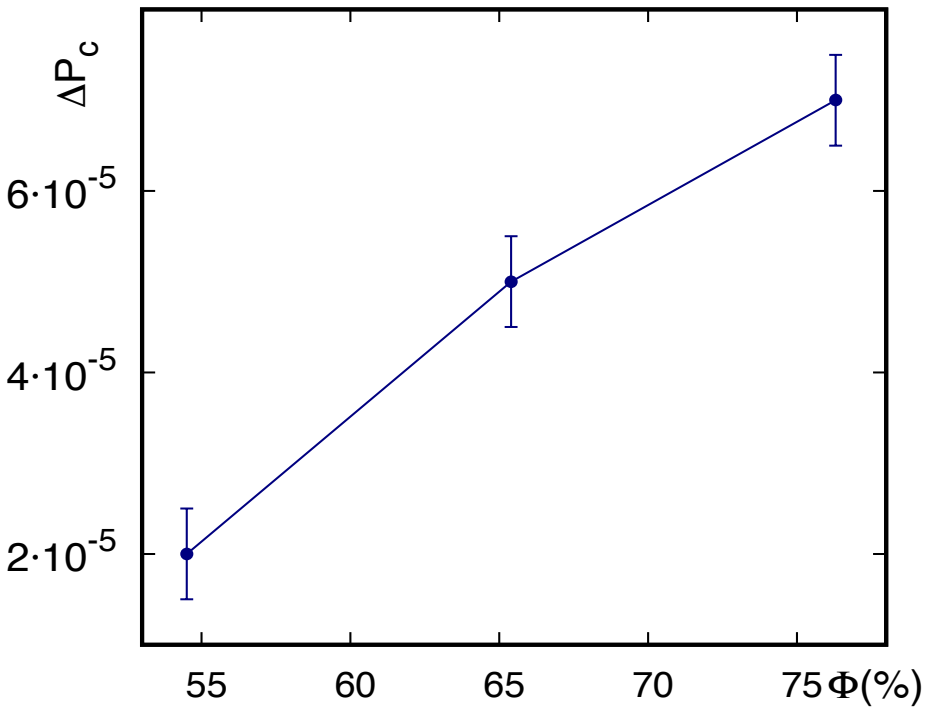


**Figure 4.12** *Plot of the threshold value of the forcing $\Delta P_c$ which triggers the velocity discontinuity as a function of the suspension area fraction. As we can notice, the forcing $\Delta P$ exhibits a linear trend for increasing values of area fraction $\Phi$.*

This progressive shift of the threshold value of the forcing can be interpreted as a sign that our suspension is becoming overall more rigid as the value of its area fraction is increased. This is in agreement with the phase diagrams presented in Figure 4.7 in our previous section, which refers to two different values of area fraction. Indeed, the red area in the two phase diagrams, which represent the so called "hard" phase, is predominant in Fig. 4.7**(b)**, indicating that a higher value of area fraction $\Phi$ causes a decrease in the effective surface tension of the overall suspension.

Moreover, in Figure 4.12 the value of the threshold of the forcing which triggers the discontinuity in the probe velocity is plotted as a function of the suspension area fraction. As we can notice, the threshold forcing exhibits a linear trend for increasing values of $\Phi$.

### 4.3.3 Mixed suspension

Finally, we performed simulations for a so called "mixed" suspension, where we set two different values of the surface tension for the probe droplet and the rest of the suspension respectively.

In particular, we considered the case where a soft probe is dragged across a suspension of more rigid droplets as well as the opposite case, where a hard probe moves within a soft and more deformable environment.

As shown in Fig. 4.13, these two complementary cases produce different thresholds of the forcing which triggers the transition to their soft phase. Indeed, when a soft probe droplet ($K_1 = 0.08$) is immersed in a harder suspension ($K_2 = 0.14$), this transition occurs for a forcing value corresponding to the one previously obtained for the case of homogeneous surface tension of $K = 0.14$ ($\Delta P_c = 7 \cdot 10^{-5}$). On the other hand, considering a hard probe ($K_1 = 0.14$) moving across a soft suspension ($K_2 = 0.08$), the threshold of the forcing shifts towards a lower value ($\Delta P_c = 5 \cdot 10^{-5}$), suggesting a similar behaviour to the overall soft suspension case with homogeneous surface tension $K = 0.08$.

In light of these results, we conclude that within the context of active microrheology, the value of the probe droplet surface tension alone does not have a significant effect on the suspension hard-soft transition.

However, this transition is strongly affected by the value of surface tension of all the droplets forming the suspension, which defines the overall suspension deformability.

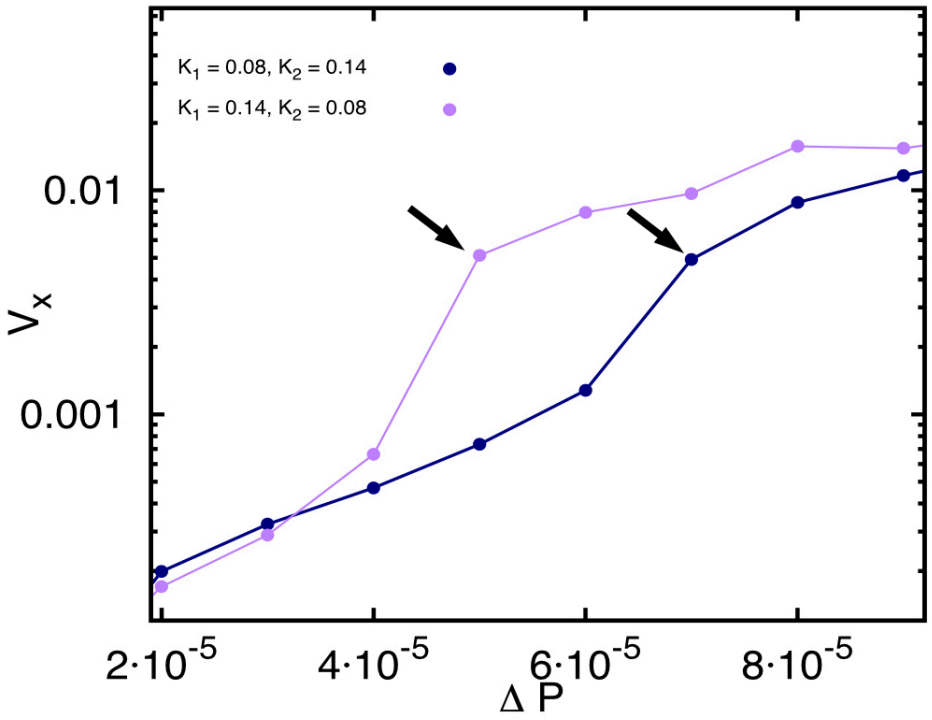


**Figure 4.13** *Probe droplet velocity curves as a function of the applied forcing for a suspension of area fraction $\phi = 76.3\%$ for different values of the surface tension. In these simulations, the probe is characterised by a different surface tension ($K_1$) with respect to the rest of the rest of the droplets ($K_2$). The purple curve refers to the case where the we simulate a "hard" probe moving across a "soft" suspension, while the blue one corresponds to the opposite case.*

## 4.4 Concluding remarks

To summarize the results presented in this Chapter, we performed two dimensional lattice Boltzmann simulations of a suspension of non-coalescing, deformable droplets where the role of the droplet surface tension was investigated. In order to test the properties of deformability of our system, we performed simulations where we systematically vary the applied pressure difference as well as the droplet surface tension. Our results show that the observed hard-soft transition progressively shifts towards higher values of applied pressure difference as we increase the droplet surface tension. In other words as shown in Fig.4.4 and Fig. 4.7 , a more rigid system (high values of $K$), will need a higher threshold value of the applied pressure difference to trigger its transition towards the soft phase.

The rheological properties of our suspension can also be characterised via its Capillary number $Ca$, defined as in (4.1). This parameter, which captures the interplay between the droplets' elastic properties and the overall system flow, can be used to scale the system viscosity curves as shown in Fig. 4.5 and 4.6. Indeed, when plotted against the Capillary number, all the viscosity curves referring to different fixed values of the surface tension collapsed onto the same curve, showing that $Ca$ captures the relevant mechanisms controlling the suspension viscosity. This is important as the master curve allows simple predictions of flow curves at different $L$, $\Delta P$ and $K$ (provided that the area fraction $\Phi$ stays constant).

Finally, we test our system properties through simulations where we mimic an active microrheological experiment, where a single probe droplet is dragged across the overall domain. Systematically varying the value of the body-force applied on the target droplet, we observe a discontinuous behaviour in the velocities of both the probe droplet and its neighbours. In agreement with the discontinuous shear thinning previously observed, this velocity discontinuity is another mark of the hard-soft transition that our suspension is undergoing.

We can therefore conclude that the suspension's deformability, characterised by the droplets' surface tension, the overall suspension area fraction and its Capillary number, play a pivotal role in defining the rheological and flow properties of a droplet suspension. Indeed, both in the context of pressure-driven flow and of active micro-rheology, the suspension's ability to deform can tune the threshold of the forcing needed in order to trigger the transition from a hard phase, where

the droplets are more rigid, towards a soft one, characterised by droplets which are significantly more susceptible to deformation. Moreover, we argue that the model presented in this chapter could be used to qualitatively describe the flow properties of red blood cells and, in general, to understand the flowing properties of suspensions made of deformable elements.

# Chapter 5

# Irreversibility transition

It is known that many physical systems are described by laws and equations that are time reversible. The time reversibility of simple flow of a Newtonian fluid at low Reynolds number (Re) has been demonstrated by Taylor in his famous Couette flow experiment [86]. Here, two or more drops of dye are placed in a fluid in the gap between concentric cylinders (circular Couette flow geometry). One then proceeds to rotate the inner cylinder, for a certain number of cycles, until the drops of dye are spread into a thin filaments. As the time reversibility predicts (but still surprisingly to actually observe), when one inverts the rotation of the inner cylinder, after performing the same number of cycles, every drop of dye moves back so as to reconstitute its initial shape. The reversible creeping flow equations also regulate the low Reynolds number dynamics of a suspension of non-Brownian particles, i.e. a suspension where the particles are too big to exhibit thermal motion.

Despite this, experience tells us that many of these reversible systems actually present a transition towards an irreversible regime, where chaotic or non predictable behaviour replaces deterministic dynamics. For instance, previous experimental [87–90] and numerical investigations [91, 92] have shown that the trajectories of non-Brownian particles exhibit irregular random displacements when a suspension is sheared between concentric cylinders. The origin of this irregular motion lies in the interactions between the particles and the surrounding fluid, producing remarkable effects on the overall suspension behaviour. A detailed experimental study on reversibility [93], conducted by periodically straining a viscous colloidal suspension in a Couette geometry, shows that

hydrodynamic interactions can lead either to reversible or irreversible motion, depending on the amount of deformation that is imposed on the suspension. These findings demonstrated that although the creeping flow equations are reversible and deterministic, the parameter range in which such behaviour is observed is still quite limited. In particular, this study shows precisely how time reversibility fails for slowly sheared suspension, and finds a concentration dependent threshold for the deformation beyond which particles do not return to their original positions. Moreover, this threshold strain is associated with a pronounced growth in the Lyapunov exponent which measures of the strength of the chaotic particles interactions. The comparison illuminates the connections between chaos, reversibility and predictability.

Many-body systems are known to be able to self-organise into ordered structures starting from random configurations. On the other hand, non-equilibrium systems also self-assemble, but no theoretical framework yet exists for treating such phenomena. Indeed, experiments on well-characterised model systems are needed to guide theory development. For instance, the work from Corté et al. [94] shows how suspensions with low values of volume fraction ($\Phi < 0.3$) under periodic shear self organise into a non-fluctuating "absorbing" state characterised by collision avoidance. If collisions avoidance was the only mechanism responsible for observing a reversible behaviour, we should expect adsorbing states to disappear for higher values of volume fraction. Intriguingly, we find the opposite result, observing a range of the phase diagram characterised by reversible behaviour even for high $\Phi$.

In this Chapter we aim to understand the reversibility properties of our deformable droplet suspension, shedding light on the onset of irreversibility and loss of predictability. To this end, as shown in the following sections, we use two different sets of simulations which represent two distinct ways of imposing a deformation on our system and therefore testing its reversibility properties. In the first section, a droplet in our suspension is periodically inflated and deflated, therefore causing an overall rearrangement of the neighbouring droplets. On the other hand, in the second section an oscillatory shear is imposed on the boundary walls. In both cases, the droplets position is carefully tracked, enabling us to verify whether, after each period of the imposed deformation, all the droplets come back to their original positions, and therefore our suspension shows a reversible behaviour. As we will see, a transition between a reversible and an irreversible phase is detected and found to depend on the amount of deformation.

## 5.1 Growing droplet

As previously mentioned, in this Chapter we analyse the reversibility properties of our two-dimensional system when subjected to an external deformation. In particular, we first focus on the case where a selected droplet, which we will refer to as the "growing droplet", within our suspension undergoes periodic inflation to a bigger final area followed by subsequent deflation until its original size is recovered.

Performing simulations where we systematically vary the inflation/deflation period and growth rate, we were able to identify the region in the parameter phase diagram where the suspension dynamics is reversible. For such parameters all neighbouring droplets find themselves at their original position after a period of the deformation of the growing one. On the other hand, the remaining part of the phase diagram is characterised by an irreversible behaviour of our suspension. Our simulations thus enable us to distinguish a marked phase transition between the reversible and irreversible regimes.

### 5.1.1 The model

For our simulations we use the same phase field framework described in Chapter 3. Thus, we use a Hybrid Lattice Boltzmann method to investigate the dynamics of a two-dimensional suspension of soft, non-coalescing droplets - this time perturbed by the periodical inflation and deflation of an arbitrarily chosen droplet within our system. The free energy density discussed in Chapter 3 as well as the hydrodynamic implementation through the Lattice Boltzmann method are also used in this Chapter. However, once we have chosen our growing droplet, to inflate and deflate its area we need to modify the Cahn-Hilliard equation describing the evolution of its phase field $\phi_G$. In particular, an additional term defining the growth rate $\alpha\Phi_G$ has to be introduced:

$$\frac{\partial \phi_G}{\partial t} + \nabla \cdot (\mathbf{v}\phi_G) = M\nabla^2\mu_G + \alpha\phi_G \tag{5.1}$$

where the sign of the growth rate $\alpha$ defines if the droplet is going to increase or decrease its area.

This dynamic equation implies an exponential growth of the selected droplet, as defined by

$$\frac{dA}{dt} = \alpha A \qquad \longrightarrow \qquad A(t) = A_0 e^{\alpha t} \tag{5.2}$$

where $A(t)$ and $A_0$ denote the droplet area at time $t$ and initial value, respectively. In order to have a periodic increase and decrease of the droplet area, we define a set value for the deformation period $T$ such that:

$$\begin{cases} A(t) = A_0 e^{\alpha t} & t < T \\ A(t) = A_0 e^{\alpha (T-t)} & t > T. \end{cases}$$

In this way, after reaching its maximum size $A(T)$, the growing droplet will start deflating, therefore decreasing its area until reaching its original size $A_0$. Note that for adiabatic (quasi-static) inflation-deflation cycles, we would expect results to only depend on minimal and maximal area, so on the product $\alpha T$, rather than on $\alpha$ and $T$ separately.

The dynamics of the rest of the droplets within the suspension is described by the same set of Cahn-Hilliard equation (3.2) discussed in Chapter 3, and their time evolution is carefully tracked during our simulations.

### 5.1.2 Irreversible transition

In order to test the reversibility properties of our suspension we perform simulations where we systematically vary the deformation period as well as the growth rate. Tracking the droplet positions and comparing them at each time after a deformation period, we are able to distinguish the cases where the droplets configuration is the same before and after a period $2T$, and cases where such comparison gives the opposite result.

As previously explained, the periodic deformation on our suspension is imposed through area inflation of a central droplet for a certain time $T$, followed by its consequent deflation which restores the corresponding area to its original one after another time $T$. As we can notice, the simulation snapshots in Fig. 5.1**(a)** and **(b)**, taken at times separated by $2T$, display the same droplets configuration

across the suspension. Such behaviour is only guaranteed in the case of a reversible system, described by time-reversible equations of motion.

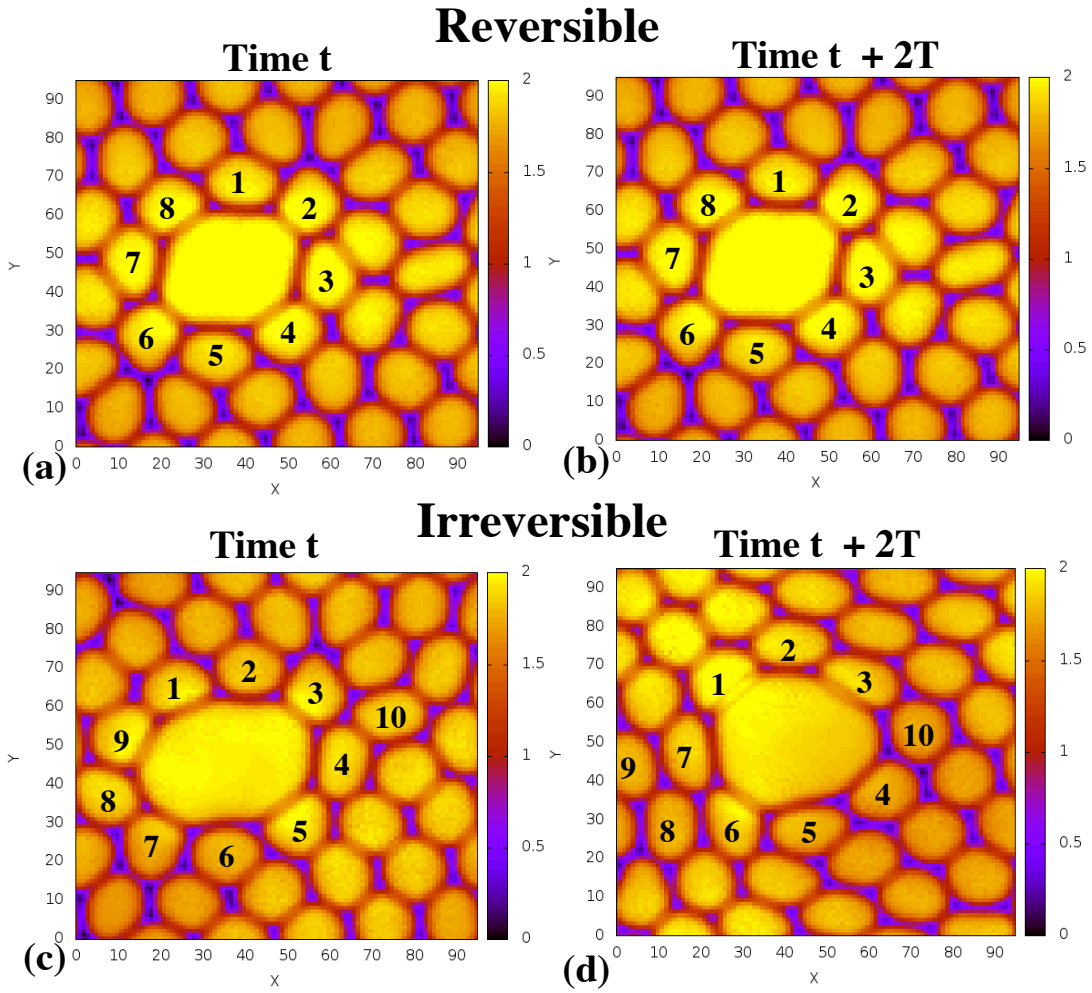


**Figure 5.1** *(a) Snapshot of a simulation at a time t where the central droplet of our suspension is periodically inflated and deflated. (b) Same as (a) but at time $t' = t + 2T$, i.e. after the central droplet is deflated until it reaches its original size and the suspension droplet configuration should be identical to the time before the droplet inflation. Comparing (a) and (b) we can observe that they are qualitatively identical, i.e. our suspension shows reversible behaviour. (c) Snapshot of a simulation at a time t where the central droplet of our suspension is periodically inflated an deflated. (d) Same as (c) but at a time $t' = t + 2T$, i.e. after a period of inflation-deflation of the central droplet. Comparing (c) and (d) we can notice that the neighbouring droplet configuration (labelled with numbers from 1 to 10) shows significant difference between the two snapshots, indicating that our suspension is presenting irreversible behaviour.*

On the other hand, for an irreversible system, we expect a significant change

in the overall droplets configuration across the suspension after reversing the imposed deformation. An example of irreversible behaviour can be observed in Fig.5.1**(c)** and **(d)**, as well as in Suppl. Movie 5 where we observe the trajectory of a neighbouring droplet as the central one inflates and deflates [1]. As for the previous examples Fig.5.1**(a)** and Fig.5.1**(b)**, Fig.5.1**(c)** is taken at a time $t$, while Fig.5.1**(d)** refers to a time $t' = t + 2T$, so that the inflated droplet has the same area in both snapshots. Observing these last two images, we notice that they show a qualitative difference in the overall droplets configuration, as indicated by the numbers labelling the neighbouring droplets. We can therefore consider this case as an example of the suspension showing irreversible behaviour.

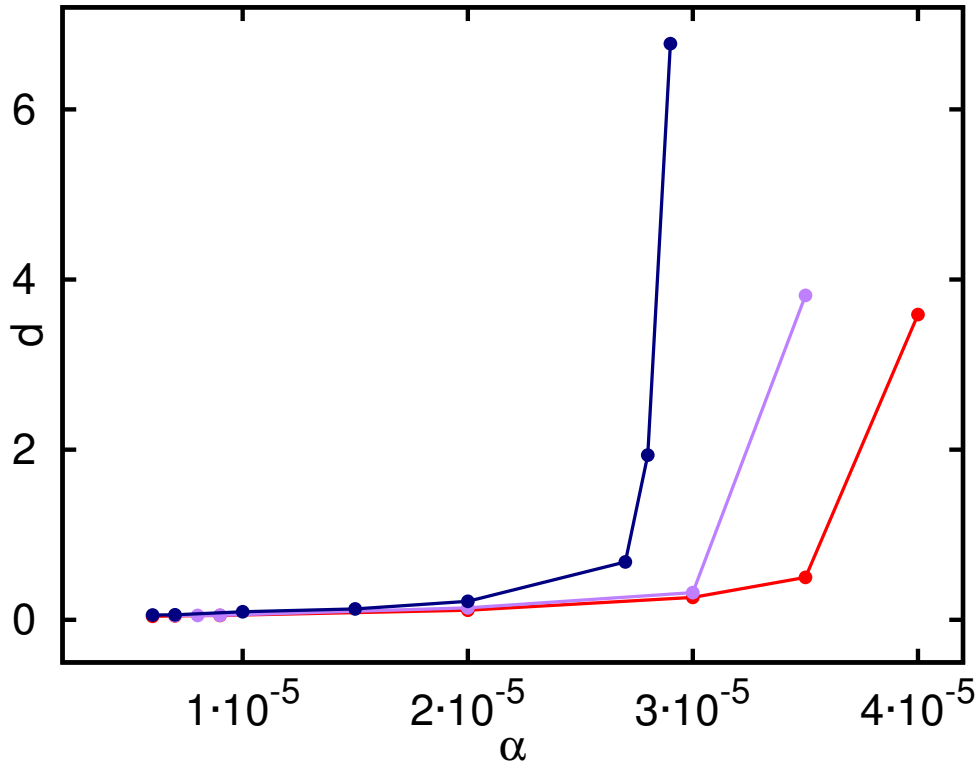


**Figure 5.2** *Average of the droplets displacements after each inflation/deflation period of the central growing droplet as a function of the imposed growth rate $\alpha$. The three curves refer to different values for the deformation period $T$ (the time we let the droplet increase its size, and consequently decrease it). As we can notice, $\langle | \vec{r}(t) - \vec{r}(t+2T) | \rangle$ (expressed in lattice units) shows a sharp increase towards higher values, signalling a transition towards an irreversible phase.*

[1] The supplementaty movies can be found on https://datasync.ed.ac.uk/index.php/s/FUhZkTvl4Nqs3yI accessible using password: foglino

A more quantitative interpretation of the occurrence of a reversible-to-irreversible phase transition comes from calculating the average displacements of the droplets after each period of deformation $d = \langle | \vec{r}(t) - \vec{r}(t + 2T) | \rangle$, where $\vec{r}$ denotes the droplet position and the average is taken both over time and over the total number of droplets.

We should obtain $d_{rev} \sim 0$ in the reversible scenario, where each droplet after a period of increase/decrease of the growing one, comes back to its original position. On the other hand, the irreversible case implies that, after each period, some or all of the neighbouring droplets surrounding the growing one will find themselves in a different position with respect to its original one, i.e. $d_{irr} \gg d_{rev}$.

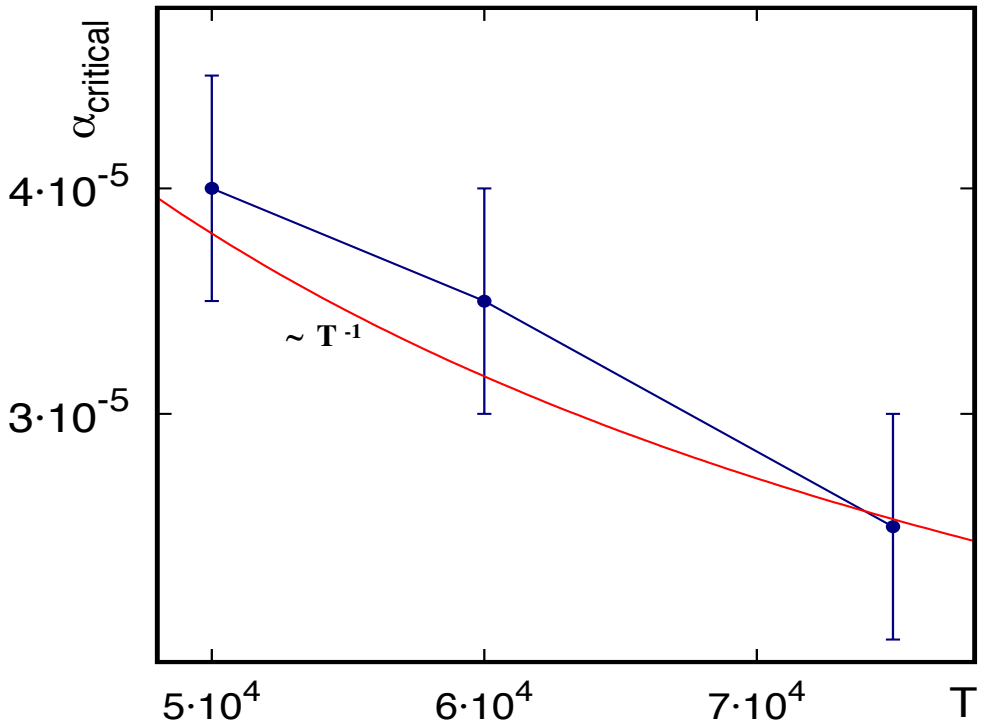


**Figure 5.3** *Threshold value for the growth rate $\alpha_{critical}$, which signals the system's transition to its irreversible phase, as a function of the imposed deformation period $T$. As we can notice, this threshold decreases linearly as the value of $T$ is increased. The error bars refer to the interval between the values of $\Delta P$ used in our simulation. The red line is proportional to $\frac{1}{T}$.*

We therefore calculate this quantity for different values of the period $T$ and observe its trend as a function of the imposed growth rate $\alpha$, as shown in Fig. 5.2.

Here, the three curves, which refer to different values of deformation period $T$, present a sharp increase for progressively higher values of the growth rate $\alpha$, denoting a transition towards the irreversible scenario. Considering the difference in the values of $d$ between each pair of points in this plot, we can define a threshold value of the growth rate $\alpha$ corresponding to the largest increase of each curve (last point of each curve). We note that if we had considered higher values of $\alpha$ (not computationally accessible), we could have found even bigger increase in the points of the curve. As we can notice, this threshold is progressively shifted towards lower values for increasing values of $T$ (see Fig. 5.3). We can therefore conclude that a system subjected to a deformation for a shorter period of time $T$, needs a higher value of growth rate $\alpha$ in order to undergo its transition towards the irreversible phase. In other words, short deformation period are more likely to cause reversible behaviour.

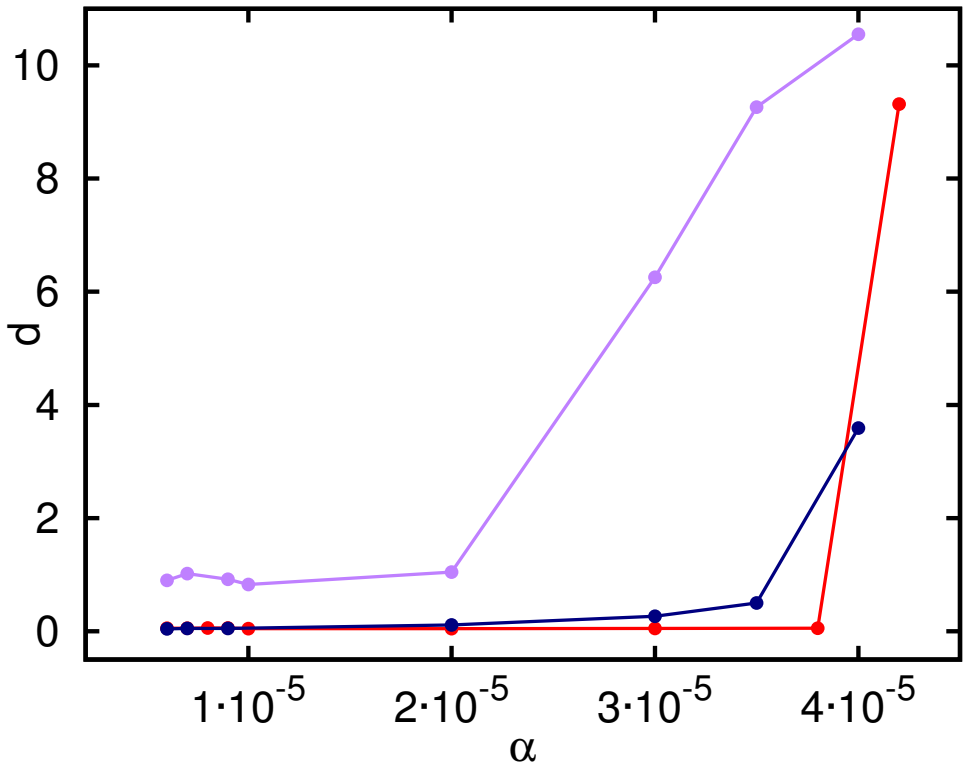


**Figure 5.4** *Average of the droplets displacements after each inflation/deflation period of the central growing droplet as a function of the imposed growth rate $\alpha$. The three curves refer to different values of the droplet surface tension $K$. As we can notice, $d$ (expressed in lattice units) shows a sharp increase towards higher values, signalling a transition towards an irreversible phase.*

As discussed in Chapter 4, the deformability properties of our suspension, defined by the droplet surface tension, play a pivotal role in its overall rheological behaviour. In particular, the value of the surface tension can be used to tune the hard-to-soft transition discussed in the previous Chapter. We are therefore now interested in quantifying the influence that the suspension deformability properties might have on the system reversible-irreversible transition.To this end, we perform simulations for different values of the growth rate $\alpha$ and droplet surface tension $K$, keeping fixed the deformation period $T$. Our results are shown in Fig. 5.4, where analogously to Fig. 5.2, we plot the values of $d$ as a function of the growth rate $\alpha$.

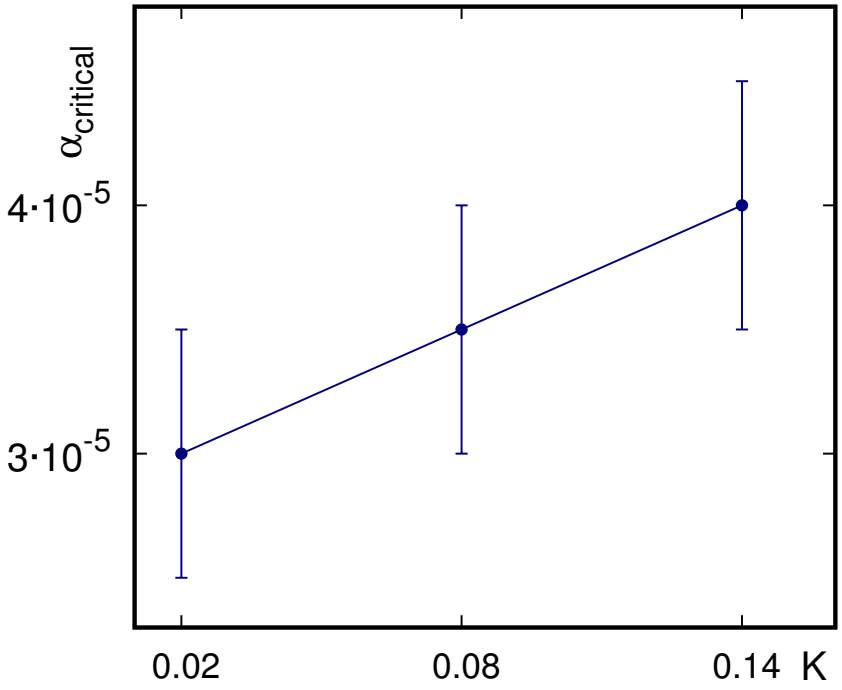


**Figure 5.5** *Threshold value for the growth rate $\alpha_{critical}$, which signals the system transition to its irreversible phase, as a function of the imposed droplet surface tension $K$. As we can notice, this threshold increases linearly as the value of $K$ is increased. The error bars refer to the interval between the values of $\Delta P$ used in our simulation.*

The three curves, referring to different values of the droplet surface tension $K$, show again a sharp increase for progressively higher values of the growth rate, signalling a transition towards the irreversible phase. However, we can notice that the threshold value for the growth rate $\alpha_{critical}$ signalling the transition

is progressively shifted towards lower values as the droplet surface tension is decreased (see Fig.5.5).

A comparison can be drawn between Fig. 5.5 and Fig.4.3 (in Chapter 4), where we plot the threshold value of the pressure difference $\Delta P_{jump}$, which causes the transition towards the soft phase, as a function of the surface tension $K$. For both cases, these two respective threshold quantities are shifted towards a higher value as the droplet surface tension is increased. We can therefore conclude that a softer suspension, which can be easily deformed, shows a transition to its irreversible phase for a lower value of the growth rate with respect to a harder one. In other words, the softer the suspension, the easier is to observe an irreversible behaviour.

### 5.1.3 Phase diagrams

Having observed scenarios where our suspension presents either reversible or irreversible behaviour, we are now able to draw a phase diagram which can give an indication where in the parameter space these behaviours occur.

To this end, for each choice of growth rate $\alpha$ and deformation period $T$, we compare snapshots of our simulations taken at different timesteps, adding the period of deformation $2T$ at every time. This qualitative comparison can be used to distinguish the suspension behaviour: if the overall droplet configuration is identical after each period, we label the case as "reversible"; on the other hand, if there is a clear difference in the droplet positions before and after each deformation period, we label the case as "irreversible".

The correspondent reversibility phase diagram is shown in Fig. 5.6, where each green dot represents a reversible scenario, while the red points indicate an irreversible one. As we can notice, it is clear that increasing the growth rate $\alpha$ or the deformation period $T$ leads towards the irreversible part of the phase diagram, i.e. a fast, or prolonged, deformation causes the system to more easily fall into an irreversible behaviour.

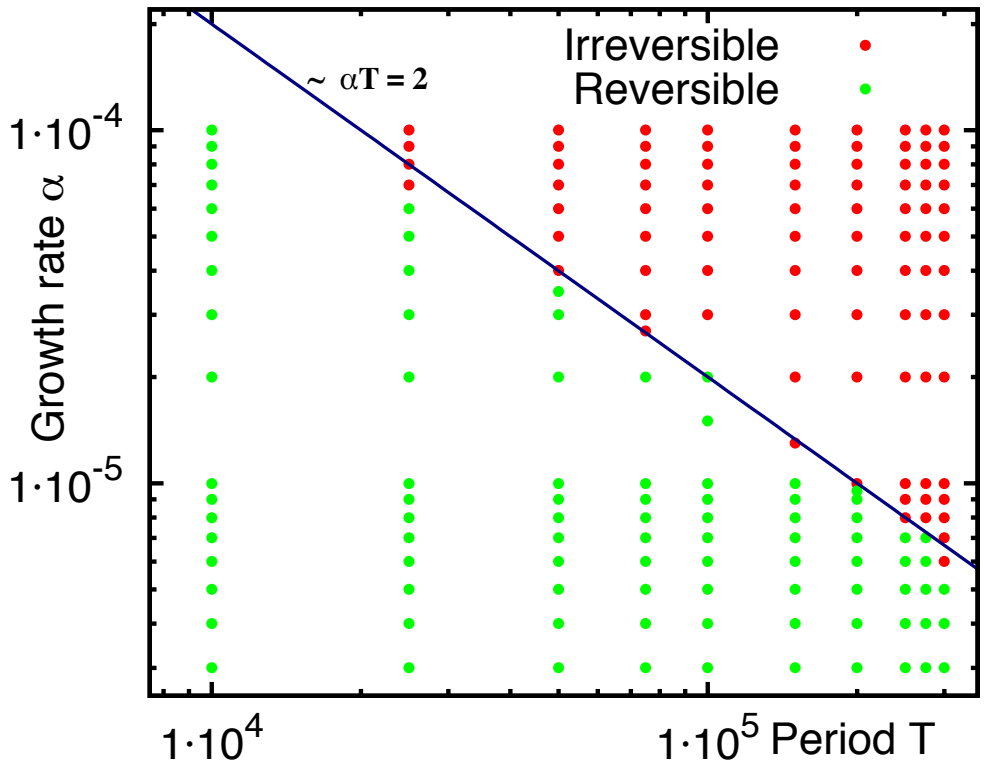


**Figure 5.6** *Reversibility phase diagram for the growing droplet scenario, where the central droplet of the suspension increases and decreases its area with period $2T$ (the suspension area fraction is $\phi = 76.3\%$). The green dots represent reversible cases, i.e. the droplets positions are identical after each period of the droplet growth, while the red ones indicate an irreversible behaviour, i.e. the droplets configuration changes after each period of the central droplet growth. The blue line is given by $\alpha T = 2$, marking the transition between the reversible and the irreversible phase.*

Moreover, Fig 5.6 shows that the crossover region between the reversible and irreversible phase is dependent on the product $\alpha T$, rather than on $\alpha$ and $T$ separately. Indeed, for our simulations the value of such product corresponding to the transition to the irreversible phase is approximately constant, $\alpha T_{crossover} \approx 2$ .

### 5.1.4 Reversible phase: limit cycles

Having observed a transition between a reversible behaviour and an irreversible one, we are now interested in analysing the characteristics of the reversible cases.

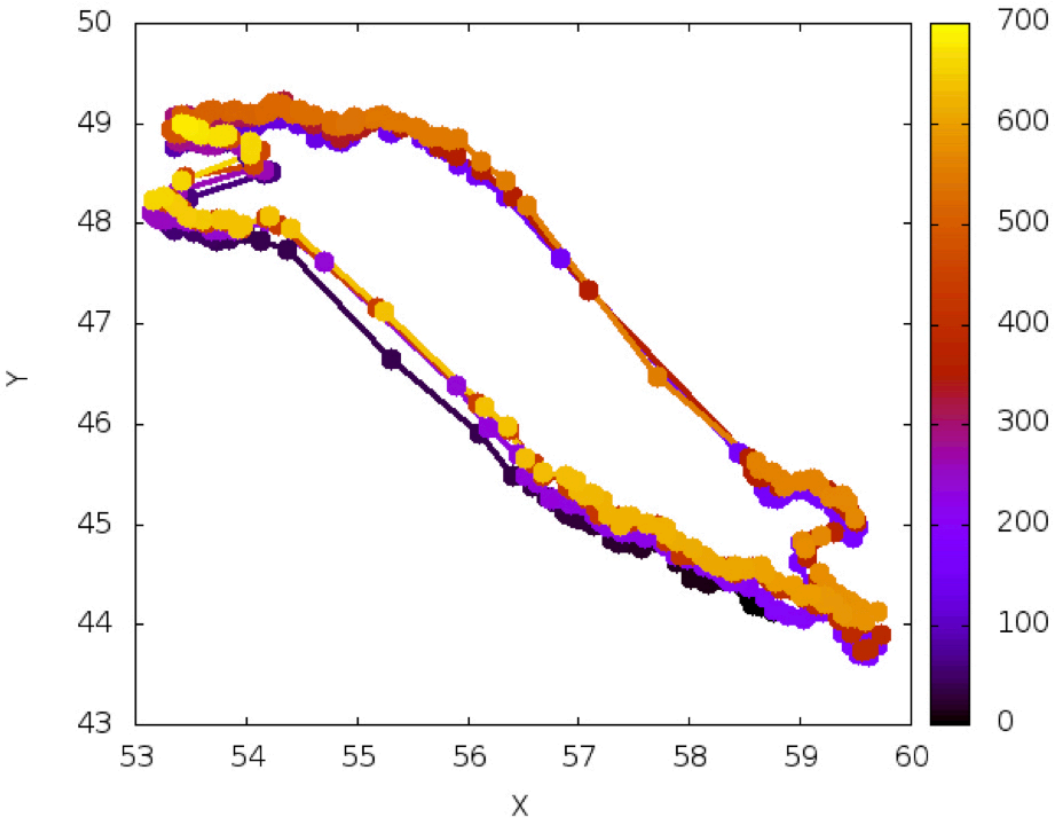


**Figure 5.7** *(x,y) trajectory of a certain droplet within the suspension, showing a repetitive limit cycle. The colour code indicates time evolution.*

From the literature, the way specific microscopic processes organise, i.e. the material bulk rheology, is generally not well understood [93]. We are therefore interested in characterising the suspension's structure, in order to try to understand the mechanisms that regulate the overall suspension reversibility.

Observing the evolution of the droplet positions over time, we noticed that about half of the droplets in our suspension undergo a "limit cycle". In particular, while the central droplet is increasing its size, the neighbouring droplets will need to spatially rearrange, and will reach, after time $T$, a new position following a particular path. At that point, the central droplet begins to deflate, causing

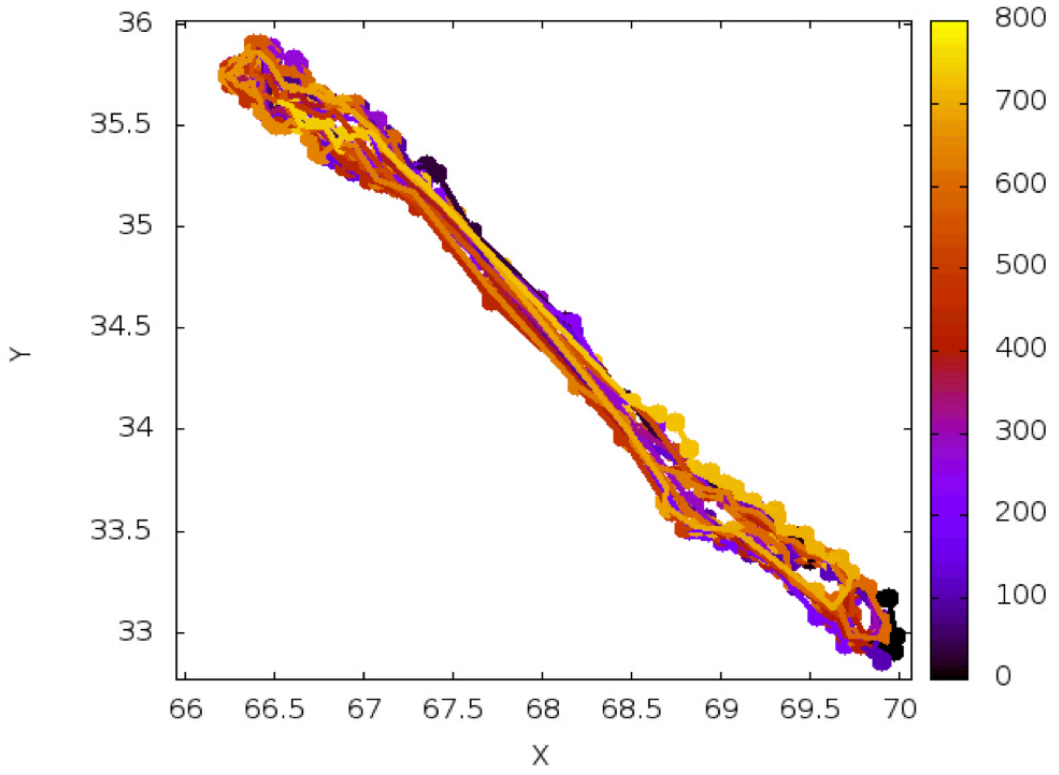


**Figure 5.8** *(x,y) trajectory of a certain droplet within the suspension, showing a repetitive limit cycle. The colour code indicates time evolution.*

the surrounding droplets to move again until they reach their original position after another time $T$. During this second part of their movement, those droplets might choose a different path with respect to the first one to get to their original position, giving rise to circular trajectories in the $(x, y)$ plot.

This behaviour is what we called a limit cycle, an example of which can be seen in Fig. 5.7. Here, we plot the $(x, y)$ trajectories of a certain droplet within the suspension for many timesteps as indicated by the colour code. As we can notice, the droplet is undergoing the same trajectory in a repetitive circular way, reaching its original position after a period $2T$ of the deformation due to the central growing droplet.

The alternative path a droplet can follow, during deflation of the growing droplet, in order to reach its original position is to retrace back its previous trajectory (followed during inflation). An example of this second kind of droplet path is shown in Fig. 5.8, where we can notice a more linear repetitive trajectory.

More generally, in Fig. 5.9 we plot all the trajectories for the droplets which undergo a limit cycle. As we can notice, the area of the limit cycles is larger in

the region surrounding the growing droplet (indicate with GD in Fig. 5.9), and becomes progressively smaller as we increase the distance from this droplet.

As we can notice, the droplets that show this kind of behaviour seem to be homogeneously distributed across the suspension, regardless of the position of the droplet that undergoes the periodic swelling. On the other hand, the area of the limit cycles exponentially decreases with the radial distance from the growing droplet.

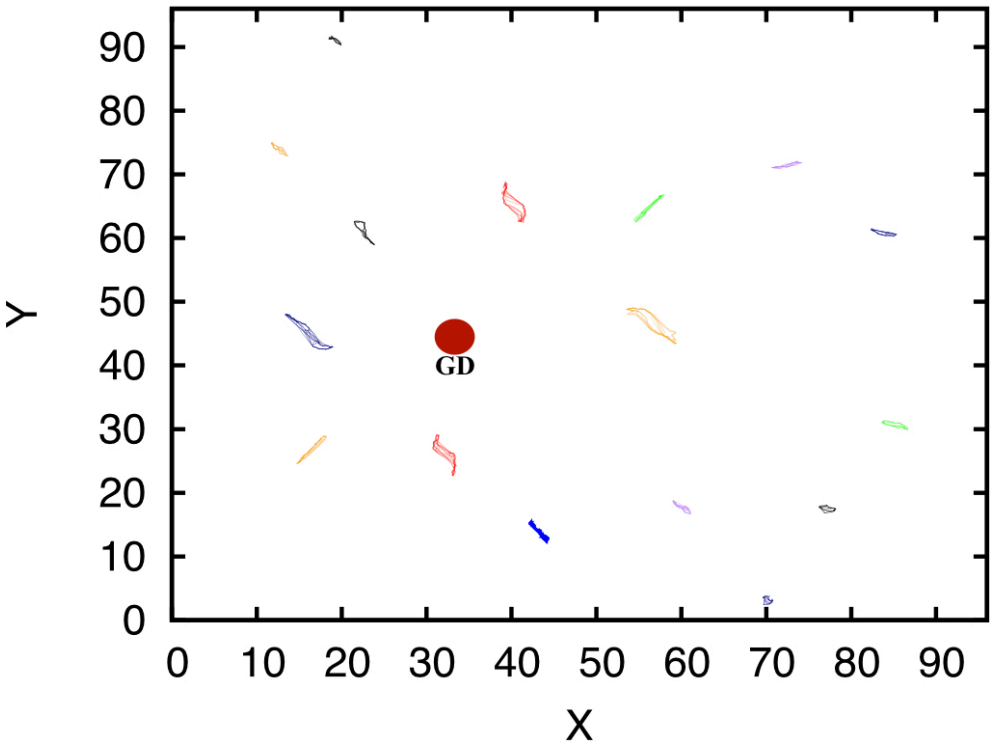


**Figure 5.9** *(x,y) trajectories of all the droplets that show limit cycles. We can notice that they are quite homogeneously spread across the suspension while their area progressively decrease as the distance with the growing droplet is increased. The red circle labelled as GD indicates the position of the growing droplet.*

Another way to quantify the limit cycle behaviour that we observe in our simulations is to introduce a parameter $L$ defined as $L_i(t) = \vec{r}_i(t) - \vec{r}_i(2T - t)$, where $i$ labels the droplets within the suspension. In particular, if we calculate

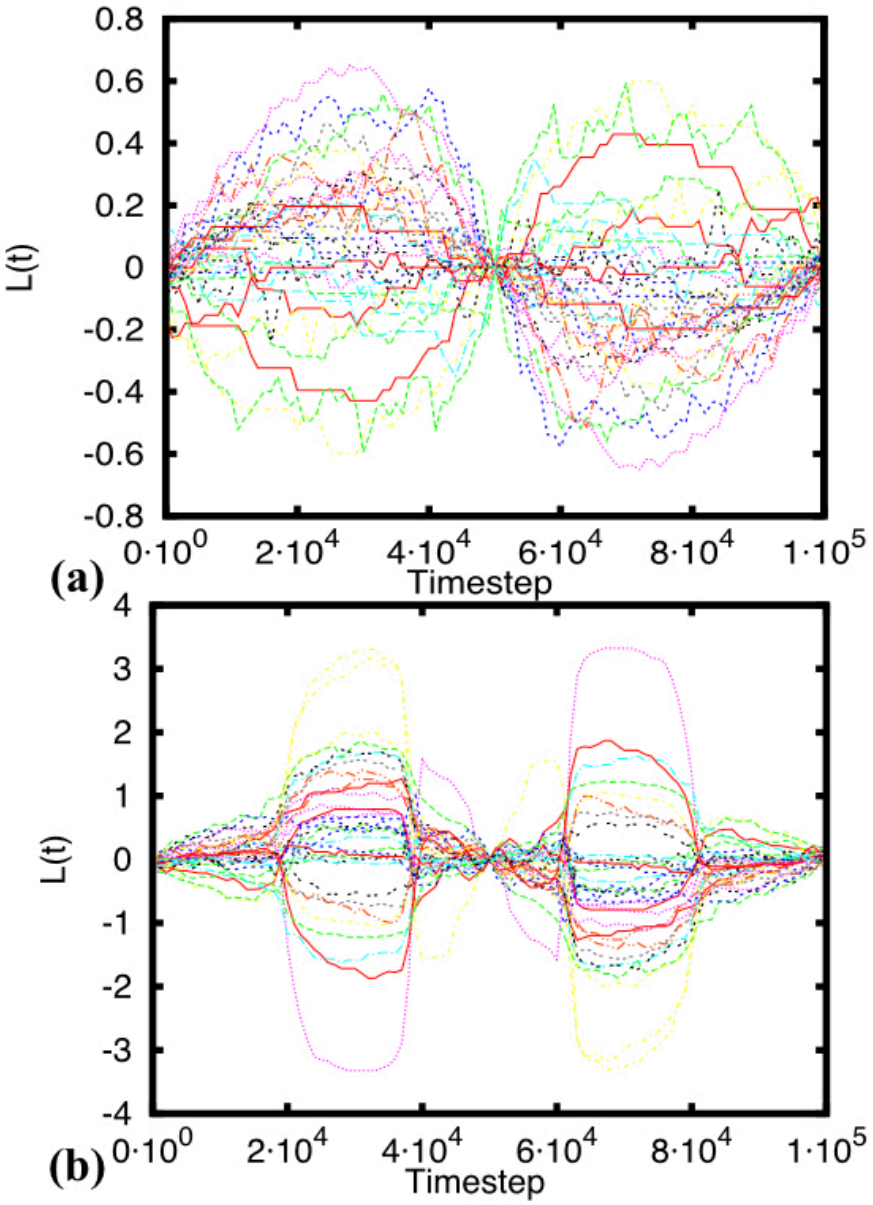


**Figure 5.10** *(a) Plot of $L(t)$ over time for all the droplets in the suspension (except the growing one) for the case of growth rate $\alpha = 2 \cdot 10^{-5}$ and deformation period $T = 50000$. As we can see each curve of $L(t)$, referring to a different droplet, oscillates between 0, $L(T/2)$ and $-L(T/2)$, presenting a symmetric behaviour.* ***(b)*** *Same as* ***(a)*** *for the case of growth rate $\alpha = 2.5 \cdot 10^{-5}$ and deformation period $T = 50000$.*

this quantity for a droplet while it is undergoing a limit cycle, we would expect:

$$\begin{cases} L(0) = L(T) = 0 \\ L(T/2) \neq 0 \end{cases} \tag{5.3}$$

We therefore expect this quantity to grow from 0, as time approaches $t = T$, where it will reach its maximum, and consequently decrease while time approaches $2T$, where it will again reach the value of 0. The maximum reached for $L(T)$ represents the maximum distance the droplet travels with respect to its original position, when the central growing droplet has reached its maximum size. After time $T$, the central droplet will start deflating, letting the surrounding droplet reach their original position, i.e. L(t) comes back to 0. An example of a limit cycle behaviour is shown in Fig. 5.10, where the quantity $L(t)$ plotted for each droplet of our suspension displays the expected oscillation between 0 and its maximum value $L(T/2)$.

The limit cycle behaviour is demonstrated by the fact that $L(t)$ is 0 for and integer multiple of the period $t = T$. Moreover, this function shows a marked time symmetry which indicates that the position of the droplet at a time $T$ and $2T$ are, on average, on a similar distance in modulus from the original position, though in opposite directions.

On the other hand, the quantity $L(t)$ gives insights also into the irreversible scenario, as shown in Fig. 5.11. Here we plot the function $L(t)$ for each droplet in our suspension for an irreversible case, where the droplet position after any integer multiple of the period $T$ is not the same. In terms of the function $L(t)$, this means that its value will follow

$$L(t) \neq 0 \quad \forall \quad t \neq T. \tag{5.4}$$

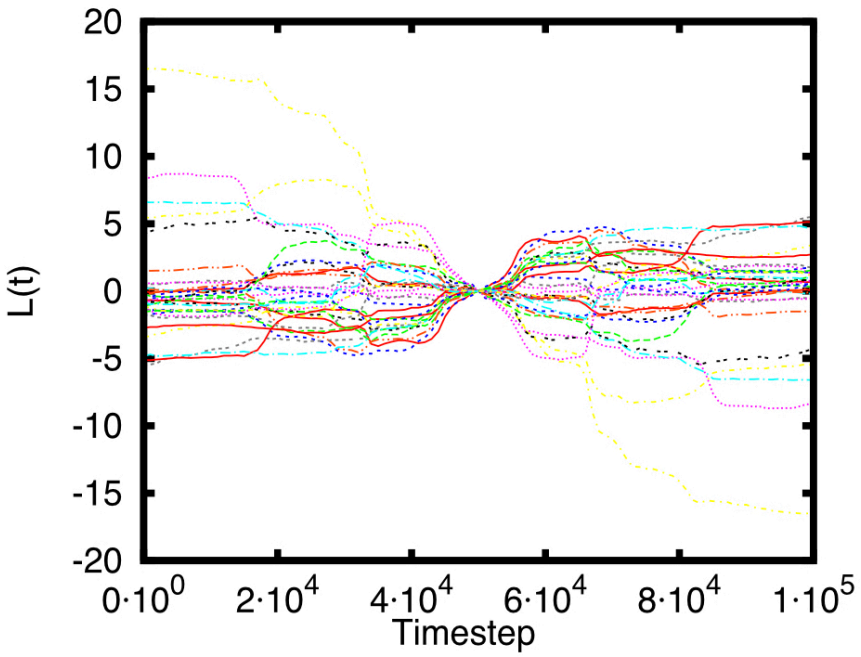


**Figure 5.11** *Plot of $L(t)$ over time for all the droplet in the suspension (except the growing one for the case of growth rate $\alpha = 3 \cdot 10^{-5}$ and deformation period $T = 50000$.) As we can see, the droplets are not undergoing a limit cycle. Indeed, $L(t)$ is not 0 for each integer multiple of the period $T$.*

## 5.2 Oscillatory shear

In light of the results discussed in the previous section, it is interesting to test whether a different kind of imposed external deformation on our system causes the same reversible-to-irreversible transition in the suspension behaviour. To this end, in this section we describe the results obtained after performing simulations where the deformation applied to our deformable droplet suspension derives from a periodic oscillatory shear.

In a similar fashion to the growing droplet scenario, here we perform simulations where we systematically vary the imposed shear amplitude as well as the period of the oscillatory shear. In this way, we are able to define the set of parameters that guarantee reversible behaviour for our suspension, leading us to draw a reversibility phase diagram for this type of deformation. In agreement with the results discussed in the previous section, a transition between a reversible and an irreversible phase is detected and found to depend on the amount of imposed shear.

### 5.2.1 The model

In order to simulate our droplet suspension under oscillatory shear we again use the same phase field framework described in Chapter 3. As previously described, a Hybrid Lattice Boltzmann method is implemented to investigate the dynamics of a two-dimensional suspension of soft, non-coalescing droplets this time perturbed by a periodical horizontal shear of the two walls sandwiching the suspension. The free energy density (3.1), the hydrodynamic implementation of the Lattice Boltzmann method as well as the Cahn-Hilliard dynamical evolution of the droplets' fields (3.2) discussed in Chapter 3 are also used in this section. In order to mimic a planar shear, we apply the velocity $\pm v(t)$ to the upper and lower plates which enclose our suspension such as

$$\begin{cases} v(t)_{up} = + \quad \gamma_0 \sin(\omega t) \\ v(t)_{bt} = - \quad \gamma_0 \sin(\omega t) \end{cases} \tag{5.5}$$

where $\omega = \frac{2\pi}{T}$ is the frequency, with period $T$, and the velocity subscripts denote the upper and bottom plate, respectively. In this way, the two boundary walls

simultaneously move in opposite directions, applying a planar oscillating shear to our suspension.

### 5.2.2 Irreversibility transition

In line with the approach we followed in the section dedicated to the growing droplet scenario (5.1), we now test the reversibility properties of our system when subjected to periodic deformation, this time provided by oscillatory shear. To this end, we perform simulations where we systematically vary the period $T$ of the oscillation as well as its amplitude $\gamma_0$. Tracking the droplet positions and comparing them after a period of oscillation, we are able to distinguish the cases where the droplets configuration across the suspension is identical before and after a period $T$, and cases where such comparison gives the opposite result.

In analogy with Figure 5.1 in section 5.1, in Figure 5.12 we present snapshots of our simulations in order to provide a qualitative understanding of the way we distinguish the reversible from irreversible cases. Figure 5.12**(a)** and **(b)**, taken at different time steps of our simulation, show the case where the droplets' configuration across the suspension before and after a period of oscillation is identical, i.e. a reversible case. Indeed, the period $T$ represents the time the plates take to move towards one direction and then reverse their motion until they reach their original position. In this scenario, the droplets in the suspension enclosed by the plates move according to the imposed shear and, in case of a reversible behaviour, after the shear is reversed they should reach their original position. On the other hand, Figure 5.12**(c)** and **(d)** show snapshots of our simulations where the oscillation amplitude is much higher than in the previous case. As we can see, here the droplet configuration across the suspension before and after the oscillation period $T$ is markedly different, i.e our system shows irreversible behaviour.

A more quantitative interpretation of the observed reversible-to-irreversible transition can be achieved by calculating the average droplet displacement after a period of oscillation T given by the quantity $d = \langle \mid \vec{r}(t) - \vec{r}(t + 2T) \mid \rangle$, where $\vec{r}$ denotes the droplet position, and the average is taken over time and over the all the droplets in our suspension. Intuitively, we would expect $d_{rev} \sim 0$ in the reversible scenario, where each droplet after a period of oscillation comes back to its original position. On the other hand, the irreversible behaviour implies that

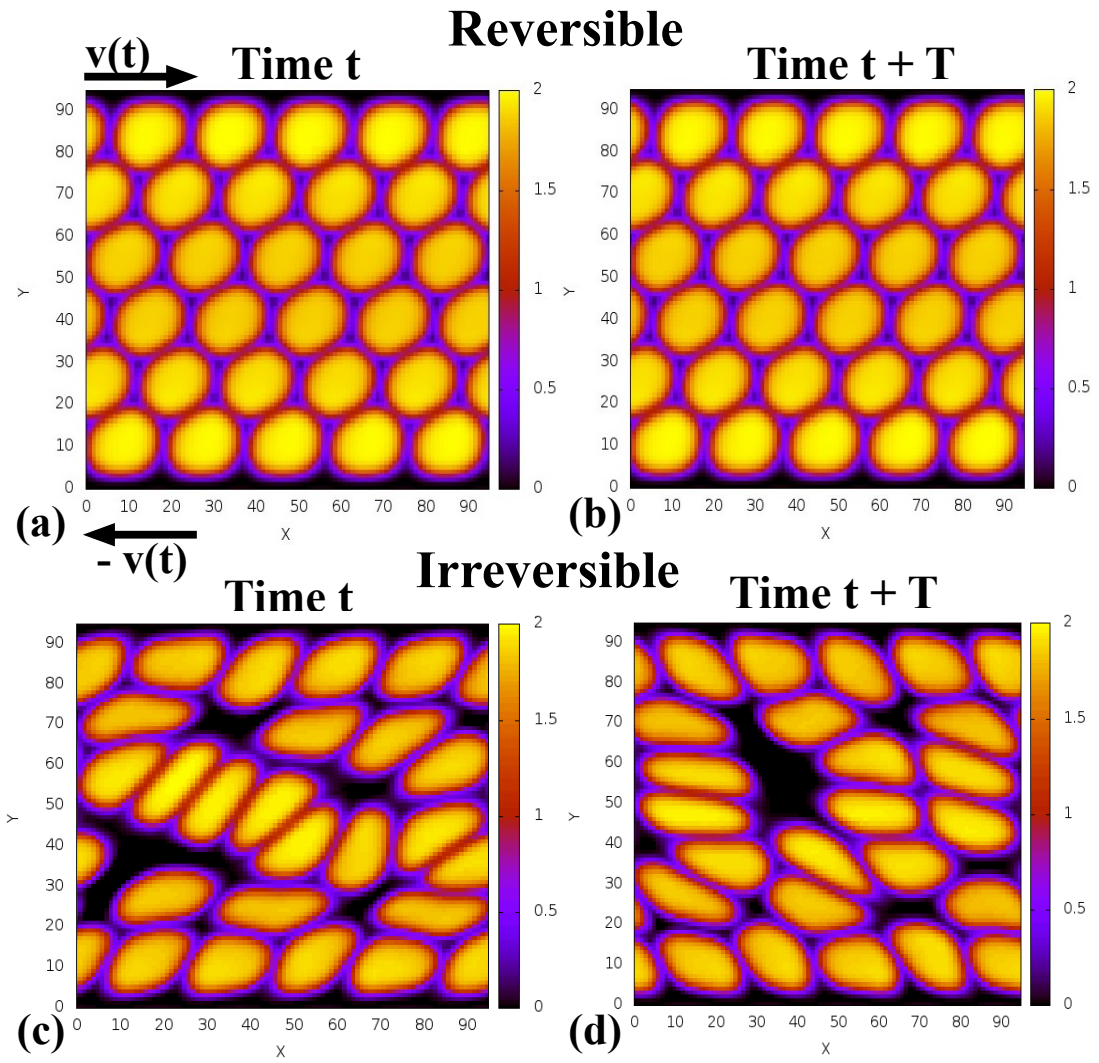


**Figure 5.12** *(a) Snapshot of a simulations at a timestep t where the suspension is subjected to an oscillatory shear with amplitude* $\gamma_0 = 10^{-3}$*. The latter is achieved by fixing a velocity* $v(t)$ *to the upper plate and* $-v(t)$ *to the bottom one as shown by the arrows.* ***(b)*** *Same as* ***(a)*** *but at timestep* $t' = t + T$*, i.e. after the shear has been reversed and the suspension droplet configuration should be identical to the time before the shear was applied. Comparing* ***(a)*** *and* ***(b)*** *we can observe that they are qualitatively identical, i.e. our suspension shows a reversible behaviour.* ***(c)*** *Snapshot of a simulations at a timestep t, where the suspension is subjected to oscillatory shear as in* ***(a)****, but with shear amplitude* $\gamma_0 = 5 \cdot 10^{-2}$*.* ***(d)*** *Same as* ***(c)*** *but at a time* $t' = t + T$*, i.e. after the shear has been reversed. Comparing* ***(c)*** *and* ***(d)*** *we can notice that the overall droplets configuration shows significant difference between the two snapshots, indicating that our suspension is presenting an irreversible behaviour.*

after each oscillation period, some or all droplets within the suspension will find

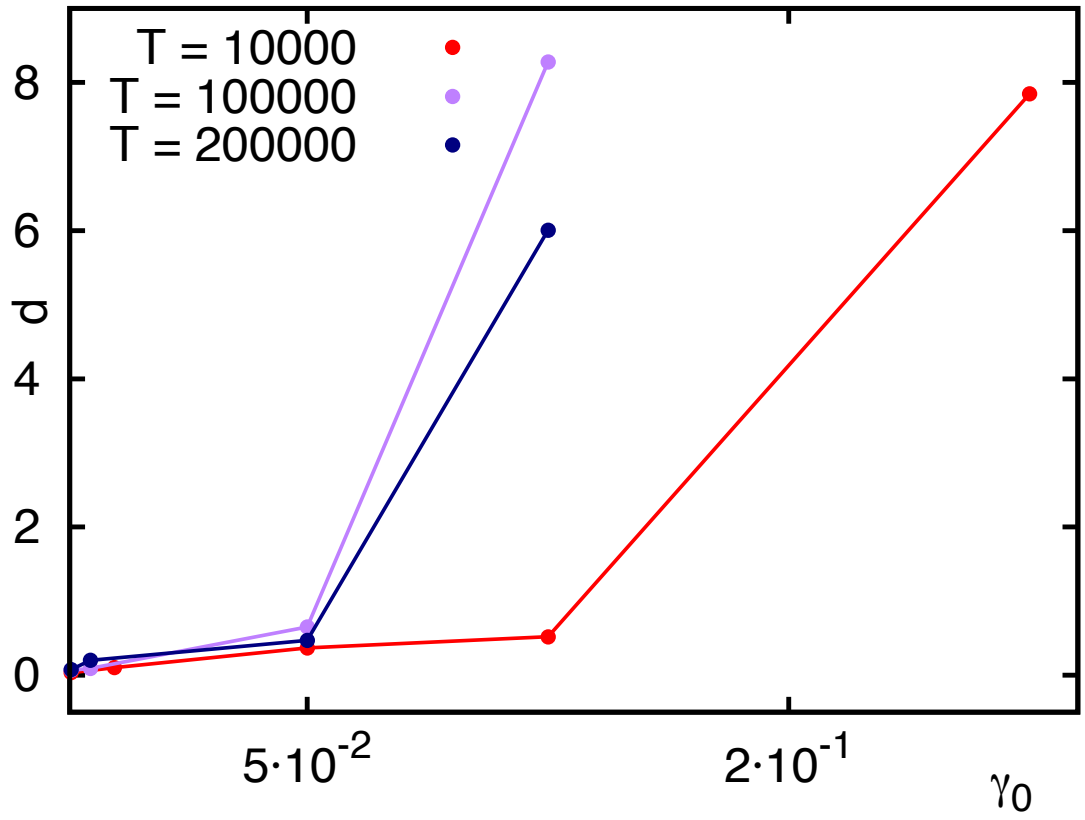


**Figure 5.13** *Average of the droplets displacements after each period of oscillation as a function of the oscillation amplitude $\gamma_0$. The three curves refer to different values of the oscillation period $T$. As we can notice, $d = \langle \mid \vec{r}(t) - \vec{r}(t+2T) \mid \rangle$ (expressed in lattice units) sees a sharp increase towards higher values, signalling a transition towards an irreversible phase.*

themselves in a different position with respect to their original one, leading to $d_{irr} \gg d_{rev}$.

Considering this quantity as a function of the oscillation amplitude $\gamma_0$, we therefore expect to observe a discontinuity, or a sudden jump towards higher values corresponding to the transition between the reversible and irreversible scenario. In Figure 5.13 we can observe the trend of $d$ as a function of $\gamma_0$ for three different value of the oscillation period $T$. Considering the difference in the values of $d$ between each pair of points in Fig. 5.13, we can define a threshold value for the oscillation amplitude corresponding to the larger increase of each curve (last point of each curve). We note that if we had considered higher values of $\gamma_0$ (not computationally accessible), we could have found even bigger increase in the points of the curve. As we can notice, this threshold is progressively shifted towards lower values as the oscillation period $T$ is increased.

We can therefore conclude that a system subjected to an oscillatory shear with shorter period $T$, needs a higher value of the oscillation amplitude $\gamma_0$ in order to undergo a transition towards the irreversible phase.

### 5.2.3 Phase diagrams

Having performed simulations for various values of oscillation amplitude and period, we are now able to draw a phase diagram which distinguish the reversible from the irreversible behaviour of our system.

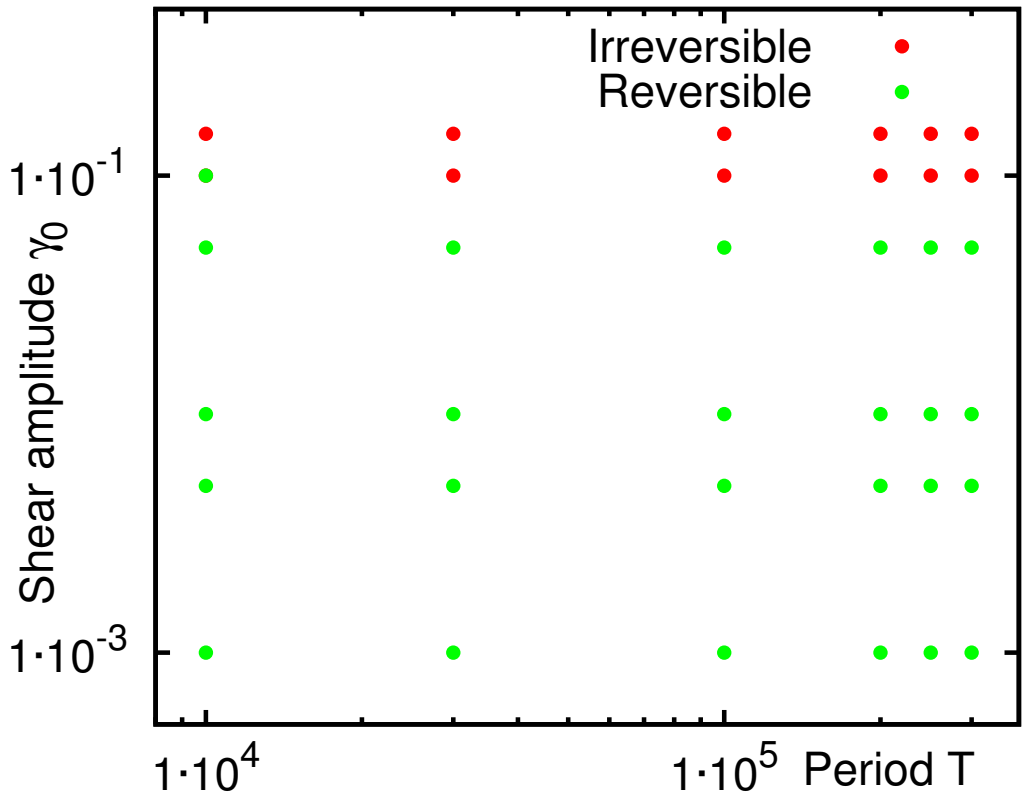


**Figure 5.14** *Reversibility phase diagram for a suspension under oscillatory shear. The green dots represent reversible cases, i.e. the droplets positions are identical after each period of the oscillation, while the red ones indicate an irreversible behaviour, i.e. the droplets configuration changes after each period of the oscillation.*

To this end, for each choice of the simulation parameters $\gamma_0$ and $T$, we compare

the different snapshot of our system taken at different timesteps separated by a time $T$ corresponding to the period of the oscillation (as shown in Fig. 5.12). This qualitative comparison, supported by the analysis of the trend of $d$ as a function of the oscillation amplitude leads us to distinguish the suspension behaviour: if the overall droplet configuration is identical before and after each period of oscillation, we label the case as "reversible" (green dots in Fig. 5.14); on the other hand, if we can spot a difference in the droplets position within the same time interval, we label the case as "irreversible" (red dots in Fig. 5.14).

The corresponding reversibility phase diagram is shown in Figure 5.14, where red and green represent the irreversible and reversible phase, respectively. As we can notice, increasing the value of the period $T$ of the oscillation or its amplitude $\gamma_0$ leads towards the irreversible part of the phase diagram. We can therefore conclude that the reversible-to-irreversible transition we observe, is tuned by the amount of imposed deformation on the suspension as well as its period.

## 5.3 Concluding remarks

In summary, in this chapter we tested the reversibility properties of our two dimensional suspension of non coalescing deformable droplets when subjected to a periodic deformation. The latter was obtained through two different set of simulations modelling a periodic area inflation and deflation of a certain droplet within the suspension and an external oscillatory shear, respectively.

In both scenarios, the trajectories of all the droplets are carefully tracked in order to be able to compare their position before and after a period of deformation. This comparison enables us to distinguish the cases where the overall configuration of the droplets across the suspension is identical before and after the deformation has occurred, and the cases where the droplets do not come back to their original positions after each deformation period. Performing simulations where we systematically varied the parameters which tune the period and amount of both types of deformation imposed on our system, we were able to obtain a reversibility phase diagram which signals a transition from a reversible behaviour towards an irreversible one.

Moreover, for the growing droplet scenario, we analysed more in detail the area in the phase diagram corresponding to the reversible behaviour. In this case, while the central droplet is periodically inflated and deflated, we analysed the dynamics of its neighbouring ones. Given that our suspension presents here a reversible behaviour, all the droplets reach their original position after each period of inflation/deflation of the central one. Nevertheless, we observed that most of the droplets within our suspension perform a repeated limit cycle, i.e. if we draw the paths that those droplets follow in order to get to their new position, which allows the growing droplet to reach its maximum size, and to consequently come back to their original ones, we can notice that such paths are closed loops. Indeed, after having reached their new position, instead of tracking their steps back, those droplets choose a different path to get to their original one after each period of deformation. Moreover, we showed that such limit cycles are identically repeated for all the periods of inflation/deflation we impose.

On the other hand, such limit cycles were not observed in the case of the oscillatory shear. Here, in the reversible cases, the symmetry of the strain imposed on our suspension through the parallel boundary walls prevents the droplets from moving along the $y$ axes across the different lines forming the suspension.

Therefore, each droplet, being able only to slide between its upper and lower neighbours, is not allowed to perform a limit cycle.

# Chapter 6

# Conclusions

We now present an overview of the results achieved in this thesis, discussing the two types of transition we distinguished with our simulations of a deformable droplet suspension: the Hard-Soft transition and the Irreversibility transition.

*Discontinuous Shear Thinning: Hard-Soft transition* – As previously discussed, the flow of colloidal suspensions can be characterised by distinctively non-trivial properties: for instance, a suspension of colloidal spheres in water first exhibits shear thinning and then shear thickening as the external forcing is increased [95] [10]. In recent years, experimental and theoretical studies have discovered and analysed the interesting property that, for dense suspensions, the shear thickening can be discontinuous. This behaviour is interpreted as a clear mark of a transition between a lubricated-dominated and a frictional flow regime [23].

In Chapter 3 of this thesis we investigated the rheological properties of our deformable droplet suspension when subjected to a pressure driven flow. In particular, we have shown that the rheology of a suspension of deformable, non-coalescing droplets, under pressure-driven flow, entails discontinuous shear thinning behaviour. We interpret this discontinuity as a non-equilibrium transition between a hard regime, where droplets tend to resist deformation and flow slowly, and a soft regime, where droplets are more susceptible to deformation and flow much more readily. Moreover, close to the transition, we find sustained oscillations in both the droplets and the underlying fluid velocities, which are reminiscent of those previously reported for hard colloidal systems close to the glass transition [75]. For both cases, it is tempting to speculate that oscillations arise due to proximity to a discontinuous transition.

In the future, it would be interesting to be able to observe discontinuous shear thinning experimentally, by studying the rheology of suspensions of non-coalescing droplets. Other than the great satisfaction I would personally feel in case of experimental observation of *my* discontinuous shear thinning, I would imagine that this discovery could be exploited in designing devices in the context where a reduction in viscosity is pivotal for the system flow. Indeed, the possibility of predicting the threshold of applied pressure difference causing a substantial drop in the material viscosity could be exploited in tuning the mechanical specifications of microfluidics devices.

*The role of deformability* – Our interest in the property of deformability of our droplets arises from the fact that, often, in colloidal fluids, the disperse particles are not hard, but soft and deformable. This kind of emulsion sees broad applications in industry and medicine, including waste treatment, food processing and pharmaceutical manufacturing. Examples can be found in the fat droplets floating in milk, or red blood cells flowing in blood: all these can deform under flow, or when subjected to a mechanical stress. On the other hand, while fluids composed of hard spheres have been extensively studied in the past, providing the basis of our understanding of the glass transition and soft glassy rheology, comparatively less is known about their soft and deformable counterparts. Nonetheless, there is evidence suggesting that the physics of soft suspensions is both highly interesting and important in applications [62–65].

As previously mentioned, in Chapter 3 we showed that emulsion rheology displays a discontinuous shear thinning behaviour, viewed as a non-equilibrium transition between "hard" and "soft" regimes. Having pinpointed the origin of this rich behaviour in the droplets' ability to deform, in Chapter 4 we characterised the suspension rheological properties as a function of the droplets' surface tension. Indeed, the latter can be tuned in our simulations in order to design more or less deformable droplets. Our results show that the observed hard-soft transition progressively shifts towards higher values of the applied pressure difference as we increase the droplet surface tension. In other words, a more rigid system (high values of surface tension $K$), will need a higher threshold value of the applied pressure difference to trigger its transition towards the soft phase.

Moreover, we show that the rheological properties of our suspension can also be characterized by its Capillary number $Ca$, defined as in (4.1). This parameter, which captures the interplay between the droplet elastic properties and the overall system flow, can be used to scale the system viscosity curves. Indeed, when

plotted against the Capillary number, all the viscosity curves referring to different fixed values of surface tension, collapsed onto the same curve, showing how the Capillary number captures the relevant mechanism controlling the suspension viscosity. This is important as the master curve allows simple predictions of flow curves at different system size $L$, applied pressure difference $\Delta P$ and surface tension (provided that the suspension area fraction $\Phi$ is kept constant).

Finally, we test the system properties through simulations where we mimic an active microrheological experiment, where a single droplet is dragged across the overall domain. Systematically varying the value of the body-force applied on the target droplet, we observe a discontinuous behaviour in the velocities of both the probe droplet and its neighbours. In agreement with the discontinuous shear thinning observed in Chapters 3 and 4, this velocity discontinuity is interpreted as another mark of the hard-soft transition that our suspension is undergoing. Similarly to the case of pressure-driven macroscopic flow, the discontinuity in the probe velocity occurs for progressively larger values of the applied forcing as we increase the value of the droplet surface tension. In other words, as our suspension becomes progressively more rigid and overall less deformable, we will need an increasingly higher forcing in order to observe the probe droplet easily flow across the suspension.

We can therefore conclude that the suspension deformability, characterised by the droplets surface tension, the overall suspension area fraction and its Capillary number, play a pivotal role in defining the rheological and flow properties of a droplet suspension. Indeed, both in the context of pressure-driven flow and of active micro-rheology, the suspension ability to deform can tune the threshold of the forcing needed in order to trigger the transition from the hard phase, where the droplets are more rigid, towards a soft one, characterised by droplets which are significantly more susceptible to deformation.

*Irreversibility Transition* – As it is well known, some physical systems are described by laws and equations that are time reversible. Examples reversible systems are observed on the Newtonian flows at low Reynolds number, as demonstrated by Taylor's famous Couette flow experiment. Moreover, the reversible creeping flow equations also regulate the low Reynolds number dynamics of a suspension of non-Brownian particles. Despite this evidence, experience tells us that most of these reversible systems actually present a transition towards an irreversible regime, where chaotic or non predictable behaviour replaces the deterministic dynamics [87–92]. The origin of this irregular

motion lies in the interactions between the particles and the surrounding fluid, producing remarkable effects on the overall suspension behaviour.

Given this background, in Chapter 5 we tested the reversibility properties of our two dimensional suspension of deformable non coalescing droplets when subjected to periodical deformation. The latter is obtained via two different sets of simulations, modelling a periodical area inflation and deflation of a certain droplet within the suspension and an external oscillatory shear, respectively. In both scenarios, we carefully tracked all droplets trajectories over time in order to be able to compare their positions before and after a period of the imposed deformation. This comparison enables us to distinguish the cases where the overall distribution of the droplets across the suspension is identical before and after the deformation has occurred, from the cases where the droplets do not come back to their original positions after each deformation period. Moreover, in our simulations we systematically varied the period and amount of both types of deformation imposed to our system, enabling us to obtain a phase diagram which signals the transition from a reversible behaviour towards an irreversible one. Our reversibility phase diagrams contribute to the understanding of the underlying mechanisms regulating this fascinating transition, where, somehow inexplicably, time reversibilty fails. Indeed, since reveresible states are observed for high values of the suspension area fraction, we can, for instance, state that the reversibility is not (or at least not only) due to collisions avoidance between the droplets, as for concentrated suspensions this is not a possible scenario.

For the growing droplet scenario, we analysed more in detail the area of the phase diagram corresponding to the reversible behaviour. Tracking the droplets trajectories while inflation/deflation of the central one, we observed that most of the droplets within our suspension perform repeated limit cycles, i.e. close loops in their trajectories that are identically repeated every period of inflation/deflation of the growing droplet.

Theoretically, the results of this thesis prompt new questions. In the future, it would be of interest to develop a theoretical model which predicts the discontinuous shear thinning observed in our simulations, in order to contribute to our general understanding of soft rheology. At the same time it would be interesting to be able to recreate the discontinuous shear thinning in the lab, by studying the rheology of suspension of non coalescing droplets. Moreover, it would be useful to characterise experimentally the dependence of the hard-soft transition on the droplets surface tension, as well as test whether our deformable

droplets model could be actually used in order to predict the behaviour of red blood cells.

Furthermore, a deep theoretical understanding of what exactly regulates the transition from a reversible behaviour towards an irreversible one is still lacking and it would desirable to achieve it. Indeed, a theoretical framework describing the reversible-to-irreversible transition would contribute to our understanding of the link connecting the microscopic structural properties of a material to its macroscopic behaviour.

# Bibliography


[1] B. M. Guy. *The physics of the flow of concentrated suspensions*. PhD Thesis, 2016.

[2] X. Liang J. Xu C. Lee Q. Liang P. Tao F. Yu, Y. Chen and T. Deng. Dispersion stability of thermal nanofluids. *Progress in Natural Science: Materials International*, 27(5):531 – 542, 2017.

[3] W.J. Norman and J.F. Brady. Shear thickening in colloidal dispersions. *Physics Today*, 62(10):27–32, 2009.

[4] Z. Cheng J. Zhu P. M. Chaikin J. H. Dunsmuir S.E. Phan, W. B. Russel and R. H. Ottewill. Phase transition, equation of state, and limiting shear viscosities of hard sphere dispersions. *Physical Review E*, 54(6):6633, 1996.

[5] C. Neinhuis R. Hensel and C. Werner. The springtail cuticle as a blueprint for omniphobic surfaces. *Chem. Soc. Rev.*, 45:323–341, 2016.

[6] A. C. Rowat D. Lee J. J. Agresti A. S. Utada L. Chu J. Kim A. Fernandez-Nieves C. J. Martinez R. K. Shah, H. C. Shum and D. A. Weitz. Designer emulsions using microfluidics. *Materials Today*, 11(4):18 – 27, 2008.

[7] R. K. Pathria. *Statistical Mechanics*. Butterworth-Heinemann, 1996.

[8] P. G. Debenedetti. *Metastable liquids: concepts and principles*. Princeton University Press, 1996.

[9] S. R. Elliott. *Physics of amorphous materials*. Longman Group, 1983.

[10] R. A. L. Jones. *Soft Condensed Matter*. Oxford University Press, 2002.

[11] J. N. Israelachvili. *Intermolecular and surface forces: revised third edition*. Academic press, 2011.

[12] J. T. G. Verwey and E. J. W. Overbeek. *Theory of the stability of lyophobic colloids*. Courier Corporation, 1999.

[13] M. Rubinstein and R. H. Colby. *Polymer physics*. Oxford University press, 2003.

[14] J. Klein. Shear, friction, and lubrication forces between polymer-bearing surfaces. *Annual review of materials science*, 26:581–612, 1996.

[15] L. Cipelletti and E. R. Weeks. Glassy dynamics and dynamical heterogeneity in colloids. *Dynamical Heterogeneities in Glasses,Colloids, and Granular Media*, 2011.

[16] A. Einstein. Eine neue bestimmung der molekldimensionen. *Annalen der Physik*, 19:289–306, 1906.

[17] R. G. Larson. *The structure and Rheolgy of Complex Fluids*. Oxford University Press, 1999.

[18] J. Van der Werff and C. De Kruif. Hard-sphere colloidal dispersions: The scaling of rheological properties with particle size, volume fraction, and shear rate. *Journal of Rheology*, 33(3):421–454, 1989.

[19] D. Vlassopoulos G. Petekidis and P. Pusey. Yielding and flow of sheared colloidal glasses. *Journal of Physics: Condensed Matter*, 16(38):S3955, 2004.

[20] J. Mewis and N. J. Wagner. *Colloidal suspension rheology*. Cambridge University Press, 2012.

[21] E. R. Weeks W. C. Poon and C. P. Royall. On measuring colloidal volume fractions. *Soft Matter*, 8(1):21–30, 2012.

[22] G. Bossis and J. F. Brady. The rheology of brownian suspensions. *J. Chem. Phys.*, 91, 1989.

[23] M. Wyart and M. E. Cates. Discontinuous shear thickening without inertia in dense non-brownian suspensions. *Phys. Rev. Lett.*, 112:098302, 2014.

[24] R. Seto R. Mari J. F. Morris and M. M. Denn. Discontinuous shear thickening of frictional hard-sphere suspensions. *Phys. Rev. Lett.*, 111:218301, Nov 2013.

[25] J. F. Morris R. Mari, R. Seto and M. M. Denn. Shear thickening, frictionless and frictional rheologies in non-brownian suspensions. *Journal of Rheology*, 58(6):1693–1724, 2014.

[26] W. C. K. Guy B. M. Hermes, M. Poon. Towards a unified description of the rheology of hard-particle suspensions. *Phys. Rev. Lett.*, 115:088304, Aug 2015.

[27] F. Brochard-Wyart P.G. de Gennes and D. Quéré. *Capillarity and Wetting Phenomena*. Springer-Verlag, 2003.

[28] E. Villarmeaux. Fragmentation. *Annu. Rev. Fluid Mech.*, 39:419–446, 2007.

[29] J.R.Grace R. Clift and M.E.Weber. *Bubbles, Drops and Particles*. Academic Press Inc, 1978.

[30] F. Blanchette and T.P. Bigioni. Partial coalescence of drops at liquid interfaces. *Nat. Phys.*, 2:254–257, 2006.

[31] E. Villermaux and B. Bossa. Single-drop fragmentation determines size distribution of raindrops. *Nat. Phys.*, 5:697–702, 2009.

[32] A. M. Puertas A. F. Nieves. *Fluids, Colloids and Soft Materials: An introduction to Soft Matter Physics*. John Wiley & Sons, Inc, 2016.

[33] R. Armstrong R. B. Bird and O. Hassager. Dynamics of polymeric liquids. *Fluid mechanics*, 1.

[34] JA. Lodge. *Elastic liquids*. Academic Press, 1964.

[35] L.D. Landau and E.M. Lifshitz. *Theory of elasticity*. Pergamon Press, 1970.

[36] Y. Forterre B. Andreotti and O. Pouliquen. *Granular media: between fluid and solid*. Cambridge University Press, 2013.

[37] G. Mase. *Schaums outline of theory and problems of continuum mechanics*. McGraw-Hill, 1970.

[38] W. R. Schowalter W. B. Russel, D. A. Saville. *Colloidal Dispersions*. Cambridge Monographs on Mechanics. Cambridge University Press, 1990.

[39] W. C. Poon C. P. Royall and E. R. Weeks. In search of colloidal hard spheres. *Soft Matter*, 9(1):17–27, 2013.

[40] W. R. Osborn M. R. Swift, E. Orlandini and J. M. Yeomans. Lattice boltzmann simulations of liquid-gas and binary fluid systems. *Phys. Rev. E*, 54:5041–5052, 1996.

[41] E. Orlandini C. Denniston and J. M. Yeomans. Lattice boltzmann simulations of liquid crystal hydrodynamics. *Phys. Rev. E*, 63:056702, 2001.

[42] W. R. Osborn M. R. Swift and J. M. Yeomans. Lattice boltzmann simulation of nonideal fluids. *Phys. Rev. Lett.*, 75:830–833, 1995.

[43] I. Pagonabarraga A.J. Wagner M. E. Cates. Binary fluid demixing: the crossover region. *J. Stat. Phys.*, 107:39, 2002.

[44] A. Tiribocchi, N. Stella, G. Gonnella, and A. Lamura. Hybrid lattice boltzmann model for binary fluid mixtures. *Phys. Rev. E*, 80:026701, 2009.

[45] J.M. Buick and C. A. Greated. Gravity in a lattice boltzmann model. *Phys. Rev E*, 61, 2000.

[46] N. S. Martys and H. Chen. Simulation of multicomponent fluids in complex three-dimensional geometries by the lattice boltzmann method. *Phys. Rev. E*, 53, 1996.

[47] B. Hasslacher P. Lallemand U. Frisch, D. d'Humieres and Y. Pomeau. Lattice gas hydrodynamics in two and three dimensions. *Complex Syst.*, 1, 1987.

[48] E. Tjhung, A. Tiribocchi, D. Marenduzzo, and M. E. Cates. A minimal physical model captures the shapes of crawling cells. *Nat. Comm.*, 6:5420, 2015.

[49] M. Fuchs C. B. Holmes and M. E. Cates. Jamming transitions in a schematic model of suspension rheology. *Europhysics Letters*, 63(2):240–246, 2003. ISSN 0295-5075.

[50] P. Sollich, F. Lequeux, P. Hébraud, and M. E. Cates. Rheology of soft glassy materials. *Phys. Rev. Lett.*, 78:2020–2023, 1997.

[51] N. Y. C. Lin, B. M. Guy, M. Hermes, C. Ness, J. Sun, W. C. K. Poon, and I. Cohen. Hydrodynamic and contact contributions to continuous shear thickening in colloidal suspensions. *Phys. Rev. Lett.*, 115:228304, 2015.

[52] G. R. Lazaro, A. Hernandez-Machado, and I. Pagonabarraga. Rheology of red blood cells under flow in highly confined microchannels: I. effect of elasticity. *Soft Matter*, 10:7195–7206, 2014.

[53] M. Fuchs C. B. Holmes, M. E. Cates and P. Sollich. Glass transitions and shear thickening suspension rheology. *J. Rheol.*, 49(1):237 – 269, 2005.

[54] G. L. Hunter and E. R. Weeks. The physics of the colloidal glass transition. *Reports on Progress in Physics*, 75(6):066501.

[55] P. N. Pusey, E. Zaccarelli, C. Valeriani, E. Sanz, W. C. K. Poon, and M. E. Cates. Hard spheres: crystallization and glass formation. *Phil. Trans. R. Soc. A*, 367:4993–5011, 2009.

[56] S. M. Fielding, M. E. Cates, and P. Sollich. Shear banding, aging and noise dynamics in soft glassy materials. *Soft Matter*, 5:2378–2382, 2009.

[57] H. Zhou and C. Pozrikidis. Pressure-driven flow of suspension of liquid drops. *Phys. Fluids*, 6:80, 1994.

[58] A. Nourbakhsh, S. Mortazavi, and Y. Afshar. Three-dimensional numerical simulation of drops suspended in poiseuille flow at non-zero reynolds numbers. *Phys. Fluids*, 23:123303, 2011.

[59] M. Loewenberg and E. J. Hinch. Numerical simulation of a concentrated emulsion in shear flow. *J. Fluid Mech.*, 321:395–419, 1996.

[60] A. Z. Zinchenko and R. H. Davis. Extensional and shear flows, and general rheology of concentrated emulsions of deformable drops. *J. Fluid Mech.*, 779: 197–244, 2015.

[61] A. Z. Zinchenko and R. H. Davis. General rheology of highly concentrated emulsions with insoluble surfactant. *J. Fluid Mech.*, 816:661–704, 2017.

[62] E. M. Schotz, M. Lanio, J. A. Talbot, and M. L. Manning. Glassy dynamics in three-dimensional embryonic tissues. *J. Roy. Soc. Interface*, 10:20130726, 2013.

[63] T. E. Angelini, E. Hannezo, X. Trepat, M. Marquez, J. J. Fredberg, and D. A. Weitz. Glass-like dynamics of collective cell migration. *Proc. Natl. Acad. Sci. USA*, 108:4714–4719, 2011.

[64] C. M. Marchetti D. Bi, X. Yang and L. M. Manning. Motility-driven glass and jamming transitions in biological tissues. *Phys. Rev. X*, 6:021011, 2016.

[65] M. Chiang and D. Marenduzzo. Glass transitions in the cellular potts model. *EPL*, 116(2):28009, 2016.

[66] M. E. Cates, J. Vollmer, A. Wagner, and D. Vollmer. Phase separation in binary fluid mixtures with continuously ramped temperature. 361(1805): 793–807, 2003.

[67] G. Falcucci, S. Chibbaro, S. Succi, X. Shan, and H. Chen. Lattice boltzmann spray-like fluids. *EPL (Europhysics Letters)*, 82(2):24005.

[68] X. Shan and H. Chen. Lattice boltzmann model for simulating flows with multiple phases and components. *Phys. Rev. E*, 47:1815–1819, 1993.

[69] G. Gonnella A. Lamuraa A. Piscitelli. Dynamics of binary mixtures in inhomogeneous temperatures. *Journal of Physics A: Mathematical and Theoretical*, 41(10):105001, 2008.

[70] C. S. O'Hern, L. E. Silbert, A. J. Liu, and S. R. Nagel. Jamming at zero temperature and zero applied stress: The epitome of disorder. *Phys. Rev. E*, 68:011306, 2003.

[71] A. Ikeda, L. Berthier, and P. Sollich. Disentangling glass and jamming physics in the rheology of soft materials. *Soft Matter*, 9:7669–7683, 2013.

[72] P. M. Chaikin S. Phan Z. Cheng, J. Zhu and W. B. Russel. Nature of the divergence in low shear viscosity of colloidal hard-sphere dispersions. *Phys. Rev. E*, 65:041405, 2002.

[73] A. Tiribocchi, M. Da Re, D. Marenduzzo, and E. Orlandini. Shear dynamics of an inverted nematic emulsion. *Soft Matter*, 12:8195–8213, 2016.

[74] N. Yoshinaga. Spontaneous motion and deformation of a self-propelled droplet. *Phys. Rev. E*, 89:012913, 2014.

[75] L. Isa, R. Besseling, A. N. Morozov, and W. C. K. Poon. Velocity oscillations in microfluidic flows of concentrated colloidal suspensions. *Phys. Rev. Lett.*, 102:058302, 2009.

[76] K. W. Desmond and E. R. Weeks. Influence of particle size distribution on random close packing of spheres. *Phys. Rev. E*, 90:022204, 2014.

[77] M. Cloitre, R. Borrega, F. Monti, and L. Leibler. Glassy dynamics and flow properties of soft colloidal pastes. *Phys. Rev. Lett.*, 90:068303, 2003.

[78] L. Mohan, M. Cloitre, and R. T. Bonnecaze. Active microrheology of soft particles. *J. Rheol.*, 58:1465–1482, 2014.

[79] M.W.Rampling O.K.Baskurt, M.Hardeman and H.J.Meiselman. *Handbook of Hemorheology and Hemodynamics*. IOP Press, Amsterdam, Netherlands, 2007.

[80] D. A. Fedosov K. Mller and G. Gompper. Shear-induced platelet margination in a microchannel. *Sci. Rep.*, 4, 2014.

[81] H. Zhao and E. S. G. Shaqfeh. Shear-induced platelet margination in a microchannel. *Phys. Rev. E*, 83:061924, Jun 2011.

[82] D. A. Fedosov, B. Caswell, S. Suresh, and G. E. Karniadakis. Quantifying the biophysical characteristics of plasmodium-falciparum-parasitized red blood cells in microcirculation. *Proceedings of the National Academy of Sciences*, 108(1):35–39, 2011.

[83] L. G. Wilson and W. C. K. Poon. Small-world rheology: an introduction to probe-based active microrheology. *Phys. Chem. Chem. Phys.*, 13:10617–10630, 2011.

[84] T. Gisler and D. A Weitz. Tracer microrheology in complex fluids. *Current Opinion in Colloid and Interface Science*, 3(6):586 – 592, 1998.

[85] E. B. Vadas, H. L. Goldsmith, and S. G. Mason. The microrheology of colloidal dispersions. iii. concentrated emulsions. *Transactions of the Society of Rheology*, 20(3):373–407, 1976.

[86] G.I.Taylor and J. Friedman. Low reynolds number flows (national committee on fluid mechanics films, encyclopedia britannica educational corp., united states.

[87] L.V.A. Breedveld, Henricus T.M. van den Ende, R.J.J. Jongschaap, and J. Mellema. Shear-induced diffusion and rheology of noncolloidal suspensions: time scales and particle displacements. *Journal of chemical physics*, 114(13):5923–5936, 2001.

[88] A. Tripathi V. Breedveld, D. van den Ende and A. Acrivos. The measurement of the shear-induced particle and fluid tracer diffusivities in concentrated suspensions by a novel method. *Journal of Fluid Mechanics*, 375:297318, 1998.

[89] I. E. Zarraga and D. T. Leighton, Jr. Measurement of an unexpectedly large shear-induced self-diffusivity in a dilute suspension of spheres. *Physics of Fluids*, 14:2194–2201, 2002.

[90] D. Leighton and A. Acrivos. The shear-induced migration of particles in concentrated suspensions. *Journal of Fluid Mechanics*, 181:415439, 1987.

[91] A. Sierou and J. F. Brady. Shear-induced self-diffusion in non-colloidal suspensions. *Journal of Fluid Mechanics*, 506:285314, 2004.

[92] M. Marchioro and A. Acrivos. Shear-induced particle diffusivities from numerical simulations. *J. Fluid Mech.*, 443:101–128, 2001.

[93] J. F. Brady A. M. Leshansky D. J. Pine, J. P. Gollub. Chaos and threshold for irreversibility in sheared suspensions. *Nature.*, 438, 2005.

[94] J.P. Gollub L. Corte, P.M. Chaikin and D.J. Pine. Random organization in periodically driven systems. *Nature Physics*, 4:420–424, 2008.

[95] J. N. Israelachvili X. Cheng, J. H. McCoy and Itai I. Cohen. Imaging the microscopic structure of shear thinning and thickening colloidal suspensions. *Science*, 333(6047):1276–1279, 2011.

# List of my Publications


[1] M. Foglino, A. N. Morozov, O. Henrich, and D. Marenduzzo. Flow of deformable droplets: Discontinuous shear thinning and velocity oscillations. *Phys. Rev. Lett.*, 119:208002, Nov 2017.

[2] M. Foglino, A. N. Morozov, and D. Marenduzzo. Rheology and microrheology of deformable droplet suspensions. *Soft Matter*, 14, 9361-9367, Nov 2018.

[3] M. Foglino, E. Locatelli, D. Michieletto, C. A. Brackley, C Likos, and D. Marenduzzo. On the non-equilibrium effects of molecular motors on polymeric substrates. *Draft ready for submission.*

[4] M. Foglino, A. N. Morozov, and D. Marenduzzo. Deformable droplets suspension: Irreversibility transition. *Draft in preparation.*